Double-Spin Asymmetries in Diffractive Vector-Meson Production at HERMES

by

K. Lipka

Double-Spin Asymmetries in Diffractive Vector-Meson Production at HERMES

Dissertation

zur Erlangung des akademischen Grades

doctor rerum naturalium
(Dr. rer. nat.)

im Fach Physik

eingereicht an der
Mathematisch-Naturwissenschaftlichen Fakultät I
der Humboldt-Universität zu Berlin

von

Diplom Physikerin
Ekaterina Lipka (geb. Negodaeva)
geboren am 22. Mai 1977 in Moskau

Präsident der Humboldt-Universität zu Berlin
Prof. Dr. Jürgen Mlynek

Dekan der Mathematisch-Naturwissenschaftlichen Fakultät I
Prof. Dr. Bernhard Ronacher

Gutachter/innen:
1. Prof. Dr. Paul Söding
2. Prof. Dr. Eva-Maria Kabuß
3. Prof. Dr. Edward Kinney

Tag der mündlichen Prüfung: 04. Juni 2002

Abstract

This thesis is devoted to the measurement of double-spin asymmetries in the cross section of exclusive diffractive electroproduction and quasi-real photoproduction of ρ^0- and ϕ-mesons in the kinematic region of HERMES, characterized by $< Q^2 >= 1.8$ GeV^2, $< W^2 >= 24.5$ GeV^2, and $< x >= 0.07$. Data used for this analysis were collected with the HERMES experiment in the years 1996-2000 using the longitudinally polarized lepton beam of HERA and the internal target of HERMES, filled with longitudinally polarized protons and deuterons. The purpose of this measurement was to tag the parity of the object exchanged in the t-channel of the interaction of the vector-meson state with the nucleon and thereby to test different theoretical models of vector-meson production mechanisms. The photon-absorption asymmetry in exclusive ρ^0-production on the deuteron target was measured to be consistent with zero, while this asymmetry on the proton target was confirmed to be slightly positive. These results are consistent with different theoretical predictions for a significant contribution of unnatural-parity object exchange (either Reggeon or di-quark object) to exclusive ρ^0-production. The photon-absorption asymmetries in exclusive ϕ-production are measured to be consistent with zero for both proton and deuteron targets. These measurements agree with the prediction of Pomeron-exchange dominance in ϕ-meson production. The dependence of the asymmetries on kinematic variables was investigated. At very low Q^2 (quasi-real photoproduction regime) the double-spin asymmetries for ρ^0- and ϕ-mesons are measured to be consistent with zero for both proton and deuteron targets. No theoretical expectation for the value of the double-spin asymmetry at very low Q^2 exists, up to now. Altogether, the conclusion is drawn that at the intermediate energies of the HERMES experiment ρ^0-meson production follows the Generalized Vector Meson Dominance scheme with subsequent scattering of the vector-meson state off the nucleon proceeding via exchange of both Reggeon(s) and Pomeron(s) in the t-channel.

Zusammenfassung

Die vorliegende Arbeit beschreibt die Messung der Doppel-Spin-Asymmetrien im Wirkungsquerschnitt der exklusiven diffraktiven Elektroerzeugung und quasi-reellen Photoerzeugung von ρ^0- und ϕ-Mesonen im kinematischen Bereich des HERMES-Experimentes, $< Q^2 >= 1.8$ GeV^2, $< W^2 >= 24.5$ GeV^2, $< x >= 0.07$. Die Analyse umfasst die Daten des HERMES-Experimentes, aufgezeichnet in den Jahren 1996-2000 mit longitudinal-polarisiertem Leptonenstrahl des HERA-Beschleunigers und internem longitudinal polarisierten Proton- bzw. Deuteron-Target von HERMES. Das Ziel der Messung war es, die Parität des Austausch-Objektes im t-Kanal der Wechselwirkung des Vektor-Meson Zustandes mit dem Nukleon zu untersuchen und dadurch die verschiedenen theoretischen Modelle der Vektor-Meson-Erzeugung zu überprüfen. Die Photon-Absorptions-Asymmetrie bei exklusiver ρ^0-Meson-Erzeugung am Deuteron-Target wurde mit Null verträglich gemessen, während diese Asymmetrie am Proton-Target einen kleinen positiven Wert ergibt. Diese Ergebnisse stimmen mit verschiedenen theoretischen Modellen überein, die vorhersagen, dass es bei ρ^0-Meson-Erzeugung einen signifikanten Anteil des Austausches von Objekten mit unnatürlicher Parität (Reggeon oder Di-Quark-Objekt) gibt. Die Photon-Absorptions-Asymmetrie bei exklusiver diffraktiver ϕ-Meson-Erzeugung am Deuteron- sowie am Proton-Target wurde mit Null verträglich gemessen. Diese Messung stimmt mit einer Vorhersage der Dominanz des Pomeron-Austausches bei ϕ-Meson-Erzeugung überein. Die Abhängigkeit der Asymmetrie von den kinematischen Variablen wurde untersucht. Die Doppel-Spin-Asymmetrien in ρ^0- und ϕ-Meson Erzeugung bei kleinen Q^2 (quasi-reelle Photoerzeugung) wurden mit Null verträglich gemessen für Proton- und Deuteron-Targets. Bisher existieren keine theoretischen Vorhersagen für Doppel-Spin Asymmetrien in quasi-reeller Photoerzeugung von Vektor-Mesonen. Zusammenfassend es lässt sich sagen, dass bei den mittleren Energien des HERMES-Experimentes die ρ^0-Meson Erzeugung dem Generalisierten Vektor-Meson-Dominanz-Schema folgt, mit nachfolgender Streuung des virtuellen Vektor-Meson-Zustandes am Nukleon, welche durch den Austausch von Reggeon(en) und Pomeron(en) im t-Kanal erfolgt.

Contents

Introduction **4**

1 Diffractive Vector-Meson Production **6**

1.1 Kinematics 6

1.1.1 Polarization Parameters 9

1.2 Diffraction 9

1.3 The Structure of the Photon 11

1.4 Vector-Meson Dominance 14

1.5 Generalized Vector-Meson Dominance 15

1.5.1 General Considerations 15

1.5.2 Application to Vector-Meson Electroproduction 17

1.6 Regge Model 18

1.7 Generalized Parton Distributions 21

1.8 Cross Section of Vector-Meson Production 23

1.8.1 GVMD Prediction 23

1.8.2 Regge-based Models 24

1.8.3 GPD-based Model 26

2 Vector-Meson Polarization **28**

2.1 Formalism 28

2.2 The Photon Spin Density Matrix 29

2.3 Vector-Meson Spin Density Matrix 31

2.3.1 Polarized Lepton, Unpolarized Nucleon 31

2.3.2 s-Channel Helicity Conservation 32

2.3.3 Parity of the Exchange 32

2.3.4 Angular Distributions 33

2.3.5 Measurements of Spin Density Matrix Elements and R 34

2.3.6 Polarized Lepton, Polarized Nucleon 35

3 Double-Spin Asymmetries in Photon-Nucleon Interactions 36
3.1 Double-Spin Asymmetries in DIS 36
3.1.1 Nucleon Structure Functions 36
3.1.2 Formalism of Double-Spin Asymmetries in DIS 38
3.2 Spin Asymmetry in Vector-Meson Production 40
3.2.1 Asymmetry in Exclusive ρ^0-meson Electroproduction. 41
3.2.2 Calculation in the Framework of Regge Model 43
3.2.3 pQCD Calculation based upon Hadron-Parton Duality 44
3.2.4 Asymmetry in Quasi-Real Photoproduction of Vector Mesons 45

4 The HERMES Experiment 47
4.1 Polarized Electron Beam of HERA 47
4.2 Internal Gas Target 49
4.3 HERMES Spectrometer 51
4.3.1 Tracking Chambers 51
4.3.2 Track Reconstruction 52
4.3.3 Particle Identification Detectors 53
4.3.4 Particle Identification Scheme 54
4.3.5 Luminosity Measurement 55
4.3.6 Trigger 56
4.4 Ring-Imaging Cherenkov Detector 56
4.4.1 Design Parameters 56
4.4.2 Angle Reconstruction 58
4.4.3 Hadron Identification Efficiencies 61

5 Analysis of Double-Spin Asymmetries 64
5.1 Event Selection Criteria 64
5.1.1 Data Organization and Data Quality 64
5.1.2 Selection of the Physics Sample 66
5.1.3 Selection of Exclusive Diffractive Events 67
5.1.4 Selection of Quasi-Real Photoproduction Events 72
5.2 Monte-Carlo Simulations 73
5.3 Exclusive Diffractive Vector-Meson Production 76
5.3.1 Spin Asymmetries in ρ^0-production 76
5.3.2 Spin Asymmetries in ϕ-production 87
5.4 Quasi-Real Photoproduction of Vector Mesons 90

5.4.1 Spin Asymmetries in ρ^0-production 90
5.4.2 Spin Asymmetries in ϕ-production 92
5.5 Comparison with Theoretical Expectations 93
5.5.1 Comparison with a GVMD-based Prediction 93
5.5.2 Comparison with a Regge-based Model 95
5.5.3 Prediction Based on Hadron-Parton Duality 97

Conclusions **98**

A Appendices **101**

References **104**

Acknowledgments **113**

Erklärung **115**

Lebenslauf **117**

Introduction

Fundamental particles and their interactions are described by the Standard Model that comprises leptons and quarks which build up matter, and gauge bosons which mediate the exchange forces between them. Quarks and leptons are spin-1/2 particles, while bosons have integer spin. In the parton picture combinations of two or three quarks, held together by gluons, are building up hadrons, thereby defining their mass and quantum numbers. Baryons are composed out of three quarks, mesons are made of quark-antiquark pairs.

The way to study the innermost structure of matter is to resolve it, e.g. by breaking up the target nucleon in scattering experiments at high energies. The first indication for the existence of point-like constituents of the nucleon came from deep inelastic scattering experiments. Polarized deep inelastic lepton-nucleon scattering is still a very promising tool to study the spin structure of the nucleon which is described in the quark-parton model by spin-independent structure functions F_1, F_2 and spin-dependent structure functions g_1, g_2. Less than half of the nucleon spin was found to be carried by quarks, the remaining part has been assigned to gluons and to orbital angular momenta of quarks and gluons.

The HERMES experiment at HERA was designed to study the different contributions to the nucleon spin in deep inelastic scattering of a longitudinally polarized lepton beam off an internal target, filled with longitudinally polarized or unpolarized gas atoms. Precision measurements of the spin-dependent structure function g_1 are accomplished through the measurements of double-spin asymmetries in inclusive lepton-nucleon scattering. By measuring spin asymmetries in semi-inclusive processes the contributions of different quark flavors can be separated. Spin asymmetries of high-p_T hadron pairs, produced in the photon-gluon fusion process, can be used to tag the contribution of the gluon polarization to the nucleon spin.

The study of diffractive vector-meson production in lepton-nucleon scattering is one of the objectives of the HERMES experiment, as well. Diffractive vector-meson production in lepton-nucleon scattering is described by a fluctuation of the virtual photon that was emitted by the electron, into a $q\bar{q}$ state. The process is defined by the photon virtuality Q^2, its energy ν and the invariant mass of the photon-nucleon system W^2. If the target nucleon stays intact in the vector-meson production process, the latter is referred to as exclusive vector-meson production. There are several models to explain exclusive diffractive vector-meson production. In the model of Vector-Meson Dominance a $q\bar{q}$-pair forms a vector meson that subsequently interacts strongly with the nucleon. In the framework of Regge-based models this process is described by Reggeon exchange at $W^2 < 5$ GeV^2, while at higher W^2 the theory involves Pomeron exchange. At the intermediate energy of HERMES

both Pomeron and Reggeon exchanges are thought to contribute. Once a hard scale is involved the description of the nucleon structure in terms of generalized parton distributions becomes possible. In this case vector-meson production is expected to proceed through quark exchange at $W^2 < 5$ GeV^2, and through two-gluon exchange at higher W^2. This approach, however, is presently on solid theoretical ground only for vector-meson production from longitudinal photons.

The measurement of double-spin asymmetries in exclusive vector-meson production can help to understand the mechanism of the exchange in the t-channel of the reaction, indicating the parity of the exchanged object. Pomeron exchange would result in a zero asymmetry, while the exchange of a di-quark object would give a non-zero asymmetry. In quasi-real photoproduction of vector mesons the double-spin asymmetry is an important quantity, as well. It may change or at least dilute the asymmetries measured in inclusive quasi-real photoproduction of high-p_t hadrons, which is used to access the gluon polarization.

This thesis describes the measurements of double-spin asymmetries in the cross section of exclusive diffractive electroproduction and quasi-real photoproduction of ρ^0- and ϕ-mesons in polarized lepton scattering off polarized proton and deuteron targets. The data collected with the HERMES experiment in the years 1996-2000 are used for the analysis.

In Chapter 1 an overview of the theoretical models of diffractive vector-meson production is given, and the kinematics of the processes are defined. Chapter 2 is devoted to the introduction of the vector-meson polarization formalism which is used in chapter 3, where the expectations for double-spin asymmetries in vector-meson production are given based on different theoretical approaches. The HERMES experiment is described in Chapter 4 where special attention is paid to the Ring-Imaging Cherenkov detector that has been operated from 1998 on. It is able to identify pions, kaons and protons with high efficiency in the most populated momentum region of HERMES.

The analysis of double-spin asymmetries in exclusive diffractive and quasi-real photoproduction of ρ^0- and ϕ-mesons is presented in chapter 5. The reconstruction of the data and the selection of the studied event samples for the double-spin asymmetry analysis are explained. Estimates are given for average kinematic variables in quasi-real photoproduction of both vector mesons. Finally the extraction of the asymmetries, the interpretation of the results and their comparison with theoretical expectations are described in detail.

Chapter 1

Diffractive Vector-Meson Production

Diffractive vector-meson production in lepton[1]-nucleon scattering is usually explained by a fluctuation of the virtual photon emitted by the lepton, into a $q\bar{q}$ state with its subsequent scattering off the nucleon by a strong interaction. The scattering of the $q\bar{q}$ off a nucleon can be calculated either in phenomenological Regge theory, or in the framework of perturbative Quantum Chromodynamics (QCD). In the following different theoretical approaches to describe diffractive vector-meson production are discussed.

1.1 Kinematics

Lepton-nucleon scattering is depicted in fig. 1.1.1, representing schematically a) deep inelastic scattering (DIS) $eN \to e'X$ and b) vector-meson production $eN \to e'VX$. The kinematic regions of the processes are defined below.

In Born approximation the interaction is mediated by the exchange of a single (virtual) photon. The process kinematics is described in the system of units where $\hbar = c = 1$ and the electron mass is neglected.

The four-momentum and the energy in the laboratory frame (lab) of the incoming lepton are denoted by k and E respectively; those of the scattered lepton by k' and E'. The lepton scattering angle is θ. In the laboratory frame the target nucleon is at rest: $p = (M, \vec{0})$. The momentum of the hadronic final state is p'. The four-momentum of the exchanged virtual photon is $q = k - k'$. The process is described by the Lorentz invariant quantities Q^2, ν, W^2, from which only two are independent:

$$Q^2 \equiv -q^2 \stackrel{lab}{=} 4EE'sin^2(\theta/2) \ , \tag{1.1.1}$$

$$\nu \equiv \frac{p \cdot q}{M} \stackrel{lab}{=} E - E' \ , \tag{1.1.2}$$

$$W^2 \equiv (q+p)^2 \stackrel{lab}{=} M^2 + 2M\nu - Q^2. \tag{1.1.3}$$

Here Q^2 is the invariant mass of the virtual photon, or photon virtuality, which is positive. In case of real photons $Q^2 = 0$. The photon energy is represented by ν, and W is the

[1]Here and further lepton denotes electron or positron.

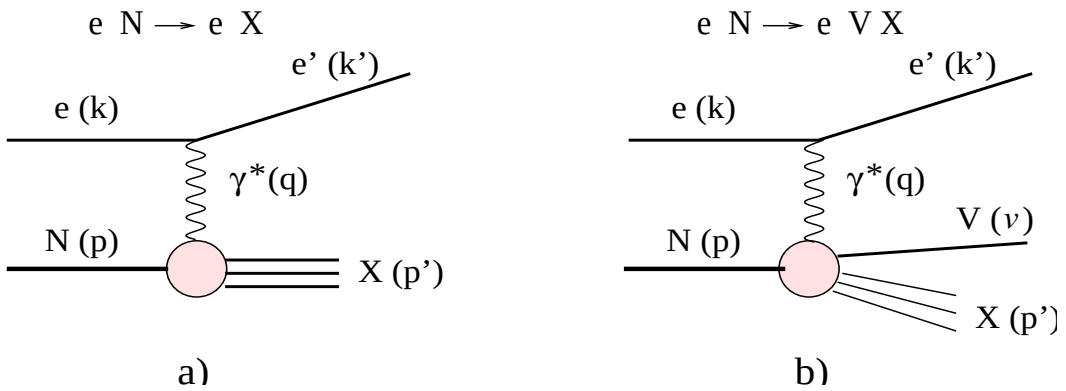

Figure 1.1.1: Schematic representation of lepton-nucleon scattering in lowest order QED; exchange of a single virtual photon in a) deep inelastic scattering, b) vector-meson production.

center-of-mass energy of the photon-nucleon system. The center-of-mass energy s of the lepton-nucleon system is given by

$$s \equiv (k+p)^2 \stackrel{lab}{=} M^2 + 2ME \tag{1.1.4}$$

and has for the HERMES beam energy of 27.5 GeV a value of $\sqrt{s} = 7.2$ GeV. In the analysis of DIS events two scaling variables are used:

$$x \equiv \frac{Q^2}{2p \cdot q} \stackrel{lab}{=} \frac{Q^2}{2M\nu}\,, \tag{1.1.5}$$

$$y \equiv \frac{p \cdot q}{p \cdot k} \stackrel{lab}{=} \frac{\nu}{E}. \tag{1.1.6}$$

In the laboratory frame y represents the fractional energy of the virtual photon with respect to the beam energy.

The HERMES kinematic acceptance is represented in fig. 1.1.2. There are two important kinematic regimes:

- The DIS regime is defined as region with the photon virtuality above the nucleon mass, $Q^2 > 1$ GeV^2, and the effective mass of the produced hadronic system above the resonance region, $W > 2$ GeV. To avoid the kinematic region where large radiative corrections are necessary the cut $y < 0.85$ is applied.

- The process denoted as quasi-real photoproduction corresponds to lepton-nucleon scattering proceeding at very low photon virtualities, $Q^2 \approx 0$, but still producing a hadronic state above the resonance region, $W > 2$ GeV.

The kinematic limits for the analysis of vector-meson production will be discussed in section 5.1.3. An important kinematic parameter in exclusive vector-meson production (i.e. X≡ p) is the four-momentum transfer to the hadronic vertex

$$t = (p - p')^2 = (q - v)^2 < 0, \tag{1.1.7}$$

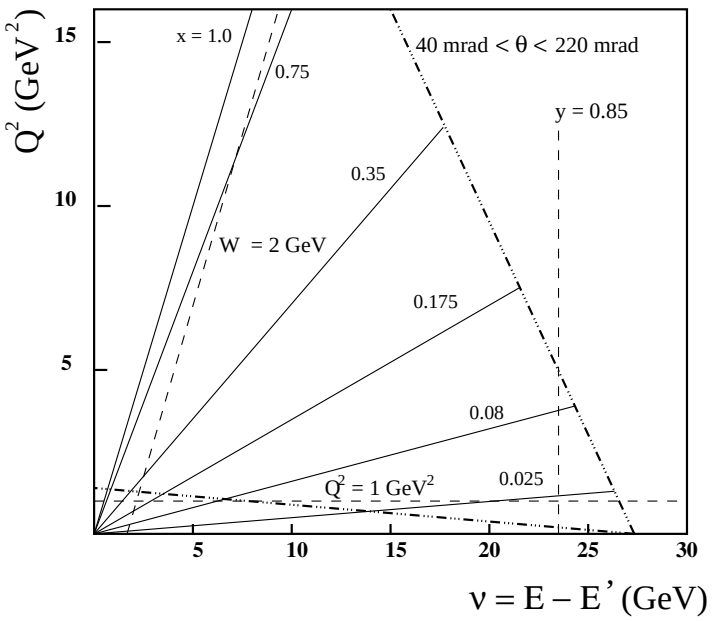

Figure 1.1.2: The kinematic acceptance of the HERMES experiment. The dashed lines denote the cuts applied in general DIS analysis: $Q^2 > 1$ GeV^2, $W > 2$ GeV, $y < 0.85$. The detector acceptance is given by 40 mrad $< \theta <$ 220 mrad (dash-dotted line).

where v is the four-momentum of the vector meson. The four-momentum of the hadronic final state p' is not measured directly at HERMES. Instead it can be calculated as $p' = p + q - v$.

The threshold of the momentum transfer t_0, above which the interaction is kinematically allowed, can be calculated in the photon-nucleon center-of-mass frame [1]:

$$t_0 = (E_{\gamma,cm} - E_{V,cm})^2 - (|p_{\gamma,cm}| - |p_{V,cm}|)^2 \ , \tag{1.1.8}$$

where

$$E_{\gamma,cm} = \frac{W^2 - Q^2 - M^2}{2W} \ , \tag{1.1.9}$$

$$|p_{\gamma,cm}| = \sqrt{E_{\gamma,cm}^2 + Q^2} \ , \tag{1.1.10}$$

$$E_{V,cm} = \frac{W^2 - M_{inv}^2 - M_x^2}{2W} \ , \tag{1.1.11}$$

$$|p_{V,cm}| = \sqrt{E_{V,cm}^2 - M_{inv}^2}. \tag{1.1.12}$$

Here M_x is the mass of the recoiling nucleon, $M_x^2 = p'^2$. In the photon-nucleon center-of-mass frame $t = t_0$ corresponds to the case in which the vector meson is produced collinear to the direction of the virtual photon. Another useful variable is the four-momentum transfer above the threshold, $t' \equiv t - t_0$. All three variables t, t_0 and t' are negative and invariant against Lorentz transformation.

1.1.1 Polarization Parameters

The polarization of a particle is represented by the helicity λ, that is the projection of the spin vector $\vec{s}$ onto the particle's direction of motion $\vec{p}$: $\lambda = \frac{\vec{s}\cdot\vec{p}}{|\vec{s}|\cdot|\vec{p}|}$. If the spin vector is parallel (antiparallel) to the 3-momentum of the particle, the particle is said to be longitudinally polarized with corresponding helicity $\lambda = 1$ ($\lambda = -1$). If the spin and 3-momentum vectors are perpendicular which corresponds to zero helicity, the particle is said to be transversely polarized.

The nomenclature of the photon polarization however, left over from optics, differs from the one given above. In the framework of classical electrodynamics it follows from the Maxwell equations that the propagation vector $\vec{k}$ of a plane wave $\vec{a} = a_0\ e^{i\vec{k}\vec{x}-i\omega t}$ is required to be perpendicular to the direction of electric $\vec{E}$ and magnetic $\vec{B}$ fields [2]. Such a wave is called transverse. It can have scalar, linear and elliptic (circular) polarization.

A photon as a spin-1 particle can have one of the helicity states $\lambda = +1, 0, -1$. The polarization state of the photon is called transverse if $\lambda = \pm 1$, otherwise it is longitudinal. Real photons are 100% transverse. Virtual photons can be both transverse and longitudinal. This definition of photon polarization is used when discussing vector-meson production, as well.

Note that a longitudinally polarized lepton beam will produce a flux of transverse photons at $Q^2 \approx 0$, while at higher Q^2 a non-zero contribution of longitudinal photons appears.

The polarization parameter ϵ expresses the ratio between the longitudinal and transverse photon fluxes Γ_L and Γ_T:

$$\epsilon = \frac{\Gamma_L}{\Gamma_T} = \frac{1-y}{1-y+y^2/2}\ . \tag{1.1.13}$$

The effective polarization of the photon is represented by:

$$D = \frac{1-(1-y)\ \epsilon}{1+\epsilon R}\ , \tag{1.1.14}$$

where R is the ratio of the photon-nucleon interaction cross sections for longitudinal and transverse photons, $R = \frac{\sigma_L}{\sigma_T}$.

1.2 Diffraction

The term "diffraction" originates from classical optics and indicates similarities in the behavior of the cross section of hadronic interactions to the light intensity distribution in optical diffraction, where the distribution of the scattering angle exhibits a strong peak in the forward direction with subsequent minima and maxima at larger angles. In the optical model of diffraction, described in detail in Ref. [3], hadron-hadron scattering is simplified as absorption of a hadron with momentum p and impact parameter b by a black disk with radius R_D. The momentum transfer between the two hadrons is defined in the center-of-mass frame as $-t \equiv q^2 = (2p\ sin(\theta/2))^2$, where θ is the scattering angle. The differential cross section

is found to be independent of the energy of the incident particle,

$$\frac{d\sigma}{dq} = \pi R_D^4 \left| \frac{J_1(R_D q)}{R_D q} \right|^2 \approx \frac{\pi R_D^4}{4}\ exp\left(-\frac{R_D^2 q^2}{4} \right), \tag{1.2.1}$$

where $J_1(x)$ is the Bessel function of the first order and R_D represents the radius of the target hadron. This simple model of scattering a plane wave on a black disk reproduces the basic properties of elastic pp interactions [3], but fails to predict the ratio of the elastic and total cross sections and their energy dependence. The model can be improved by assuming the disk to be not totally absorbing but "grey" with a Gaussian density distribution. This approach yields the cross section in the form

$$\frac{d\sigma}{dt} = \frac{d\sigma}{d|t|}\Big|_{t=0} e^{-b|t|}\ . \tag{1.2.2}$$

The exponential slope b can be related to the radius of the black disk R_D by $b = R_D^2/4$. Typical values of the slope b vary between 5 and 13 GeV^{-2}. Note that in optical models the polarization of the interacting particles is disregarded.

In contemporary approaches [4, 5] a diffractive process is defined by the exchange of vacuum quantum numbers at high energies. No non-zero color or flavor quantum numbers may be exchanged in the interaction, while the exchange of spin quantum number is allowed. If both interacting particles stay intact after collision the process is called elastic. In the case where one of the interacting particles is excited to a resonance or produces secondary particles, the process is called single-dissociative diffraction. If both interacting particles produce secondary particles, the process is called double-dissociative diffraction. In fig. 1.2.1 elastic, single-dissociative and double-dissociative diffractive processes are shown schematically. In

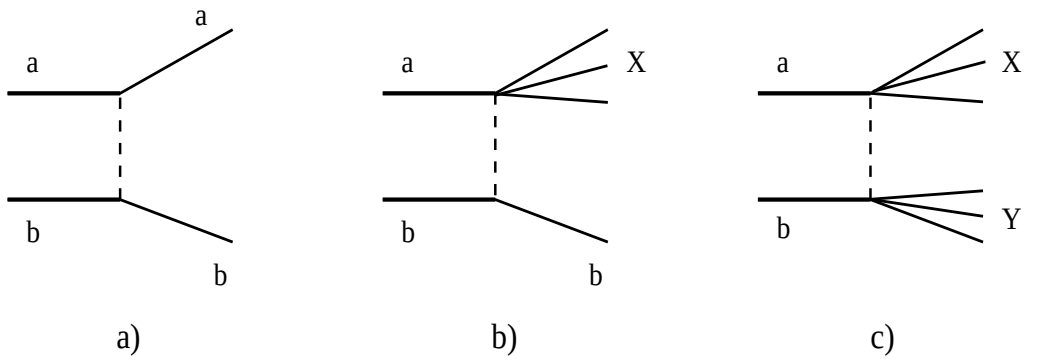

Figure 1.2.1: a) elastic, b) single-dissociative and c) double-dissociative diffractive processes. The dotted line represents energy and momentum exchange, a and b denote photons or hadrons, X and Y are resonances or a sum over multi-particle states.

general the high-energy condition requires the square of the center-of-mass energy s being larger than other energy scales, $s \gg t$, M_X^2, or for virtual photons $Q^2/s \ll 1$. In order to preserve the identity of the target in diffractive scattering the momentum transfer is limited by $|t| < 1/R_T^2$, where R_T^2 is the radius of the target nucleon. For a hadronic radius of 1 fm

the corresponding limit is $|t| < 1$ GeV^2. The $-t$ distribution has an exponential behavior, $f(t) \sim e^{-b|t|}$. Other general experimental signatures of diffractive processes are the slow rise of the cross section with energy and rapidity[2] gaps. The final state particles (e.g. X and Y in fig. 1.2.1) emerge in the forward and backward directions in the center-of-mass frame and are separated in rapidity or pseudo-rapidity.

Besides the optical model sketched above, where hadron-hadron scattering is explained using concepts of classical diffraction in optics, two other approaches are discussed in Ref. [4] to describe diffraction in terms of vacuum exchange. These are the Regge phenomenology, implying the exchange of one or more Regge poles with vacuum quantum numbers, and the gluon exchange model, regarding the vacuum exchange as the exchange of two or more gluons in a color-singlet state. Both approaches will be discussed in more detail below.

1.3 The Structure of the Photon

In the first years of quantum electrodynamics a photon was regarded as a structureless particle. Later on, when experiments at higher energy became possible, the fluctuation of a photon into an electron-positron pair through an interaction with a Coulomb field was a first manifestation of a more complicated photon structure. Also features of pure hadronic interactions were found in various photon scattering experiments [6]. Indeed, quantum-mechanically a photon may fluctuate into a fermion-antifermion pair $f\bar{f}$. Such a pair interacts strongly with the nucleon and is thought to be responsible for the major part of the γp total cross section [7]. The Q^2 spectrum of $f\bar{f}$ fluctuations of the photon can be split into a low- and a high-virtuality part. The low-virtuality part can be described by Vector-Meson Dominance (VMD), where the photon fluctuation into the $q\bar{q}$ pair is approximated by a sum over low mass vector-meson states (see section 1.4). The high-virtuality part is calculable in perturbative QCD. Altogether, the photon wave function can be written as [8]

$$|\gamma >= \sqrt{Z_3}|\gamma_b > + \sum_{V=\rho^0,\omega,\phi,J/\psi} c_V \; |V > + \sum_{q=u,d,s,c,b} c_q \; |q\bar{q} > + \sum_{l=e,\mu,\tau} c_l \; |l^+l^- >, \qquad (1.3.1)$$

$$Z_3 = 1 - \sum_{V=\rho^0,\omega,\phi,J/\psi} c_V^2 \; - \sum_{q=u,d,s,c,b} c_q^2 \; - \sum_{l=e,\mu,\tau} c_l^2 \; . \qquad (1.3.2)$$

The coefficients c_V, c_q, c_l depend on the factorization scale μ at which the photon is probed and which is usually taken to be the transverse momentum of the $2 \to 2$ parton level process. The coefficient Z_3 is close to unity [7]. Two *transverse* momentum transfer scales are introduced to describe the process [7]. These are $k_\perp$, related to the $\gamma \to q\bar{q}$ vertex, and $p_\perp$, defining the hardest QCD $2 \to 2$ subprocess of the "ladder" between the photon and the proton. An additional scale $k_0 \approx 0.5$ GeV separates the low-mass vector-meson region from the high-mass $q\bar{q}$ one. It is also the lower cut-off of the photon-parton cross section since the vertex $\gamma \to q\bar{q}$ is responsible for interactions of the bare photon. The states $|l^+l^- >$ can be

[2]Rapidity y is defined in terms of the particle energy E and the momentum p_z in z (beam) direction as $y = \frac{1}{2}\, ln(\frac{E+p_z}{E-p_z})$. Pseudo-rapidity is $\eta = -ln\; tan(\frac{\theta}{2})$, where θ is the polar angle with respect to the beam direction.

neglected here as their strong interaction with partons inside a hadron occurs only at higher orders.

Three kinds of interactions, depicted in fig. 1.3.1, can be distinguished:

- VMD process: the photon fluctuates into a vector meson that is subsequently scattered off the proton. All the subprocesses known from hadron-hadron interactions may occur such as e.g. elastic, diffractive etc.
- 'Direct' process: the bare photon $|\gamma_b>$ interacts directly with a parton of the proton, e.g. photon-gluon fusion (PGF) and QCD Compton scattering (QCDC). The process is calculable in perturbative QCD and no photon structure function is involved.
- 'Anomalous' process: the photon fluctuates perturbatively in the $q\bar{q}$ pair and one of the quarks interacts then with the parton of the proton. This process is calculable in perturbative QCD, as well.

At HERMES energies mainly a VMD processes are observed with a small contribution of direct processes. The phase space of the processes is defined by the $k_\perp$ and $p_\perp$ scales,

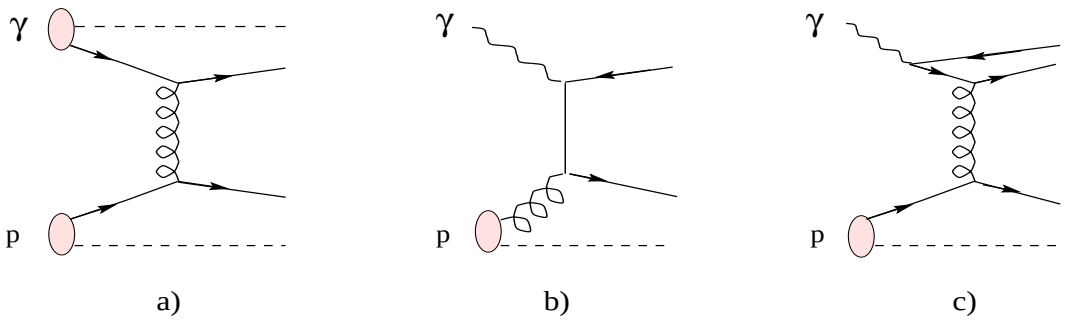

Figure 1.3.1: a) VMD, b) direct and c) anomalous process contribution to γp scattering. Only basic graphs are illustrated. Full lines indicate partons that may give rise to high-p_T jets, dashed lines represent spectator jets. The figure is taken from Ref.[7].

as shown in fig. 1.3.2. The difference between the three processes is reflected in the beam jet structure. The photon in direct processes does not give any beam jet, as all of its energy is involved into the interaction, while the VMD and anomalous processes[3] leave a beam remnant. The VMD and anomalous processes are also called resolved ones. All three processes are of order $\mathcal{O}(\alpha_{em})$.

The VMD weighting factor $c_V^2 = 4\pi\alpha_{em}/f_V^2$, where f_V is the $\gamma \to V$ coupling constant, gives the probability for the transition $\gamma \to V$. The coefficients $f_V^2/4\pi$ can be obtained from data using their relation to the mass M_{VM} and the leptonic decay width Γ_{VM}^{ll} of the vector meson according to Ref. [6],

$$\frac{f_V^2}{4\pi} = \frac{\alpha_{em}^2 M_{VM}}{3\Gamma_{VM}^{ll}} \ . \tag{1.3.3}$$

[3]One of the quarks plays a role of a beam remnant, but is has a larger p_t than in the VMD case.

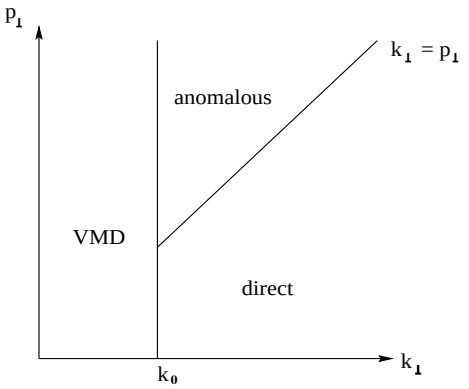

Figure 1.3.2: Phase space for the subdivided classes of photon interactions [7].

Its value appeared to be 2.20 for ρ^0, 23.6 for ω, 18.4 for ϕ and 11.5 for J/ψ, implying that the photon can be found in a VMD state about 0.4 % of the time.

The contribution from the high mass fluctuations depends on the typical scale μ at which the photon is probed:

$$c_q^2 \approx \frac{\alpha_{em}}{2\pi}\frac{N_C}{3}\left(2\sum_q e_q^2\right) ln\left(\frac{\mu^2}{k_0^2}\right), \tag{1.3.4}$$

where $N_C = 3$, and quarks can be taken massless compared with μ. The total photon-proton cross section reads:

$$\sigma_{tot}^{\gamma p}(s) = \sigma_{dir}^{\gamma p}(s) + \sigma_{VMD}^{\gamma p}(s) + \sigma_{anom}^{\gamma p}(s)\ . \tag{1.3.5}$$

To obtain a cross section valid for both DIS and real photoproduction regimes, the DIS cross section has to be parameterized in a way that it vanishes at $Q^2 \to 0$. Such parameterization is given in Ref. [9], where the total DIS cross section is represented via the lowest order (LO) DIS process $\gamma^* q \to q$, with $\mathcal{O}(\alpha)$ corrections from PGF or QCDC (direct) processes. In Ref. [9] the cross section of the lowest order DIS is given in a form:

$$\sigma_{LO\ DIS}^{\gamma^* p} \to \sigma_{DIS}^{\gamma^* p}\ exp\left(-\frac{\sigma_{QCDC}^{\gamma^* p} + \sigma_{PGF}^{\gamma^* p}}{\sigma_{DIS}^{\gamma^* p}}\right)\ . \tag{1.3.6}$$

The total cross section then reads:

$$\sigma_{tot}^{\gamma^* p} = \sigma_{DIS}^{\gamma^* p}\ exp\left(-\frac{\sigma_{dir}^{\gamma^* p}}{\sigma_{DIS}^{\gamma^* p}}\right) + \sigma_{dir}^{\gamma^* p} + \left(\frac{W^2}{Q^2+W^2}\right)^n \sigma_{res}^{\gamma^* p}, \tag{1.3.7}$$

where $\sigma_{res}^{\gamma^* p}$ corresponds to the cross section of resolved processes (VMD and anomalous ones) in which the fluctuation of the photon into $q\bar{q}$ is damped by a factor $(\frac{W^2}{Q^2+W^2})^n$ with n being of the order of 3 or 4. The term $\sigma_{dir}^{\gamma^* p} = \sigma_{QCDC}^{\gamma^* p} + \sigma_{PGF}^{\gamma^* p}$ stands for the contribution from direct processes.

1.4 Vector-Meson Dominance

Vector-Meson Dominance assumes that the photon-nucleon interaction proceeds via a direct coupling of the photon to a vector meson and a subsequent (strong-interaction) diffractive scattering of the vector meson off the nucleon. This ansatz is described in detail in Ref. [6]. As described above, the photon fluctuates into a $q\bar{q}$ pair that forms a light neutral vector meson conserving the quantum numbers of the photon $J^{PC} = 1^{--}$, $B = S = Y = 0$. The 'hadronic' term $|V>$ in Eq. (1.3.1) is then a sum over $V = \rho^0$, ω and ϕ states. The fluctuation time is defined by

$$t_f \approx \frac{2\nu}{Q^2 + M_V^2} \ , \tag{1.4.1}$$

and needs to be long enough for a virtual vector meson to travel over a distance larger than the nucleon radius so that the interaction between the virtual meson and the nucleon can occur.

The production of vector mesons by real photons is described by VMD very successfully, relating the total cross section of the photon-nucleon interaction to that of (forward) elastic vector-meson scattering off the nucleon using the optical theorem:

$$\sigma^{\gamma p} = \sum_V \sqrt{16\pi} \sqrt{\frac{4\alpha\pi}{f_V^2}} \left(\frac{d\sigma^{\gamma p \to Vp}}{d|t|}\Big|_{t=0} \right)^{1/2} , \tag{1.4.2}$$

$$\frac{d\sigma^{\gamma p \to Vp}}{d|t|}\Big|_{t=0} = \frac{e^2}{f_V^2} \frac{d\sigma^{Vp \to Vp}}{d|t|}\Big|_{t=0} . \tag{1.4.3}$$

The fractional contributions r_{VM} of different vector mesons to the total cross section $\sigma^{\gamma p}$ were found to be $r_\rho = 65\%$, $r_\omega = 8\%$ and $r_\phi = 5\%$, adding up to 78% of the total cross section of vector-meson photoproduction. An additional contribution of $r_{J/\psi} \sim 1 - 2\%$ has to be added for the J/ψ meson.

The model was extended to virtual photons, assuming that the Q^2 dependence is fully determined by the propagator of a single VM state, $1 + \frac{Q^2}{M_V^2}$. In case of virtual photons the cross section needs to be split up into longitudinal and transverse parts, as a longitudinal photon needs not to have the same total cross section as a transverse one. The VMD calculation, based on the assumption that both cross sections are dominated by ρ^0, ω and ϕ-mesons, gives for the transverse and longitudinal cross sections [6]

$$\sigma_T^{\gamma^* p \to Vp} = \sum_V \frac{e^2}{f_V^2} \left(1 + \frac{Q^2}{M_V^2} \right)^{-2} \sigma_V , \tag{1.4.4}$$

$$\sigma_L^{\gamma^* p \to Vp} = \sum_V \frac{e^2}{f_V^2} \frac{\xi_V Q^2}{M_V^2} \left(1 + \frac{Q^2}{M_V^2} \right)^{-2} \sigma_V , \tag{1.4.5}$$

where $\sigma_V = \sigma_T^{VM}(\nu, Q^2 = 0)$ is the total cross section of the transversely polarized vector meson. The ratio of longitudinal-to-transverse vector-meson cross sections is represented by

the factor ξ_V. The longitudinal-to-transverse cross section ratio for $\gamma^* p$ interaction is then

$$R = \frac{\sigma_L}{\sigma_T} = \xi_V^2 \frac{Q^2}{M_V^2} \ . \tag{1.4.6}$$

In VMD ξ_V is predicted to be $\xi_V \approx 0.6$ which led to a high value of R and was found to disagree with experiment [6]. HERMES data show that the value of ξ_ρ^2 is less than 0.2 [10]. The total cross section for the interaction of a virtual photon with a proton is given by Eqs. (1.4.4, 1.4.5):

$$\sigma^{\gamma^* p \to Vp}(\nu, Q^2) = \left(1 + \epsilon\ \xi_V^2 \frac{Q^2}{M_V^2}\right)\left(1 + \frac{Q^2}{M_V^2}\right)^{-2} \sigma^{\gamma p \to Vp}(\nu, Q^2 = 0), \tag{1.4.7}$$

where ϵ is the ratio between the fluxes of longitudinal and transverse photons, as defined in Eq. (1.1.13).

1.5 Generalized Vector-Meson Dominance

1.5.1 General Considerations

Generalized Vector-Meson Dominance (GVMD) treats the sum rule (1.4.2) as a reasonable approximation for $Q^2 \approx 0$ while it is considered to be broken for non-zero virtualities. Indeed, the idealization that the propagation of a single vector meson V is responsible for the Q^2 dependence of the diffractive electroproduction of this vector meson is not true. Photons also couple to the continuum of hadronic states beyond ρ^0, ω, ϕ, etc.

Like VMD, GVMD postulates that the Q^2 dependence of the virtual photon cross section arises from the propagation of massive 1^--states which are 'hadronic constituents' of the photon. Different from VMD is, however, the assumption that these are not necessarily discrete vector meson states, but represent a continuum. Also, vector-meson forward scattering needs not necessarily be 'diagonal' in the masses of the incoming and outgoing particles [11]. In Ref. [12] the sum over vector-meson states in the expression for e.g. the transverse cross section $\sigma_T^{\gamma^* p}(W^2, Q^2)$ (Eq. 1.4.4) is replaced by a mass dispersion relation:

$$\sigma_T^{\gamma^* p}(W^2, Q^2) = \int dM^2 \int dM'^2\ \frac{\rho_T(W^2, M^2, M'^2) M^2 M'^2}{(Q^2 + M^2)(Q^2 + M'^2)} \ . \tag{1.5.1}$$

The double-spectral function $\rho_T(W^2, M^2, M'^2)$ is proportional to the imaginary part of the forward amplitude of the process $V + p \to V' + p$, where V and V' stand for vector states of masses M and M'. The diagonal transitions $V = V'$ and $M = M'$, corresponding to elastic Vp scattering, are known to dominate in strong interactions. The contribution of the off-diagonal transitions $V \neq V'$, $M \neq M'$, representing dissociative diffraction, is small.

Once the diagonal approximation is made, the double-spectral function simplifies to a single-spectral function:

$$\rho_T(W^2, M^2, M'^2) \sim \rho_T(W^2, M^2)\delta(M^2 - M'^2) \ . \tag{1.5.2}$$

At values of $k_t > k_0$, where the production of higher-mass $q\bar{q}$ states is possible (cf. fig 1.3.2), ρ_T can be interpreted as a probability for the photon to create a vector state of mass M multiplied by the total cross section σ_V of this (vector) $q\bar{q}$-state scattering off a nucleon [13]:

$$\rho_T(W^2, M^2) = \frac{e^2}{f_V^2}\sigma_V \ . \tag{1.5.3}$$

Note that the expression for the transverse cross section (1.5.1) together with (1.5.3) is nothing more than the continuum generalization of the transverse cross section in VMD, as given in Eq. (1.4.4). The predictions of the total virtual photon interaction cross section and of the cross-section ratio R in Ref. [13] show much better agreement with data than the corresponding VMD calculations.

The contribution of dissociative diffraction to strong interaction processes becomes significant[4] at $x \ll 1$ [12]. Therefore at low x the off-diagonal transitions should be taken into account. In Ref. [14] the contribution of off-diagonal terms to the total $\gamma^* p$ interaction cross section is calculated in the framework of pQCD. The diagonal and off-diagonal transitions are shown to interfere. This can be illustrated by the pQCD two-gluon exchange in $\gamma^* p$ scattering, represented in fig. 1.5.1.

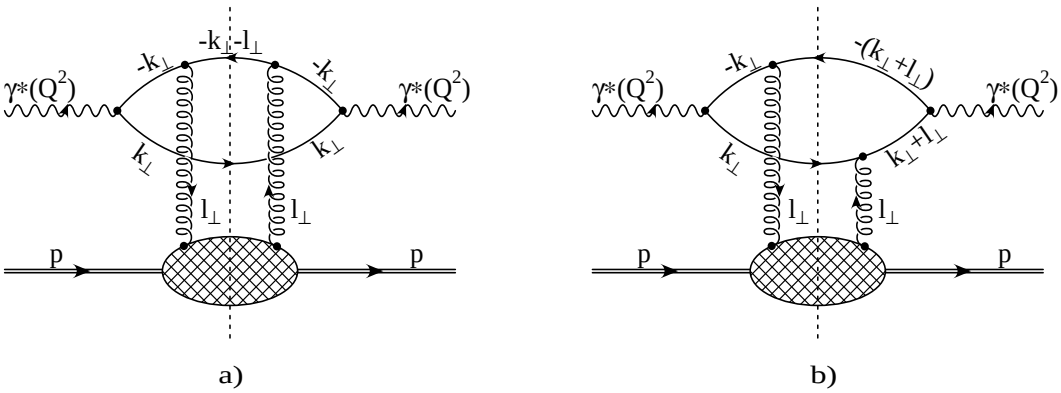

Figure 1.5.1: Diagonal a) and off-diagonal b) transitions in the two-gluon exchange [14].

The graphs depict the diagonal a) and off-diagonal b) transitions with respect to the quark transverse momenta and the masses of the incoming and outgoing $q\bar{q}$ states. The transverse momenta of the quarks, defined in the photon rest frame, are denoted as $\vec{k}_\perp$ and $\vec{k}'_\perp = \vec{k}_\perp + \vec{l}_\perp$. It is convenient to introduce a dimensionless variable z which is related to the polar production angle θ of the quark in the photon rest frame: $sin^2\theta \equiv 4z(1-z)$. In the high-energy limit z can be interpreted as the fraction of the longitudinal momentum of the $q\bar{q}$ state carried by the quark q. The masses of the incoming and outgoing $q\bar{q}$ states read:

$$M_{q\bar{q}}(\vec{k_\perp}, z) = \frac{\vec{k_\perp^2}}{z(1-z)}, \qquad M'_{q\bar{q}}(\vec{k'_\perp}, z) = \frac{(\vec{k}_\perp + \vec{l}_\perp)^2}{z(1-z)} \ . \tag{1.5.4}$$

[4] In Ref. [47] the region of applicability of the off-diagonal GVMD is limited by $x \leq 0.2$.

In the calculation of Ref. [14] the scattering is assumed to affect only the transverse momentum, while z remains unchanged. The pair of variables (k_T, z) or $(M_{q\bar{q}}, z)$ completely determines the $q\bar{q}$ state. The $q\bar{q}$-state scattering off a proton is assumed to be determined by the transverse momentum transfer $l_\perp^2$ and the photon-nucleon center-of-mass energy W^2.

The quark and the antiquark couple with opposite sign to the gluon. Therefore diagonal and off-diagonal transitions contribute with the same weight but with opposite signs. Hence, the interference between these transitions is destructive[5].

1.5.2 Application to Vector-Meson Electroproduction

The off-diagonal GVMD ansatz can be applied to the electroproduction of vector mesons. In Ref. [15] the vector-meson electroproduction cross-section is calculated assuming the coupling of the photon to a series of vector-meson states considering contributions from dissociative diffraction. For the spin-conserving part of dissociative diffraction the assumption of a power law for the forward amplitudes was made:

$$T^{Vp\to V_N p} = c_0 \cdot T^{Vp\to Vp} \cdot \left(\frac{m_1}{m_N}\right)^{2p+1} , \qquad (N = 1, 2, 3, \ldots) \ , \ p \geq 0 \ , \tag{1.5.5}$$

where $c_0 = T^{Vp\to V_1 p}/T^{Vp\to Vp}$ is the ratio of the first off-diagonal amplitude to the elastic one. The poles in the amplitude were shown to sum up approximately to a single pole with the mass m_T, different from the mass of the produced vector meson. Introduction of the off-diagonal terms does not affect the sum rule (1.4.2). In contrast, in the relation (1.4.3), when integrated over t, the terms with interfering amplitudes imply multiplication of each $\sigma^{Vp\to Vp}$ by a correction factor smaller then unity. The transverse and longitudinal amplitudes for (forward) $\gamma^* p$ interaction, as calculated in Ref. [11], read:

$$A_T^{\gamma^* p\to Vp}(W^2, Q^2, t=0) = \ m_T^2 \int_{m_T^2} \frac{dm^2}{(Q^2+m^2)^2} A^{\gamma p\to Vp}(W^2, t=0) \ , \tag{1.5.6}$$

$$A_L^{\gamma^* p\to Vp}(W^2, Q^2, t=0) = \xi_V \cdot m_L^2 \int_{m_L^2} \sqrt{\frac{Q^2}{m^2}} \frac{dm^2}{(Q^2+m^2)^2} A^{\gamma p\to Vp}(W^2, t=0) \ , \tag{1.5.7}$$

where ξ_V was taken mass independent. The threshold mass for the longitudinal amplitude, m_L, is expected to be larger than m_T : $m_T^2 < m_L^2 < m_V^2$, comparing the mass dependences of the longitudinal and transverse amplitudes of the $\gamma^* p \to Vp$ interaction. The integrated e.g. transverse cross section is then given by (cf. Eq. 1.4.4)

$$\sigma_T^{\gamma^* p\to Vp}(W^2, Q^2) = \frac{m_T^4}{(Q^2 + \ m_T^2)^2} \ \sigma^{\gamma p\to Vp}(W^2) \ , \tag{1.5.8}$$

with the prediction of the longitudinal-to-transverse ratio R calculated in Q^2-limits:

$$R(W^2, Q^2) \to \begin{cases} \frac{4}{9} \ \xi_V^2 \ \frac{Q^2}{m_L^2} & \text{for } Q^2 \ \to 0 \\ \frac{\pi^2}{4} \ \xi_V^2 \ \frac{m_L^4}{m_T^4} & \text{for } Q^2 \ \to \infty \ . \end{cases} \tag{1.5.9}$$

[5]Terms contributing with the same sign are said to interfere constructively, those with opposite signs interfere destructively.

Transverse and longitudinal cross sections are used further to determined the total GVMD cross section of vector-meson production from virtual photons (cf. Eq. 1.4.7)

$$\sigma^{\gamma^* p \to Vp}(W^2, Q^2) = \sigma_T^{\gamma^* p \to Vp}(W^2, Q^2) + \epsilon\, \sigma_L^{\gamma^* p \to Vp}(W^2, Q^2)\ . \tag{1.5.10}$$

Recalling the process classification depicted in fig. 1.3.2 an improved picture for the phase space can be drawn [7] taking into account the GVMD description of the photon interactions (fig. 1.5.2). At values of $k_\perp < k_0$ 'pure' VMD states, such as ρ^0, dominate. Though the VMD

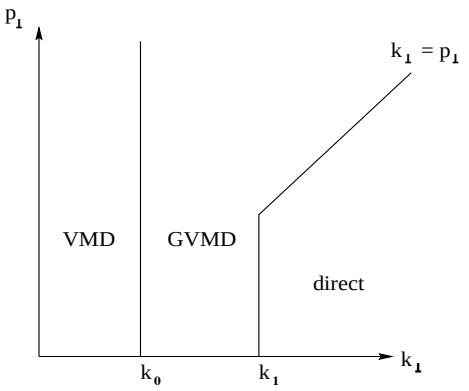

Figure 1.5.2: An alternative classification of the phase space in fig. 1.3.2

part is nothing else than a discrete diagonal approximation of the GVMD for light $q\bar{q}$ states, it is worthwhile to keep this low-Q^2 (non-perturbative) regime separate. At higher $k_\perp > k_0$ higher-mass $q\bar{q}$ states take over and off-diagonal transitions become significant. Processes at a scale $k_0 < k_\perp < k_1$ can be described in the framework of GVMD. The upper limit k_1 determines the region where the direct processes can be considered as anomalous ones due to possible diagonal and off-diagonal transitions in the interaction of the $q\bar{q}$ state and the proton.

1.6 Regge Model

Regge phenomenology was formulated first for non-relativistic scattering and was extended to high-energy physics in Ref. [16]. In this model the angular momentum l is treated as a complex variable. Therefore elastic scattering amplitudes at a fixed energy, if regarded as a function of l, have to be analytically continued into the complex l-plane. The only singularities of the scattering amplitude are so-called Regge poles. These poles are either resonances or bound states depending on the angular momentum value.

The model makes use of the principle of crossing symmetry: reaction $a + b \to c + d$ described by the s-channel variables s (energy) and t (momentum transfer) and its crossed reaction $a + \bar{c} \to \bar{b} + d$ with energy $t = \bar{s}$ and momentum transfer $s = \bar{t}$ have the same scattering amplitude, $\bar{F}\ (\bar{s},\ \bar{t}) = F\ (s,\ t)$. The scattering amplitude $F(s,t)$ has to be smooth also on non-physical sheets of the (s,t)-plane. The exchange poles in the t-channel of the reaction $a + b \to c + d$ become resonances in the s-channel of a crossed reaction.

In the Regge approach the angular momentum l can be described via a so-called Regge trajectory $\alpha(E)$ that is a complex function of the total energy: $l = Re\ \alpha(E)$. The behavior of such a trajectory is schematically shown in fig. 1.6.1. Every time the trajectory passes an

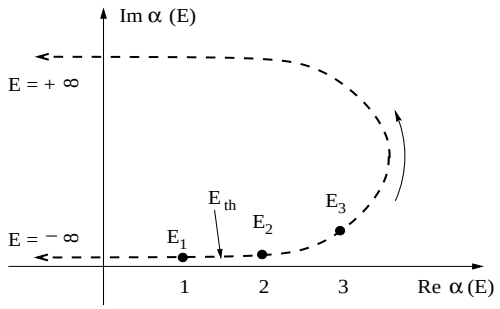

Figure 1.6.1: Typical behavior of a Regge trajectory in angular momentum space [3]. At energies $E < E_{th} = m_a + m_b$ there exists a bound state $(E_1,\ l = 1)$ corresponding to the point on the trajectory Im $\alpha(E)$=0, Re $\alpha(E)$=1. If the energy increases, the trajectory attains a positive imaginary part.

integer value in Re $\alpha(E)$, i.e. $l = n$, the state $(E_n,\ l = n)$ is possible. The amplitude $f(E, l)$ has a pole:

$$f(E,\ l = n)\ =\ -\frac{R(E)}{\varepsilon}\ \frac{1}{(E - E_n)\ +\ i\Gamma/2}\ , \tag{1.6.1}$$

$$\varepsilon \equiv \frac{d}{dE}\ Re\ \alpha(E)|_{E=E_n}; \quad \Gamma = 2/\varepsilon\ Im\ \alpha(E), \tag{1.6.2}$$

where R(E) is the residual. Eq. (1.6.1) represents a Breit-Wigner formula for a scattering amplitude near a resonance with angular momentum l and total energy E. Thus a Regge trajectory connects bound states and resonances with momentum l, being an interpolation curve between both. The number of bound states and resonances depends on the available energy of the interaction.

An important property of Regge trajectories is that all quantum numbers, apart from angular momenta, are the same for all the poles on the trajectory. The neighboring poles on the trajectory are spaced by $\Delta l = 2$. Thus the parity of the trajectory is fixed.

At low center-of-mass energies the scattering cross section in hadronic interactions is dominated by s-channel resonances. For s above 10 GeV the cross section does not depend on energy anymore and the exchange of t-poles dominates. Therefore the application of the Regge model is most useful for processes at high s and small t (diffraction). Hadron interactions at high energies can be described by the exchange of resonances in the t-channel whose interpolation is given by a Regge trajectory or Reggeon [17]. If plotted in the $(l,\ E)$ - plane, the Regge trajectories appear to be straight lines. An example of such a plot (the so-called Chew - Frautschi diagram) for several mesons is shown in fig. 1.6.2. The Regge trajectory can be parameterized as $\alpha(E)\ =\ \alpha(0) +\ \alpha'\ E$. The intercept $\alpha(0)$ and the slope α' are not predicted in the model and have to be determined from fits to experimental data.

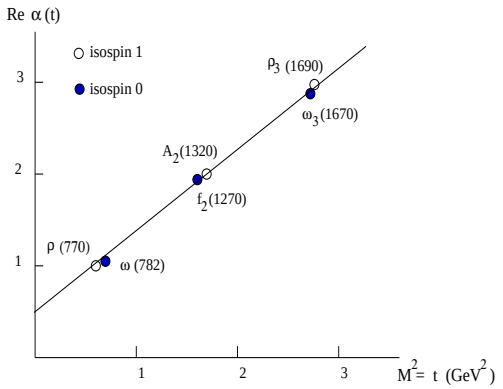

Figure 1.6.2: Chew - Frautschi diagram for a few meson resonances. The line indicates the Regge trajectories for isospin-1 and isospin-0 particles which are almost identical. The intercepts are about 0.5 and the slopes 0.9 GeV^{-2}

On the basis of the Sommerfeld-Watson representation in the complex l - plane the amplitude of the direct reaction can be represented in a form [3, 17]

$$F(s,\ t)\ =\ \frac{1}{k}\ \beta(t)\ \left(\ \frac{s}{s_0}\ \right)^{\alpha(t)}, \tag{1.6.3}$$

where a single Regge pole is assumed to dominate in the scattering process. Here k is the momentum of the elastically scattered particles in the center-of-mass frame, defined by $t = -2k^2(1 - cos\theta)$. The part of the amplitude that is independent on s is represented by $\beta(t)$ and s_0 is an energy scale factor. Using the high energy approximation $s \approx 4k^2$ at $s \to \infty$ the differential cross section corresponding to this amplitude is

$$\frac{d\sigma^{el}}{dt}\ =\ \frac{d\Omega}{dt}\ \frac{d\sigma}{d\Omega}\ =\ \frac{\pi}{k^2}\ |F(s,t)|^2\ , \tag{1.6.4}$$

$$\frac{d\sigma^{el}}{dt}\ =\ 16\ \pi\ \beta^2(t)\ \left(\frac{s}{s_0}\right)^{2\alpha(t)-2}\ . \tag{1.6.5}$$

The total cross section can be obtained from the optical theorem

$$\sigma^{tot}\ =\ \frac{4\ \pi}{k}\ Im\ F(t=0)\ \propto\ \left(\frac{s}{s_0}\right)^{2\alpha(0)-2}\ . \tag{1.6.6}$$

The behavior of the hadron-hadron cross section at high energies requires a trajectory with $\alpha(0)\ \approx\ 1$, and with the vacuum quantum numbers, as no quantum numbers may be exchanged in elastic processes. For all other Regge trajectories the intercepts are smaller than unity, so the vacuum trajectory dominates at high energies. Vacuum-pole exchange implies $\sigma_{ab}\ =\ \sigma_{\bar{a}b}$. This follows from the Pomeranchuk theorem, hence the vacuum trajectory is also called 'Pomeron' trajectory, with $\alpha_{\mathbf{P}}(0)\ =\ 1\ +\ \zeta, 0\ <\ \zeta\ \ll\ 1$.

Total hadron-hadron and photon-hadron cross sections can be described by a sum of Reggeon and Pomeron terms:

$$\sigma^{tot}\ =\ X\ s^{\epsilon}\ +\ Y\ s^{-\eta}\ . \tag{1.6.7}$$

The effective powers of Pomeron and Reggeon exchange, ϵ and η, respectively, can be determined from fits to experimental data and are assumed to be independent of the interacting hadrons, while the normalizations X and Y do depend on the process. In Ref. [18] the values of $\epsilon = \alpha_{\mathbf{P}} - 1 = 0.0808$ and $\eta = \alpha_R - 1 = 0.4525$ are reported for proton-proton and proton-antiproton scattering at $\sqrt{s} = 10$ GeV. The effective power ϵ is thought to be somewhat smaller than $\alpha(0) - 1$ because the term includes also multi-Pomeron exchange.

The differential cross section of diffractive processes falls exponentially with $|t|$, so the parameterization $|\beta(t)|^2 \sim e^{b_0 t}$ can be used which gives for the differential cross section:

$$\frac{d\sigma}{dt} \propto e^{b_0 t} \left(\frac{s}{s_0}\right)^{2\alpha(t)-2} = \left(\frac{s}{s_0}\right)^{2\alpha(0)-2} e^{b_0 + 2\alpha' ln(s/s_0)} = \frac{d\sigma}{dt}\Big|_{t=0} e^{-b|t|} , \qquad (1.6.8)$$

where $b = b_0 + 2\alpha' \, ln\left(\frac{s}{s_0}\right)$. At small negative values of t the expression (1.6.8) describes the behavior of the elastic cross section with increasing momentum transfer. Regge theory also predicts that the slope of the forward diffractive peak increases with energy (shrinkage effect). Measurements of this effect are used to extract the slopes of the exchanged Regge trajectory. The slope of the Pomeron trajectory was determined to be $\alpha'_{\mathbf{P}} = 0.25$ GeV^{-2} and that of the Reggeon one $\alpha'_R = 0.93$ GeV^{-2} [19].

1.7 Generalized Parton Distributions

The measurement of hard exclusive processes in the Bjorken limit of high Q^2 at fixed x and small fixed t appears to be a promising tool to study the details of the nucleon structure that can not be accessed with inclusive DIS. The formalism of generalized parton distributions (GPDs) [20, 21] provides a unified theoretical description of hard exclusive and inclusive processes.

The idea of this unification can be explained by a comparison of DIS and the exclusive process of deeply virtual Compton scattering (DVCS) [22].

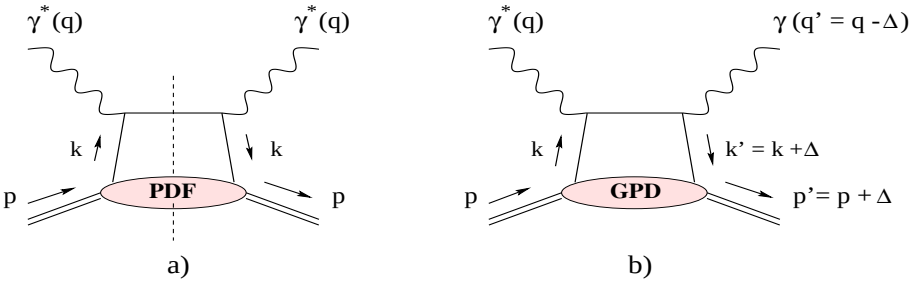

Figure 1.7.1: Born-level diagrams for a) forward Compton amplitude and b) DVCS. The nucleon structure depicted as blobs is described by PDFs and GPDs, respectively.

The cross section of the inclusive DIS process $\gamma^* \, p \rightarrow X$ is related through the optical theorem to the forward amplitude of the elastic reaction $\gamma^* \, p \rightarrow \gamma^* \, p$, shown in fig. 1.7.1 a). The nucleon structure in this case is described by parton distribution functions (PDFs).

No momentum is transfered across the cut in the graph, the parton lines connected to the nucleon carry the same momenta k or momentum fractions x.

The graph representing the DVCS process $\gamma^*\ p \rightarrow\ \gamma\ p$ is shown in fig. 1.7.1 b). The virtual photon on the right side is now replaced by a real one. In this case the momentum transfer $t = \Delta^2 = (p' - p)^2 = (q - q')^2 < 0$ from the left to the right side of the diagram is non-zero. The parton lines now have different momenta thereby introducing a disbalance or skewedness in the graph. In the Bjorken limit the DVCS amplitude can be factorized into a hard-scattering part calculable in pQCD and a non-perturbative part describing the nucleon structure in terms of GPDs.

Production of vector mesons from longitudinal photons in the limit of high Q^2 and small t is illustrated in fig. 1.7.2. The factorization theorem [23] implies that the amplitude of the process can be described by three components: the hard scattering part, the quark-antiquark distribution amplitude of the meson and the generalized quark a) or gluon b) distributions in the nucleon. In leading order QCD the structure of the nucleon can be expressed in terms

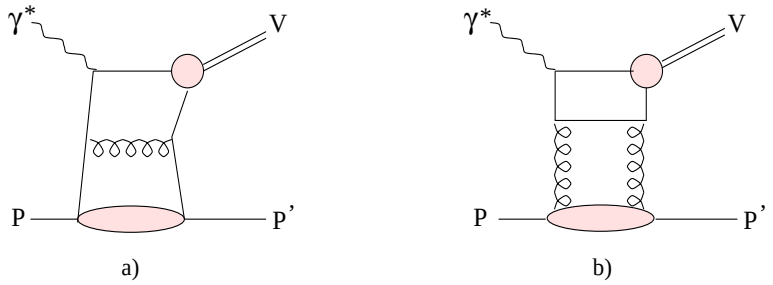

Figure 1.7.2: Born-level diagrams contributing to vector-meson production from longitudinal photons [24], involving generalized a) quark and b) gluon distributions.

of four GPDs per flavor: unpolarized GPDs H_f, E_f and polarized GPDs $\tilde{H}_f$, $\tilde{E}_f$. These are functions of four independent kinematic variables: Q^2, x, ξ and $\Delta^2 = t < 0$. These variables are defined in a frame where the momenta of the virtual photon q^μ and the nucleon p^μ are anti-parallel, so that the transverse momenta are zero.

Physical momenta are expressed in terms of light-cone vectors[6] $p^\mu = P^+/\sqrt{2}\cdot(1,0,0,0)$ and $n^\mu = 1/\sqrt{2}P^+ \cdot (1,0,0,-1)$. The internal variables x, x' stand for the light-cone momentum fractions of the exchanged partons with respect to the incoming nucleon. These are defined by the longitudinal momenta of the partons k, k'. The longitudinal momentum fraction ξ describes the 'skewedness' of the interaction

$$x = \frac{k}{P^+}, \quad x' = \frac{k'}{P^+}, \quad \xi = -\Delta P^+ \ . \tag{1.7.1}$$

In the Bjorken limit it holds $2\xi \rightarrow x_B/(1 - x_B/2)$, where x_B is the Bjorken-x variable. The difference between the parton fractional momenta is $x - x' \approx x_B$.

Ordinary parton distribution functions are matrix elements of an operator between identical nucleon states and represent the squared amplitude or probability for a nucleon to emit

[6]The light-cone coordinates are defined as $m^\pm = 1/\sqrt{2}(m^0 \pm m^3)$, the role of time played by m^+.

a parton of a given flavor f with the momentum fraction x. GPDs are matrix elements of the same operators but between different nucleon states. They represent the amplitude for a nucleon to emit a parton with a momentum fraction x times the conjugated amplitude of absorption of a parton with a momentum fraction x'. In the forward limit the GPDs H_f, $\tilde{H}_f$ reduce to unpolarized and polarized PDFs respectively:

$$H_f(x, \xi = 0, t = 0) = q_f(x), \quad \tilde{H}_f(x, , \xi = 0, t = 0) = \Delta q_f(x) \tag{1.7.2}$$

At finite momentum transfer and after summation over the quark flavors (depending on the nucleon type) the first moments of GPDs are related to elastic Dirac, Pauli, axial-vector and pseudo-scalar form factors, respectively:

$$\begin{aligned} \int_{-1}^{+1} dx H(x, \xi, t) &= F_1(|t|), \quad \int_{-1}^{+1} dx E(x, \xi, t) = F_2(|t|), \\ \int_{-1}^{+1} dx \tilde{H}(x, \xi, t) &= G_A(|t|), \quad \int_{-1}^{+1} dx \tilde{E}(x, \xi, t) = G_P(|t|). \end{aligned} \tag{1.7.3}$$

For a given flavor f the second moments of the unpolarized GPDs in the forward limit are relevant to the total quark angular momentum [20]:

$$J_f = \frac{1}{2} \int_{-1}^{1} x \; dx \; [H^f(x, \xi, t = 0) + E^f(x, \xi, t = 0)] \; . \tag{1.7.4}$$

The total quark angular momentum decomposes as $J_q = \frac{1}{2}\Delta\Sigma + L_q$. Here $\Delta\Sigma/2$ and L_q are the intrinsic quark spin and quark orbital angular momentum, respectively. The total quark contribution $\Delta\Sigma$ has been measured in polarized DIS experiments. A measurement of J_q through Eq. (1.7.4) makes it in principle possible to determine the contribution of the quark orbital momentum to the nucleon spin. Eventually the contribution of the total gluon angular momentum J_q may become accessible, since $J_g = \frac{1}{2} - J_q$.

1.8 Cross Section of Vector-Meson Production

1.8.1 GVMD Prediction

In Ref. [11] the Q^2-dependence of the total cross section (1.5.10) and of the ratio R (1.5.9) for electroproduction of ρ^0 and ϕ-mesons is fitted to the data of HERA collider experiments at $W = 50$ GeV and 80 GeV, respectively. The fits depend on four parameters: the effective masses m_L, m_T of the vector meson, the ratio ξ_V, and the photoproduction cross section $\sigma^{\gamma p \to Vp}$ (Eq. (1.5.8) at $Q^2 = 0$). The calculations agree well with the data (fig. 1.8.1) and the following values of the fit parameters were obtained:

$$\begin{aligned} \xi_\rho = 1.06 \; , \quad m^2_{T,\rho} = 0.68 m^2_\rho \; , \quad m^2_{L,\rho} = 0.71 m^2_\rho \; , \quad \sigma^{\gamma p \to \rho p} = 11.1 \; \mu b, \\ \xi_\phi = 0.90 \; , \quad m^2_{T,\phi} = 0.43 m^2_\phi \; , \quad m^2_{L,\phi} = 0.60 m^2_\phi \; , \quad \sigma^{\gamma p \to \phi p} = 1.2 \; \mu b. \end{aligned}$$

The total cross section shows the asymptotic $1/Q^2$ behavior. The fitted values of the effective masses show the theoretically expected ordering: $m_T < m_L < m_{VM}$. The solid

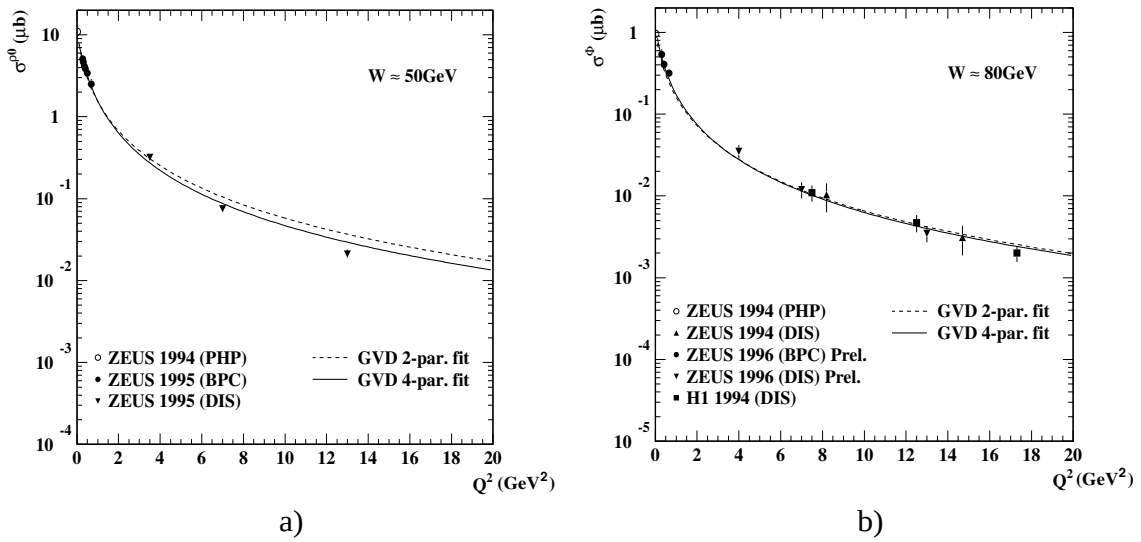

Figure 1.8.1: GVMD prediction of the Q^2-dependence of the cross section of a) ρ^0-meson and b) ϕ-meson electroproduction compared with HERA collider data. The solid and dashed lines represent 4-parameter and 2-parameter fits, respectively. The figure is taken from Ref. [11].

line in fig. 1.8.1 represents the 4-parameter fit to the data, performed separately for ρ- and ϕ-mesons. The dashed line shows the 2-parameter fit where ξ and mass parameters are fixed: $\xi = 1$, $m^2_{V,L} = 1.5\ m^2_{V,T}$ (corresponding to the asymptotic value of R). The following relations are obtained:

$$m^2_{\rho,T} = 0.62 m^2_{\rho}, \qquad m^2_{\phi,T} = 0.40 m^2_{\phi}\ .$$

It was also observed, that the ratio R becomes independent on Q^2 at high Q^2 [11] (cf. Eq. (1.5.9)). Considering the agreement between the data and the model it is concluded that indeed the propagation of hadronic spin-1 states and the destructive interference between diagonal and off-diagonal transitions govern the Q^2 dependence of exclusive electroproduction of vector mesons at small[7] x.

1.8.2 Regge-based Models

In Ref. [25] the photoproduction of light vector mesons at laboratory energies of about 50 GeV is explained by Pomeron exchange, while at lower energies the exchange of other trajectories dominates. The parameterization (1.6.7) is used for the calculation of the vector-meson photoproduction cross section. The additive quark model, where the single Pomeron couples to a single quark in the nucleon, is assumed and diagonal VMD is considered. The forward amplitude of $\rho^0 p$ scattering is taken as the average of the forward amplitudes for $\pi^- p$ and $\pi^+ p$ scattering, implying for the cross section:

$$\sigma^{\rho^0 p} \approx \frac{1}{2}(\sigma^{\pi^+ p} + \sigma^{\pi^- p}). \tag{1.8.1}$$

[7]The requirement of small x implies here $x \approx \frac{Q^2}{W^2} \ll 1$. In Ref. [47] the x-region where GVMD can be used is extended up to $x < 0.2$

The resulting total cross section of $\rho^0 p$ scattering (in millibarn) is

$$\sigma^{tot}(\rho^0 p) = 13.6\ s^{0.08} + 31.8\ s^{-0.45}.$$

For the $\gamma\rho^0$ coupling constant f_ρ the value of 5.043 was obtained. The energy behavior observed in the HERA data is well described by this parameterization, but the normalization appeared to be too high.

Unlike Ref. [25] the model of Ref. [26] postulates that the Pomeron singularity is not a simple pole with a fixed intercept $\alpha_{\mathbf{P}}(0)$, but instead multiple Pomeron exchanges must be considered. An effective intercept Δ^{eff} was introduced, yielding the value of ≈0.08 for real photons and ≈0.24 for high photon virtualities $Q^2 \gg 1$ GeV^2. In this approach

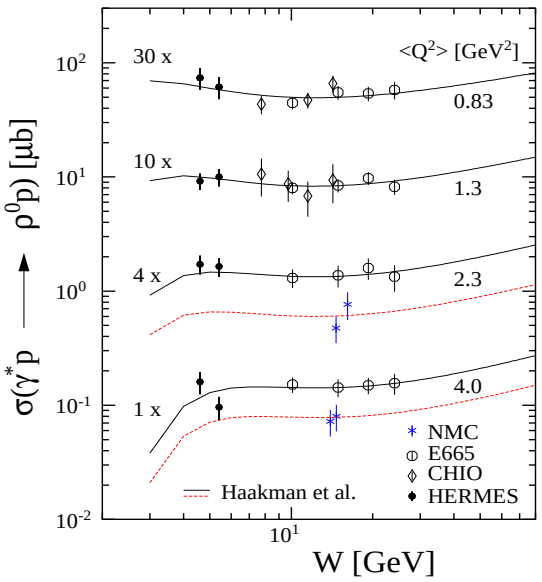

Figure 1.8.2: Prediction of Ref. [26] for the W-dependence of the cross section of ρ^0 electroproduction compared with world data at average Q^2 values of 0.83, 1.3, 2.3 and 4 GeV^2. Both data and calculation have been multiplied by factors indicated on the left of the figure. The plot is taken from Ref. [27].

the W-dependence of the $\gamma^* p$ cross section is described through the $(x,\ Q^2)$-dependent electromagnetic structure function F_2 of the nucleon:

$$\sigma^{\gamma^* p} = \frac{4\pi^2 \alpha_{em}}{Q^2(1-x)} F_2(x, Q^2).$$

The cross section of vector-meson production through Pomeron exchange is written as

$$\frac{d\sigma}{dt} = \Phi(Q^2, M_V)\ F_2(x, Q^2)^2\ e^{\Lambda(W)t},$$

where the scaling function Φ is unknown and has to be fitted to the data.

The slope parameter Λ of the diffraction cone and the radius R of the (γVp) vertex are defined as

$$\Lambda(W) = 2\left(R^2 + \alpha'_{\mathbf{P}}\ ln\left(\frac{W}{W_0}\right)\right), \quad \text{with} \quad W_0 = m_V^2 + Q^2,$$
$$R^2 = R_p^2 + R_V^2(Q^2),\ R_V^2 = \frac{R_0^2 V\ m_\rho^2}{m_V^2 + Q^2}.$$

The production of light vector mesons containing u and d quarks (ρ^0, ω) at high energies is thought to be described by dominant Pomeron exchange, while at low energies the Reggeon exchange dominates. In the intermediate energy regime of HERMES both Pomeron and Reggeon exchange are expected to contribute.

In Ref. [27] the predicted W-dependence of the ρ^0 production cross section was compared in particular to HERMES measurements. The calculation was normalized to HERMES and E665 data, separately for each Q^2-bin. The results are shown in fig. 1.8.2. The data are well described by the model down to W=4 GeV. For even lower W, however, HERMES data at $W < 4$ GeV show that the cross section is slowly rising with decreasing W (cf. fig. 3 of Ref. [27]), a feature that is not reproduced by the calculation of Ref. [26].

1.8.3 GPD-based Model

The description of vector-meson production from longitudinal photons involves the unpolarized GPDs H and E. First calculations of DVCS and meson leptoproduction in the Bjorken limit in terms of GPDs are presented in Ref. [28, 29]. These calculations were restricted to the near-to-forward directions. A comparison with data is given in Ref. [29] and Ref. [27].

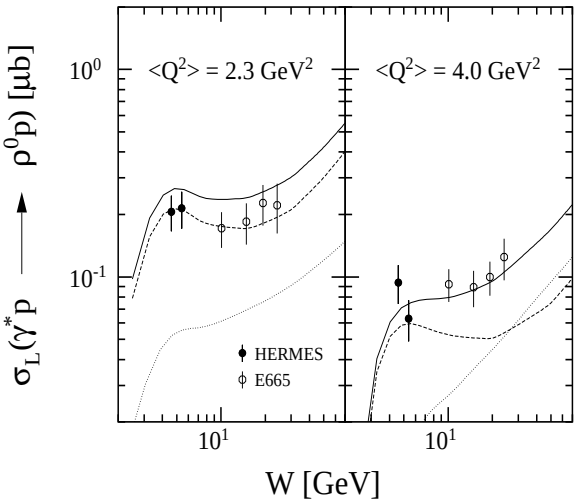

Figure 1.8.3: Prediction (solid lines) of Ref. [28, 29] for the W-dependence of the longitudinal cross section of ρ^0-meson electroproduction, compared with HERMES and E665 data at average Q^2 values of 2.3 (left), and 4.0 GeV^2 (right). The dashed and dotted curves represent the quark and two-gluon exchange, respectively. The plot is taken from Ref. [27].

At $W > 10$ GeV the perturbative two-gluon exchange mechanism is predicted to dominate for $Q^2 \geq 6$ GeV^2. At lower W the quark-exchange mechanism is expected to contribute. In fig. 1.8.3 the calculated cross sections corresponding to these two mechanisms and their incoherent sum are compared to longitudinal ρ^0-production cross sections measured at HERMES and E665 at two average values of Q^2.

Indeed, in the HERMES kinematic domain the quark exchange dominates and only at $Q^2 = 4$ GeV^2 and $W > 10$ GeV the gluon exchange contribution becomes significant.

Note that the factorization theorem implies (yet) only longitudinal photons. At HERMES energies, however, the cross section is not purely longitudinal. Hence, the total cross section of exclusive vector-meson electroproduction can not (yet) be properly described in terms of GPDs.

Chapter 2

Vector-Meson Polarization

Interactions of a longitudinally polarized beam lepton with an unpolarized or longitudinally polarized target nucleon can be used to tag the spin dependence of vector-meson production. The matrix element describing the scattering process for polarized beam and unpolarized target contains the photon and vector-meson spin density matrices. The vector-meson spin density matrix elements can be determined from measured production and decay angles of the vector meson. The spin density matrix elements of the vector meson contain the information about the parity of the object exchanged with the target nucleon.

2.1 Formalism

The basics of the analysis of vector-meson production in polarized lepton - nucleon scattering are given in Ref. [30] with the formalism of the polarization studies been thoroughly described in Ref. [31]. The case of a longitudinally polarized target is dealt with in Ref. [32]. The definitions throughout this chapter follow those in the work by Schilling and Wolf [31].

The helicity dependence of vector-meson production in inelastic lepton - nucleon scattering, depicted in fig. 1.1.1 b), is studied in a hadronic center-of-mass frame referred to as hadronic frame and defined by an orthogonal set of unit vectors:

$$\vec{Z} = \frac{\vec{q}^*}{|\vec{q}^*|}, \quad \vec{Y} = \frac{\vec{q}^* \times \vec{v}^*}{|\vec{q}^* \times \vec{v}^*|}, \quad \vec{X} = \vec{Y} \times \vec{Z} \; . \tag{2.1.1}$$

The s-channel helicity frame is defined by an implicit assumption made on the hadronic frame, namely that there is no orbital momentum in the $\gamma^* N$ system. With this assumption, the virtual photon and the nucleon collide head-on. The spin-polarization axis of the vector meson is taken to be in the direction of the vector meson.

The process $l N \rightarrow V N$ is defined by the meson production angle Φ and the meson decay angles ϕ and θ, drawn in fig. 2.1.1 for the case of ρ^0 production.

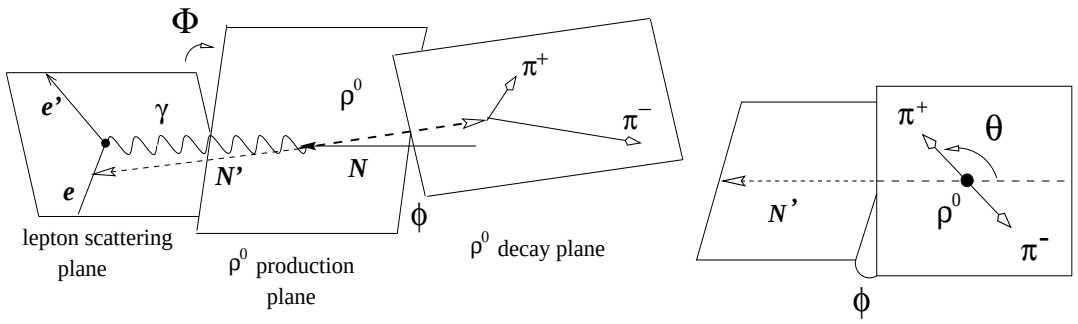

Figure 2.1.1: Angles used in the ρ^0 polarization analysis. Φ is the angle between the lepton scattering plane and the hadron production plane. The decay angles θ and ϕ are the polar and azimuthal angles of the π^+ in the ρ^0 rest frame.

The azimuthal production angle Φ between the normals to the leptonic plane $\vec{n_l}$ and the hadron production plane $\vec{Y}$ reads

$$cos\ \Phi\ =\ \vec{n_l}\vec{Y}, \qquad sin\ \Phi = \frac{((\vec{Y}\times n_l)\times\vec{Y})\ \vec{n_l}}{(\vec{Y}\times n_l\times\vec{Y})}, \quad \text{where} \quad \vec{n_l}\ =\ \frac{\vec{k_1}^*\times\vec{k_2}^*}{|\vec{k_1}^*\times\vec{k_2}^*|}\ . \tag{2.1.2}$$

The decay distribution of the vector meson is described in the vector-meson rest frame using the s-channel helicity frame with the z-axis opposite to the direction of the outgoing nucleon in the center-of-mass frame $\{\ \vec{z} = -\frac{\vec{p'}^*}{|\vec{p'}^*|},\ \vec{y} = \vec{Y},\ \vec{x} = \vec{y}\times\vec{z}\ \}$. The polar and azimuthal decay angles θ and ϕ can be determined via the unit vector $\vec{n}_d$ which points along the momentum of the positively charged decay particle in case of a 2-body decay[1]

$$cos\ \theta\ =\ \vec{n_d}\vec{z}, \quad cos\ \phi\ =\ \frac{\vec{y}(\vec{z}\times\vec{n}_d)}{|\vec{z}\times\vec{n}_d|}, \quad sin\ \phi = -\frac{\vec{x}(\vec{z}\times\vec{n}_d)}{|\vec{z}\times\vec{n}_d|}\ . \tag{2.1.3}$$

The vector-meson production angle with respect to the direction of the virtual photon is

$$cos\ \theta^*_V\ =\ \frac{\vec{q}^*\vec{v}^*}{|\vec{q}^*||\vec{v}^*|}\ . \tag{2.1.4}$$

2.2 The Photon Spin Density Matrix

The differential cross section of vector-meson production in lepton-nucleon scattering can be written as

$$\frac{d\sigma^{eN\to e'N'V}}{dE'd\Omega'd\Phi dt} = \frac{1}{(2\pi)^5}\ \frac{E'}{E}\ \frac{m^2}{4(v^2+Q^2)^{1/2}}\ \frac{1}{Q^4}\ \frac{1}{4}\ \sum_{spins}|\mathcal{M}|^2\ . \tag{2.2.1}$$

Here $d\Omega'$ is the volume element of the scattered lepton and $\mathcal{M}$ is the matrix element describing the scattering process. In the one-photon exchange approximation the matrix element reads:

$$\mathcal{M} = e^2 < k'|j^e_\mu|k > \cdot < p'v|j^{e,\mu}|p > =\ e^2 j_\mu \cdot J^\mu, \tag{2.2.2}$$

[1]In case of a 3 - body decay $\vec{n}_d$ points along the normal to the decay plane.

where e is the elementary charge, j^μ and J^μ are the matrix elements of the electromagnetic current operator j^e_μ between the lepton and hadron states, respectively. For unpolarized leptons the matrix element can be expressed in terms of leptonic and hadronic tensors $L_{\mu\nu}$ and $T^{\mu\nu}$, respectively

$$\frac{1}{4}\sum_{spins}|\mathcal{M}|^2 \;=\; \frac{1}{4}\sum_{spins} L_{\mu\nu}T^{\mu\nu} \tag{2.2.3}$$

The leptonic tensor $L_{\mu\nu}$ contains the information regarding the photon polarization and therefore is called the photon spin density matrix. It contains transverse (x, y), longitudinal (z) and scalar (0) components. It can be evaluated in a coordinate system, where the z-axis points along $\vec{q} = \vec{k} - \vec{k'}$ and $\vec{k}$, $\vec{k'}$ lying in the (x, z) plane. The longitudinal and scalar components are treated as a single entity, as they transform into each other under the Lorentz transformation along $\vec{q}$, while the transverse polarization remains unchanged. The photon density matrix is shown to be invariant under the Lorentz boost. Therefore it can be evaluated in the Breit frame[2], resulting in the 3×3 matrix $L_{\mu\nu}$. This matrix can be expressed in terms of the polarization parameter ϵ and the electron mass correction $\delta_e = \frac{2m_e^2}{Q^2}(1-\epsilon)$ which can be neglected at $Q^2 \gg m_e$. Transformed into the hadronic frame, the photon density matrix has the form

$$L_{\lambda\lambda'}(\epsilon, \delta_e, \Phi) \;=\; U_{\lambda\mu}L_{\mu\nu}U^{-1}_{\nu\lambda}, \tag{2.2.4}$$

where λ denotes the photon helicity and the matrices $U_{\mu\nu}$ describe the rotation around Z through the angle Φ.

For polarized incident leptons the photon density matrix $\tilde{L}_{\mu\nu}$ is given by the sum of unpolarized and polarized density matrices

$$\tilde{L}_{\mu\nu} = L_{\mu\nu} + M_{\mu\nu}, \quad M_{\mu\nu} = im_e\ \epsilon_{\mu\nu\rho\sigma}q^\rho P^\sigma, \tag{2.2.5}$$

where m_e is the lepton mass, P^μ represents the lepton polarization vector and $\epsilon_{\mu\nu\rho\sigma}$ is the total anti-symmetric Levi-Cevita tensor. Like $L_{\mu\nu}$ the matrix $M_{\mu\nu}$ is invariant under the Lorentz boost along $\vec{q}$ and can be represented in the hadronic frame dependent on ϵ, δ_e and Φ. Normalized to a unit flux of transverse photons, the photon density matrix $\rho(\gamma)$ reads

$$\rho(\gamma)_{\lambda\lambda'} = \frac{1-\epsilon}{Q^2}\Big(L_{\lambda\lambda'} + M_{\lambda\lambda'}\Big), \tag{2.2.6}$$

and can be decomposed into an orthogonal set of independent hermetian matrices Σ^α

$$\rho(\gamma)_{\lambda\lambda'} = \frac{1}{2}\sum_{\alpha=0\ldots8}\tilde{\Pi}_\alpha\Sigma^\alpha\ . \tag{2.2.7}$$

The vector $\tilde{\Pi}_\alpha$ is a function of ϵ, δ_e, Φ and P_μ. The matrices Σ^α describe the polarization state of the photon. The transverse photon contribution is given by $\alpha = 0..3$ with the

[2]The Breit frame is defined from either the *lab* frame or the hadronic frame by a boost along $\vec{q}$, with the lepton scattered elastically backwards with the same energy as before the interaction.

unpolarized part ($\alpha = 0$), the linear ($\alpha = 1,\ 2$), and – in case of polarized leptons – circular ($\alpha = 3$) polarization. Longitudinal photons are represented by $\alpha = 4$. Longitudinal-transverse interference terms are given by $\alpha = 5,\ 6$ for unpolarized leptons and $\alpha = 7,\ 8$ for polarized leptons. The following symmetry properties of the matrices $M_{\lambda\lambda'}$ and $L_{\lambda\lambda'}$ should be noticed

$$M_{-\lambda-\lambda'} = -(-1)^{\lambda-\lambda'} L_{\lambda'\lambda}, \quad L_{-\lambda-\lambda'} = (-1)^{\lambda-\lambda'} L_{\lambda'\lambda}\ . \tag{2.2.8}$$

The matrices $\Sigma^{3,7,8}$ obey the symmetry properties of $M_{\lambda\lambda'}$, the remaining Σ^{α} follow those of $L_{\lambda\lambda'}$.

2.3 Vector-Meson Spin Density Matrix

The hadronic vertex of vector-meson leptoproduction can be expressed in terms of Jacob-Wick helicity amplitudes for the process $\gamma^* N \to V N$:

$$T^{\lambda_{N'}\lambda_V}_{\lambda_N\lambda_\gamma}(\theta^*_V) = < \lambda_V \lambda'_N | j_{\lambda_\gamma} | \lambda_N >, \tag{2.3.1}$$

$$\text{with} \quad j_{\lambda_\gamma=\pm1} = j_x \pm j_y, \quad j_{\lambda_\gamma=0} = j_z.$$

As a consequence of parity conservation the helicity amplitudes show the following symmetry relation:

$$T^{-\lambda_{N'}-\lambda_V}_{-\lambda_N-\lambda_\gamma} = (-1)^{(\lambda_V-\lambda_{N'})-(\lambda_\gamma-\lambda_N)} T^{\lambda_{N'}\lambda_V}_{\lambda_N\lambda_\gamma}. \tag{2.3.2}$$

2.3.1 Polarized Lepton, Unpolarized Nucleon

In case of an unpolarized target the nucleon helicities can be summed over. In the following, if not explicitly mentioned, the summation over nucleon helicities is always performed. The cross section of the process $\gamma^* N \to V N$ is given by

$$\frac{d\sigma^{\gamma^* N \to V N}}{dt d\Phi} \ = \ \frac{1}{32\pi^2(\nu^2+Q^2)} \ \frac{1}{2} \ Tr\ (T\rho(\gamma)T^+), \tag{2.3.3}$$

or expressed in terms of longitudinal and transverse production cross sections σ_L and σ_T, respectively, after integration over Φ

$$\frac{d\sigma^{\gamma^* N \to V N}}{dt} \ = \ \frac{d\sigma_T^{\gamma^* N \to V N}}{dt} + (\epsilon + \delta_e) \frac{d\sigma_L^{\gamma^* N \to V N}}{dt}\ . \tag{2.3.4}$$

The normalized spin density matrix of the vector meson is derived as

$$\rho(V) = \frac{1}{2}\ T\rho(\gamma)T^+ / \int \frac{d\Phi}{2\pi}\ Tr(T\rho(\gamma)T^+) \tag{2.3.5}$$

Like the photon density matrix $\rho(\gamma)$ the vector-meson density matrix can be decomposed into hermetian matrices

$$\rho(V) = \sum_{\alpha=0\ldots8} \Pi_\alpha \rho^\alpha, \tag{2.3.6}$$

$$\text{with elements} \quad \rho^\alpha_{\gamma_V\gamma'_V} = \frac{1}{2N_\alpha} \sum_{\lambda_{N'},\lambda_N,\lambda_\gamma,\lambda'_\gamma} T^{\lambda_{N'}\lambda_V}_{\lambda_N\lambda_\gamma} \Sigma^\alpha_{\lambda_\gamma\lambda'_\gamma} T^{\lambda_{N'}\lambda_V}_{\lambda_N\lambda_\gamma}\ . \tag{2.3.7}$$

Here N_α are normalization factors and the vector Π_α is a function of ϵ, δ_e, Φ, the longitudinal-to-transverse cross section ratio $R = \sigma_L/\sigma_T$, and the lepton polarization vector in the Breit system. From Eq. (2.3.7) it is clear how different components of the photon spin density matrix contribute to the vector-meson density matrix. The symmetry relations

$$\rho^\alpha_{-\lambda-\lambda'} = \begin{cases} (-1)^{\lambda-\lambda'}\rho^\alpha_{\lambda\lambda'} & \alpha = 0,1,4,5,8 \\ -(-1)^{\lambda-\lambda'}\rho^\alpha_{\lambda\lambda'} & \alpha = 2,3,6,7, \end{cases} \tag{2.3.8}$$

following from the symmetry properties of helicity amplitudes and photon density matrices, reduce the number of independent matrix elements.

2.3.2 s-Channel Helicity Conservation

The concept of s-channel helicity conservation (SCHC) implies that the helicity of the photon is preserved by the vector meson in the s-channel helicity frame. In terms of helicity amplitudes this means that helicity non-conserving amplitudes become zero:

$$T^{\lambda_{N'}\lambda_V}_{\lambda_N\lambda_\gamma} \Rightarrow T^{\lambda_{N'}\lambda_V}_{\lambda_N\lambda_\gamma}\delta_{\lambda_V\lambda_\gamma} \ . \tag{2.3.9}$$

This leaves only three independent amplitudes T^0_0, T^1_1 and T^{-1}_{-1}, where nucleon helicities are omitted.

2.3.3 Parity of the Exchange

The photon-nucleon interaction can be explained to proceed via t-channel exchange of particles or particle systems. These particles can have natural or unnatural parity, $P = (-1)^J$ and $P = -(-1)^J$, respectively. Introducing the parity of the exchange another symmetry property of helicity amplitudes can be obtained

$$T^{\lambda_{N'}-\lambda_V}_{\lambda_N-\lambda_\gamma} = \pm(-1)^{(\lambda_V-\lambda_\gamma)} = T^{\lambda_{N'}\lambda_V}_{\lambda_N\lambda_\gamma}. \tag{2.3.10}$$

This relation is valid to leading order in s. The sign applies to natural (+) and unnatural (–) parity exchange. Representing the helicity amplitudes as a sum of contributions of natural- and unnatural-parity exchange and considering the symmetry properties of the Σ^α the vector-meson spin density matrix can be written in the form

$$\rho^\alpha_{\lambda\lambda'} = \rho^{\alpha n}_{\lambda\lambda'} + \rho^{\alpha u}_{\lambda\lambda'} \ . \tag{2.3.11}$$

It is essential that in Eq. (2.3.11) there are no interference terms between contributions from natural and unnatural parity exchange in the helicity amplitudes. This, however, holds only for the unpolarized nucleon.

Only a measurement of the complete set of density matrices ρ^α makes it possible to separate the contributions from natural- and unnatural-parity exchange.

SCHC with the assumption that only natural parity has been exchanged leaves only two independent amplitudes, e.g. T^0_0 and T^1_1. Introducing their phase difference δ results in

$$T^0_0\ T^{1*}_1 \ = \ |T^0_0|\ |T^1_1|\ e^{-i\delta} \ . \tag{2.3.12}$$

It should be noticed that natural-parity exchange is consistent with Pomeron exchange, while unnatural-parity exchange can be mediated by di-quark objects. Unnatural-parity exchange in vector-meson electroproduction at small $|t| < 0.08$ GeV^2 is discussed in Ref. [32] in the framework of the One-Pion Exchange model.

2.3.4 Angular Distributions

The vector-meson decay angular distribution in terms of the spin density matrix and decay amplitude M reads

$$W(cos\ \theta, \phi) = \sum_{\lambda_V \lambda_{V'}} < \theta, \phi | M | \lambda_V > \rho(V)_{\lambda_V \lambda_{V'}} < \lambda'_V | M^+ | \theta, \phi > \ . \tag{2.3.13}$$

The Wigner functions $D^j_{ab}(\phi, \theta)$ describe a state with total angular momentum j and give the probability that a state $< ab|$ is transformed into a state $< ab'|$ after a rotation (ϕ, θ). The angular distribution $W(cos\ \theta, \phi)$ can be expressed in terms of spin-1 functions $D^1_{\lambda_V 0}(\phi, \theta)$. It can be then interpreted as a probability of a spin-1 vector meson decaying into spin-0 pseudoscalar mesons at angles (θ, ϕ)

$$\begin{aligned} W(cos\ \theta, \phi, \Phi) &= \sum_{\alpha=0...8} \Pi_\alpha \left(\frac{3}{4\pi} \sum_{\lambda_V \lambda'_V} D^1_{\lambda_V 0}(\phi, \theta, -\phi)^* \rho^\alpha_{\lambda_V \lambda'_V} D^1_{\lambda'_V 0}(\phi, \theta, -\phi) \right) \\ &= \sum_{\alpha=0...8} \Pi_\alpha W^\alpha(cos\ \theta, \phi, \Phi) \ . \end{aligned} \tag{2.3.14}$$

This expression can be split up into two parts, one depending on the beam polarization and the other one not.

In case of unpolarized leptons it is in general possible to measure 20 independent real quantities: the transverse and longitudinal photon cross sections σ_T and σ_L and 18 matrix elements ρ^α_{ik}, $\alpha = 0..2$, $4..6$. Additional 8 matrix elements can be accessed with longitudinal beam polarization, while transverse beam polarization gives no new information.

In order to separate the contributions from ρ^0_{ik} and ρ^4_{ik} and to determine R, measurements are necessary at different values of ϵ, i.e. for different lepton scattering angles at fixed Q^2 and W^2. This is difficult as the inelastic scattering cross section decreases rapidly with increasing scattering angle. If the separation is impossible, new density matrix r^α can be introduced whose elements are the following combinations:

$$r^{04}_{ik} = \frac{\rho^0 + \epsilon R \rho^4_{ik}}{1 + \epsilon R}, \tag{2.3.15}$$

$$r^\alpha_{ik} = \begin{cases} \frac{\rho^\alpha_{ik}}{1+\epsilon R} & \alpha = 1..3, \\ \sqrt{R}\frac{\rho^\alpha_{ik}}{1+\epsilon R} & \alpha = 5..8 \end{cases} \ . \tag{2.3.16}$$

The beam polarization-independent contribution is a function of 15 independent matrix elements r^α_{ik}, the (longitudinal) polarization-dependent term contains 8 independent matrix elements.

Under the assumption of SCHC the matrix elements related to helicity-flip amplitudes vanish and only r^{04}_{00}, r^{1}_{1-1}, $Im\ r^{2}_{1-1}$, $Re\ r^{5}_{10}$, $Im\ r^{6}_{10}$, $Im\ r^{7}_{10}$ and $Re\ r^{8}_{10}$ are left. There can be no extra spin dependence at the vector-meson production vertex and the production angle Φ becomes equally distributed. The angular distribution is then a function of $cos\ \theta$ and the polarization angle $\Psi = \phi - \Phi$. A further simplification occurs in case of natural-parity exchange, where the angular distribution is fully determined by the cross section ratio R and the phase difference δ.

2.3.5 Measurements of Spin Density Matrix Elements and R

At HERMES the spin density matrix elements were determined for ρ- and ϕ-mesons [33], [34] by a fit to the angular distribution $W(\cos\theta, \phi, \Phi)$. The measurement was done with a longitudinally polarized beam, while the polarization of the proton target was disregarded. A slight violation of SCHC is observed in the ρ^0 spin density matrix element r^5_{00} that appeared to be significantly positive [33]. This observation is consistent with measurements of other experiments [35]. The matrix element r^5_{00} corresponds to the interference between the longitudinal non-flip amplitude T^0_0 and the single-flip amplitude T^0_1. This interference was predicted in Ref. [36] to be dominant in SCHC violation in at high Q^2, and also in Ref. [37] where the authors claim the applicability of their approach to real photoproduction.

The measured ρ^0-meson spin density matrix elements are consistent within large uncertainties with the assumption of natural-parity exchange.

Assuming SCHC the longitudinal-to-transverse photon cross section ratio R can be obtained from the matrix element r^{04}_{00}

$$R = \frac{1}{\epsilon}\frac{r^{04}_{00}}{1 - r^{04}_{00}} \ . \tag{2.3.17}$$

In Ref. [33] R^ρ was shown to be insensitive to slight violations of SCHC. The Q^2-dependence of R_ρ was parameterized by

$$R^\rho(Q^2) = c^\rho_0 \left(\frac{Q^2}{M^2_\rho}\right)^{c^\rho_1} \ , \tag{2.3.18}$$

$$\text{with} \quad c^\rho_0 = 0.48 \pm 0.03 \ , \quad c^\rho_1 = 0.62 \pm 0.07 \ . \tag{2.3.19}$$

The phase difference δ between the ρ^0-meson helicity amplitudes T^0_0 and T^1_1 was derived and the following values were obtained:

$$\begin{aligned} cos\ \delta &= 0.872 \pm 0.028_{stat} \pm 0.068_{syst} \\ sin\ \delta &= 0.43 \pm 0.16_{stat} \pm 0.23_{syst} \ . \end{aligned} \tag{2.3.20}$$

The spin density matrix elements of the ϕ-meson appeared to be consistent with SCHC and NPE [34]. The longitudinal-to-transverse cross section ratio R_ϕ was parameterized similarly to that of ρ^0-meson and the following values for parameters c^ϕ_0 and c^ϕ_1 for different W^2 regions

were found:

$$c_0^\phi = \begin{cases} 0.29 \pm 0.08 & W < 4 \ \text{GeV} \\ 0.42 \pm 0.05 & 4 < W < 7 \ \text{GeV} \\ 0.54 \pm 0.48 & W > 7 \ \text{GeV} \end{cases} \qquad (2.3.21)$$
$$c_1^\phi = 0.73 \pm 0.18 \ .$$

Comparison of R_ρ and R_ϕ indicates that c_0 for both mesons are consistent. In VMD this can be interpreted that the longitudinal-to-transverse scattering cross section ratios for ϕ- and ρ^0-mesons are the same. It should be taken into account, however, that the VMD predicts $c_1^{VM} = 1$ which is inconsistent with Eq. (2.3.19).

2.3.6 Polarized Lepton, Polarized Nucleon

The general case where the polarized lepton interacts with the polarized nucleon is described in detail in Ref. [32]. The main point of the discussion is the determination of natural and unnatural parity exchange contributions that would help in understanding different mechanisms of vector-meson production. Like in the unpolarized case the vector-meson spin density matrix and matrix elements are given by :

$$\rho(V) = \sum_{\alpha=0\ldots8} \sum_{\beta=0\ldots3} \Pi_\alpha \xi_\beta \rho^{\alpha\beta}, \quad \Pi_0 = \xi_0 = 1, \qquad (2.3.22)$$

$$\text{with elements} \quad \rho^{\lambda\lambda'}_{\alpha\beta} = \sum_{\lambda_{N'},\lambda_N,\lambda'_N,\lambda_\gamma,\lambda'_\gamma} e^{i\Phi(\lambda_\gamma - \lambda'_\gamma)} \cdot T^{\lambda_{N'}\lambda_V}_{\lambda_N\lambda_\gamma} \rho^{\lambda_N\lambda'_N}_\beta \rho^{\lambda_\gamma\lambda'_\gamma}_\alpha (T^{\lambda_{N'}\lambda'_V}_{\lambda'_N\lambda'_\gamma})^* \ . \qquad (2.3.23)$$

Here Π_α and ξ_β are the polarization parameters of the photon and the nucleon, respectively. The index α as before denotes the polarization state of the photon, the index β represents those of the nucleon and corresponds to the unpolarized nucleon ($\beta = 0$), transverse polarization in the hadronic plane ($\beta = 1$), transverse polarization normal to the hadronic plane ($\beta = 2$) and longitudinal polarization ($\beta = 3$).

A properly polarized target can be used for the investigation of the effects of helicity non-conserving natural and unnatural parity exchange. A transversely polarized target yields information on the unnatural parity exchange and, in conjunction with polarized leptons, it supplies additional information on natural parity exchange. The longitudinally polarized target does not give any new information on spin density matrix elements in comparison with unpolarized target. No experimental data on spin density matrix elements using both polarized beam and target exist up to now.

Chapter 3

Double-Spin Asymmetries in Photon-Nucleon Interactions

The spin dependence of polarized photon-nucleon interactions can be expressed through double-spin asymmetries in the interaction cross section. In inclusive deep inelastic scattering double-spin asymmetries are used as a tool to separate the contributions of different parton species to the nucleon spin. In exclusive vector-meson production they can help to understand the mechanism of the exchange in the t-channel of the reaction: a non-zero asymmetry in exclusive ρ^0-meson production is related to unnatural parity exchange in the t-channel which indicates the contribution from di-quark object exchange to ρ^0 production from transverse photons. This asymmetry is expected to be proportional to that in inclusive DIS scattering. The region of quasi-real photoproduction of vector mesons was investigated in order to study the dependence of the double-spin asymmetry on Q^2.

3.1 Double-Spin Asymmetries in DIS

The definition of double-spin asymmetries includes the sign and the degree of the polarization of both interacting particles. Therefore the polarization properties of photon and nucleon are inevitably involved. In the following only longitudinal polarization of beam and target will be considered, while the case of transverse target polarization will not be discussed.

3.1.1 Nucleon Structure Functions

The cross section for DIS in one-photon approximation can be expressed in terms of the leptonic and hadronic tensors $L_{\mu\nu}$ and $W_{\mu\nu}$, respectively [38]

$$\frac{d^2\sigma}{d\Omega dE'} = \frac{\alpha^2}{2MQ^4}\frac{E'}{E}L_{\mu\nu}W^{\mu\nu}. \tag{3.1.1}$$

The leptonic tensor $L_{\mu\nu}$ describes the emission of a photon by the lepton and is exactly calculable in QED, cf. discussion in section 2.2. The hadronic tensor $W_{\mu\nu}$, representing the absorption of the photon by the nucleon, can not be calculated analytically, yet.

A spin-$\frac{1}{2}$ target can be described by an axial vector $\vec{s_h}$, defined [38] additionally to the target mass M, with $|\vec{s_h}| = 0$ for the unpolarized target, $|\vec{s_h}| = M$ for a 100% polarized target and $|\vec{s_h}| = fM$ for a target with the fractional polarization f. Taking into account the parity invariance of strong interactions and the hermiticity of the electromagnetic currents, the hadronic tensor can be parameterized by experimentally accessible parameters $F_{1,2}$ and $g_{1,2}$ [38] :

$$\begin{aligned} W_{\mu\nu} =& F_1\left(-g_{\mu\nu} + \frac{q_\mu q_\nu}{q^2}\right) + \frac{F_2}{p\cdot q}\left(p_\mu - \frac{(p\cdot q)q_\mu}{q^2}\right)\left(p_\nu - \frac{(p\cdot q)q_\nu}{q^2}\right) \\ &+ \frac{ig_1}{p\cdot q}\epsilon_{\mu\nu\lambda\sigma}q^\lambda s^\sigma + \frac{ig_2}{(p\cdot q)^2}\epsilon_{\mu\nu\lambda\sigma}q^\lambda(p\cdot q s^\sigma - s\cdot q p^\sigma)\ . \end{aligned} \tag{3.1.2}$$

Here q_μ and p_μ are the four-momenta of the photon and the nucleon, respectively. The notations $g_{\mu\nu}$ and $\epsilon_{\mu\nu\lambda\sigma}$ stand for the metric and Levi-Cevita tensors, respectively.

The parameters F_1, F_2, g_1 and g_2 describe the structure of the nucleon and are therefore called structure functions. They are dimensionless functions of the Lorentz invariant variables $p^2 = M^2$, $p\cdot q$ and q^2. Nowadays they are written as functions of the variables x and Q^2. In the quark-parton model (QPM), where the constituents of the hadron are considered as free point-like objects, the scaling variable x is interpreted as the momentum fraction of the nucleon carried by the struck quark. In this approximation the structure functions are predicted to depend only on x and be independent on Q^2 (Bjorken scaling). As $1/Q^2$ defines the resolution of the scattering, the independence on Q^2 can be interpreted in a way that the structure of components is much smaller than the resolution of the process. Perturbative QCD allows to calculate the evolution of the structure functions with Q^2 (scaling violation) at high energies using the Gribov-Lipatov-Altarelli-Parisi (DGLAP) equations [39, 40] at a certain Q^2, starting from a fixed Q_0^2. The structure functions F_1 and F_2 do not depend on the nucleon polarization while g_1 and g_2 do.

Similarly to the case of vector-meson production, discussed in section 2.3, the hadronic vertex of deep inelastic photon-nucleon scattering and, in turn, the structure functions can be represented in terms of helicity amplitudes of forward Compton scattering $A^{\lambda_{N'}\lambda_{\gamma'}}_{\lambda_N\lambda_\gamma}$. Here $\lambda_{N(N')}$ and $\lambda_{\gamma(\gamma')}$ denote the helicities of initial (final) nucleon and photon state, respectively. The structure functions are related to the following helicity amplitudes [38]:

$$2\pi F_1 = \frac{1}{2}\ Im\ (A^{++}_{++} + A^{-+}_{-+}), \tag{3.1.3}$$

$$2xF_1 - F_2 \propto Im\ (A^{+0}_{+0}) = Im\ (A^{-0}_{-0}), \tag{3.1.4}$$

$$2\pi g_1 = \frac{1}{2}\ Im\ (A^{-+}_{-+} - A^{++}_{++})\ . \tag{3.1.5}$$

The expressions (3.1.3) and (3.1.4) are related to the cross sections for scattering a transverse and a longitudinal photon off an unpolarized target, respectively. Expression (3.1.5) is a spin asymmetry in the scattering cross section for a transverse photon. The combination $g_1 + g_2$ is proportional to the helicity-single-flip amplitude A^{+0}_{-+}.

The hadronic tensor can be expressed in terms of parton distribution functions of quarks of flavor f with spin parallel (q_f^+) and antiparallel (q_f^-) to that of the nucleon. The calculation

of the hadronic tensor in the QPM yields the following expressions for the structure functions in terms of parton distributions:

$$F_1(x,Q^2) = \frac{1}{2}\sum_f e_f^2(q_f^+(x,Q^2) + q_f^-(x,Q^2)) = \sum_f e_f^2 q_f \ , \tag{3.1.6}$$

$$F_2(x,Q^2) = \sum_f e_f^2 x(q_f^+(x,Q^2) + q_f^-(x,Q^2)) = \sum_f e_f^2 x q_f \ , \tag{3.1.7}$$

$$g_1(x,Q^2) = \frac{1}{2}\sum_f e_f^2(q_f^+(x,Q^2) - q_f^-(x,Q^2)) = \sum_f e_f^2 \Delta q_f, \tag{3.1.8}$$

where q_f and Δq_f represent the unpolarized and polarized quark distributions, respectively. From Eqs. (3.1.6) and (3.1.7) follows the Callan-Gross relation $2xF_1(x) = F_2(x)$. In the framework of the naive QPM, where masses and transverse momenta of the quarks are neglected, the polarized structure function g_2 is equal to zero.

In the QPM, the helicity of the nucleon is given by the helicities of valence and sea quarks:

$$\frac{1}{2} = \frac{1}{2}\,\Delta\Sigma = \frac{1}{2}\sum (\Delta q_v + 2\Delta\bar{q}) \ . \tag{3.1.9}$$

The relativistic QPM predicts $\Delta\Sigma \approx 0.6$. Measurements of g_1, however, give the value $\Delta\Sigma \approx 0.2 - 0.3$ [41, 42] which is only about half of the expectation, and hence suggest the existence of some other contributions to the nucleon spin. In the QCD-inspired parton model the helicity of the nucleon is written as a sum of contributions from quark and gluon spin and orbital angular momenta [43]:

$$\frac{1}{2} = \frac{1}{2}\,\Delta\Sigma + \Delta G + L_q + L_g \ . \tag{3.1.10}$$

Here ΔG denotes the gluon contribution and L_q and L_g represent the angular momentum carried by quarks and gluons, respectively. The properties and experimental accessibility of each contribution are discussed in Ref. [44].

3.1.2 Formalism of Double-Spin Asymmetries in DIS

The polarized structure functions g_1 and g_2 can be determined by measuring double-spin asymmetries in the photon-nucleon cross section when both lepton[1] and nucleon are longitudinally polarized. The photon-nucleon interaction is schematically shown in fig. 3.1.1. Since the struck quark in the final state must have spin $\frac{1}{2}$, the photon can be absorbed only by a quark whose helicity is antiparallel to the helicity of the photon. The amount of such quarks within the nucleon depends on the polarization state of the nucleon. The helicity of the photon-nucleon system can be either 1/2 or 3/2, with the corresponding photon-nucleon cross section denoted by $\sigma_{1/2}$ and $\sigma_{3/2}$, respectively.

[1]The longitudinally polarized lepton beam produces a flux of virtual photons, in which at small virtualities $Q^2 \simeq 0$ transverse photons dominate. With growing Q^2 the fraction of longitudinal photons increases.

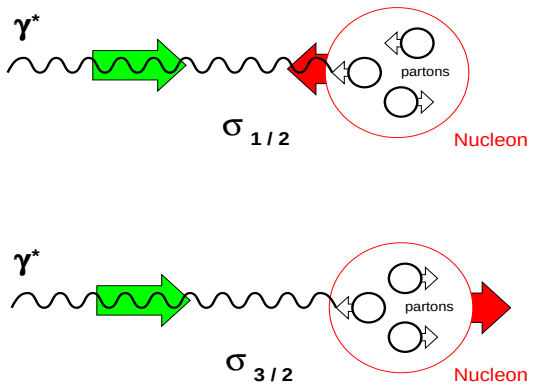

Figure 3.1.1: QPM representation of a transverse photon interacting with quarks inside a nucleon.

Two asymmetries A_1 and A_2 are used to describe the spin dependence of the photon-nucleon interaction. The asymmetry A_1 for a transverse photon interacting with a longitudinally polarized nucleon is defined as

$$A_1 = \frac{\sigma_{1/2} - \sigma_{3/2}}{\sigma_{1/2} + \sigma_{3/2}} \ . \tag{3.1.11}$$

The asymmetry A_2 arises from the interference between transverse and longitudinal photons:

$$A_2 = \frac{\sigma_{LT}}{\sigma_{1/2} + \sigma_{3/2}} = \frac{\sigma_{LT}}{\sigma_T} \ , \tag{3.1.12}$$

where σ_{LT} is the cross section describing the interference between longitudinal and transverse photons. Recalling the connection of the structure functions to the helicity amplitudes of forward Compton scattering (Eq. 3.1.3 - 3.1.5) the following relations between the structure functions and photon absorption cross section can be derived [38]:

$$\begin{aligned} \sigma_{3/2} &\sim (F_1 + g_1 - \gamma^2 g_2) \ , \\ \sigma_{1/2} &\sim (F_1 - g_1 + \gamma^2 g_2) \ , \\ \sigma_{1/2}^{LT} &\sim g_1 + g_2 \ . \end{aligned} \tag{3.1.13}$$

Here $\gamma = 2Mx/Q$ is a dimensionless kinematic factor. The asymmetries then read:

$$A_1 = \frac{g_1 - \gamma g_2}{F_1} \ , \quad A_2 = \gamma \ \frac{g_1 + g_2}{F_1} \ . \tag{3.1.14}$$

The photon absorption asymmetry A_1 is experimentally accessible through a measurement of the lepton-nucleon asymmetry $A_{||}$ using longitudinally polarized beam and target. This experimental asymmetry is defined in terms of $\sigma^{\vec{\Rightarrow}}$ and $\sigma^{\vec{\Leftarrow}}$, the cross sections for parallel and antiparallel orientation of the nucleon helicity with respect to the lepton helicity:

$$A_{||} \equiv \frac{\sigma^{\vec{\Leftarrow}} - \sigma^{\vec{\Rightarrow}}}{\sigma^{\vec{\Leftarrow}} + \sigma^{\vec{\Rightarrow}}} = \frac{N^{\vec{\Leftarrow}} L^{\vec{\Rightarrow}} - N^{\vec{\Rightarrow}} L^{\vec{\Leftarrow}}}{N^{\vec{\Leftarrow}} L_p^{\vec{\Rightarrow}} + N^{\vec{\Rightarrow}} L_p^{\vec{\Leftarrow}}} \ . \tag{3.1.15}$$

It is determined from the number of events $N^{\overrightarrow{\Rightarrow}(\overrightarrow{\Leftarrow})}$ for the corresponding beam and target helicity configuration, weighted by the relative luminosities $L^{\overrightarrow{\Rightarrow}(\overrightarrow{\Leftarrow})}$. Relative luminosities weighted with polarizations of beam, p_b, and target, p_T, are denoted by $L_p = L \cdot p_b \cdot p_T$ and are calculated per helicity configuration, as well. The photon absorption asymmetries are connected to the lepton-nucleon asymmetry via the effective photon polarization D and the flux ratio ϵ (cf. Eqs. 1.1.13, 1.1.14) :

$$A_1 = \frac{A_{||}}{D} - \eta A_2 \ , \tag{3.1.16}$$
$$\text{with} \quad \eta = 2\,\epsilon\,\frac{\sqrt{Q^2}}{(M+2E)(1-(1-\epsilon))} \ .$$

A direct measurement of A_2 requires a transversely polarized target, which was not used at HERMES before 2002. However, the maximum value of A_2 is given by its positivity limit, derived from the interference term $\sigma_{LT} \leq \sqrt{\sigma_L \sigma_T}$:

$$A_2 \leq \sqrt{\frac{\sigma_L \sigma_T}{\sigma_T^2}} = \sqrt{R} \ . \tag{3.1.17}$$

In the following the notations A_1^N and A_2^N will be used for the double-spin asymmetries A_1 and A_2 in inclusive DIS.

3.2 Spin Asymmetry in Vector-Meson Production

The above outlined formalism of double-spin asymmetries can be applied to vector-meson production. From now on only longitudinal polarization of beam and target is considered. The double-spin asymmetry in the cross section of vector-meson production in lepton-nucleon interactions is defined as

$$A_{||}^{VM} \equiv \frac{\sigma^{\overrightarrow{\Leftarrow}} - \sigma^{\overrightarrow{\Rightarrow}}}{\sigma^{\overrightarrow{\Leftarrow}} + \sigma^{\overrightarrow{\Rightarrow}}} = \frac{N_{VM}^{\overrightarrow{\Leftarrow}} L^{\overrightarrow{\Rightarrow}} - N_{VM}^{\overrightarrow{\Rightarrow}} L^{\overrightarrow{\Leftarrow}}}{N_{VM}^{\overrightarrow{\Leftarrow}} L_p^{\overrightarrow{\Rightarrow}} + N_{VM}^{\overrightarrow{\Rightarrow}} L_p^{\overrightarrow{\Leftarrow}}} \ . \tag{3.2.1}$$

Here in analogy to Eq. (3.1.15) $N_{VM}^{\overrightarrow{\Rightarrow}(\overrightarrow{\Leftarrow})}$ denotes the number of produced vector mesons for the corresponding beam and target helicity configuration. This asymmetry is connected to the photon absorption asymmetry A_1^{VM} :

$$A_1^{VM} = \frac{A_{||}^{VM}}{D^{VM}} - \eta A_2^{VM} \ , \tag{3.2.2}$$

The contribution from A_2^{VM}, similarly to Eq.(3.1.17), is limited by the condition:

$$A_2^{VM} = \sqrt{\frac{\sigma_{LT}^{VM}}{\sigma_T^2}} \leq \sqrt{\frac{\sigma_L^{VM} \sigma_T^{VM}}{\sigma_T^2}} = \sqrt{R^{VM}} \ . \tag{3.2.3}$$

In the following the contribution from A_2^{VM} is replaced by its positivity limit, which is based upon the relation (2.3.12), as the phase difference between the helicity conserving

longitudinal and transverse amplitudes in ρ^0-meson production was measured to be small [45].

The double-spin asymmetry A_1^ρ in ρ^0 electroproduction on a proton target was measured at HERMES [46] for the first time and appeared to be significantly different from zero.

3.2.1 Asymmetry in Exclusive ρ^0-meson Electroproduction.

For the first time an estimate of the double-spin asymmetry A_1^ρ in (forward) diffractive ρ^0-meson electroproduction was given in Ref. [47], where it was related to the double-spin asymmetry in inclusive deep inelastic scattering, A_1^N, introduced in section 3.1.2. The notations throughout this section follow those of Ref. [47]. The double-spin asymmetry in the cross section of ρ^0-meson production in scattering of both longitudinally polarized lepton and nucleon reads (cf. Eq. 3.1.11)

$$A_1^\rho = \frac{\sigma(\xi_e, +\xi_{||}) - \sigma(\xi_e, -\xi_{||})}{\sigma(\xi_e, +\xi_{||}) + \sigma(\xi_e, -\xi_{||})} = \xi_e \xi_{||} \frac{\sigma(\xi_e, \xi_{||})}{\sigma(0,0)} \ , \tag{3.2.4}$$

where ξ_e and $\xi_{||}$ denote the polarization of the lepton and the longitudinal polarization of the nucleon, respectively. The differential cross section of ρ^0-meson production is given by $\sigma(\xi_e, \xi_{||})$, the cross-section for the unpolarized case is denoted by $\sigma(0,0)$.

The differential cross section can be expressed in terms of the ρ^0-meson spin density matrix $\rho(\rho^0)$ with its elements connected to the helicity amplitudes $T^{\lambda_{N'}\lambda_V}_{\lambda_N\lambda_\gamma}$ via the relations (2.3.23). Taking into account angular momentum conservation the helicity amplitudes can be represented as

$$T^{\lambda_{N'}\lambda_V}_{\lambda_N\lambda_\gamma}(Q^2, \nu, t) \propto sin\left(\frac{1}{2}\,\theta_V^*\right)^{|\lambda_{N'} - \lambda_N| - |\lambda_V - \lambda_\gamma|} \ , \tag{3.2.5}$$

where θ_V^* is the vector-meson production angle (cf. Eq. (2.1.4)). In case of forward production ($\theta_V^* = 0$, $t \sim 0$) the number of independent helicity amplitudes is reduced to three helicity-conserving amplitudes T^{++}_{++}, T^{+-}_{+-}, T^{+0}_{+0} and two helicity-flip amplitudes T^{++}_{-0} and T^{+0}_{--}. These amplitudes can be split up into natural- ($n^{i'j'}_{ij}$) and unnatural- ($u^{i'j'}_{ij}$) parity components. The longitudinal amplitude has only a natural-parity component, while the natural- and unnatural-parity contributions of the helicity-flip amplitudes T^{++}_{-0} and T^{+0}_{--} coincide:

$$\begin{aligned}
&T^{+\pm}_{+\pm} = n^{++}_{++} \pm u^{++}_{++} \ , \\
&T^{+0}_{+0} = n^{+0}_{+0} \ , \\
&T^{++}_{-0} = 2n^{++}_{-0} = 2u^{++}_{-0} \ , \\
&T^{+0}_{--} = 2n^{+0}_{--} = 2u^{+0}_{--} \ .
\end{aligned}$$

Since for diffractive production of vector mesons the helicity is approximately conserved in the s-channel, all terms bilinear in helicity-flip amplitudes are neglected. All imaginary parts of bilinears of helicity amplitudes are neglected, as well. The differential cross section for a longitudinally polarized nucleon is then obtained in the form:

$$\sigma \propto |n^{++}_{++}|^2 + \epsilon\ |n^{+0}_{+0}|^2 + 2\sqrt{1-\epsilon^2}\ \xi_e \xi_{||}\ Re\ (n^{++}_{++} u^{++*}_{++}) \ , \tag{3.2.6}$$

where the term $(n^{++}_{++}u^{++*}_{++})$ represents the interference between the natural- and unnatural-parity parts of the transverse amplitudes. The asymmetry 3.2.4 then reads:

$$A_1^\rho(\xi_e, \pm\xi_{||}) = \xi_e^2\xi_{||}^2 \; \frac{2\sqrt{1-\epsilon^2}\; Re\; (n^{++}_{++}u^{++*}_{++})}{|n^{++}_{++}|^2 + \epsilon\; |n^{+0}_{+0}|^2} \; . \tag{3.2.7}$$

Thus it can be concluded that the double-spin asymmetry (3.2.4) is introduced by the interference between the natural- and unnatural-parity parts of the transverse SCHC amplitudes. As has been discussed in section 1.6, exclusive diffractive scattering of the vector meson off the nucleon can be described by the exchange of an intermediate object in the t-channel. A non-zero double-spin asymmetry in such a process indicates the presence of both unnatural- and natural-parity contributions in this exchange. Note that even a tiny contribution of the unnatural parity part can yield an asymmetry, while remaining negligible in the incoherent sum of squared amplitudes in the total cross section. For the following calculations the expression (3.2.7) is re-written in the form

$$A_1^\rho(\xi_e, \pm\xi_{||}) = \xi_e\xi_{||}\frac{2\;\sqrt{1-\epsilon^2}}{1+\epsilon\; cos\; (2\Psi)}\; \frac{Im\; u^{++}_{++}}{Im\; n^{++}_{++}} \; , \tag{3.2.8}$$

where Ψ stands for the polarization angle, defined in section 2.3.4. The real parts of the diffractive amplitudes are expected to be small [48, 49] and have therefore been neglected.

The helicity amplitudes for both ρ^0-meson production and forward Compton scattering, the latter connected to the DIS cross-section via the optical theorem, were calculated in the framework of the off-diagonal GVMD [47]. The ratio of the helicity amplitudes for elastic scattering and dissociative diffraction is taken to be the same for all helicities. The asymmetry (3.2.4) is then calculated in terms of the asymmetries A_1^N and A_2^N, as used in the inclusive DIS process at high[2] Q^2:

$$A_1^\rho(\xi_e, \pm\xi_{||}) \sim a\frac{\xi_e\xi_{||}}{1+\epsilon\; cos\; 2\; \Psi}\left(A_1^N - \frac{A_2^N}{(1+E_b/xM)tg\frac{1}{2}\theta_e}\right), \tag{3.2.9}$$

$$\text{with}\;\; a = 2(1+\epsilon R)\sqrt{\frac{1+\epsilon}{1-\epsilon}}\; \frac{1+Mx/E_b}{2E_b/\nu - 1}, \tag{3.2.10}$$

where θ_e is the lepton scattering angle. The contribution of the asymmetry A_2^N was calculated to be negligible. Hence it was concluded that the asymmetry (3.2.8) in ρ^0 production at high beam energies E_b is essentially defined by the asymmetry $A_{||}$. The factor a gives an enhancement of the asymmetry in ρ^0-meson production in comparison to that in inclusive DIS.

In Ref. [47] numerical calculations of the ratio of photon absorption asymmetries A_1^ρ/A_1^p are performed for finite values of Q^2 and $x < 0.2$, for two electron energies E_b=15 GeV and E_b=50 GeV, and for electron scattering angles $\theta = 10^o,\; 20^o,\; 30^o$. From these predictions a value of about 2 was interpolated for the HERMES beam energy [46].

[2]For finite Q^2 this expression has to be modified by a factor which is a function of Q^2. This factor is taken into account in numerical calculations of Ref. [47].

The approach of Ref. [47] to calculate the ratio A_1^ρ/A_1^p is simplified in Ref. [46]. The asymmetries for ρ^0-meson production and inclusive DIS scattering are written in terms of transverse (only) s-channel helicity-conserving amplitudes as

$$A_1^\rho = \frac{|T_{++}^{++}|^2 - |T_{+-}^{+-}|^2}{|T_{++}^{++}|^2 + |T_{+-}^{+-}|^2}, \quad A_1^p = \frac{Im\ T_{++}^{++} - Im\ T_{+-}^{+-}}{Im\ T_{++}^{++} + Im\ T_{+-}^{+-}}\ . \tag{3.2.11}$$

Here the terms $Im\, T_{++}^{++}$ and $Im\, T_{+-}^{+-}$ correspond to the cross sections $\sigma_{1/2}$ and $\sigma_{3/2}$, connected to the imaginary part of the forward Compton scattering amplitudes via the optical theorem. The amplitudes for ρ^0 production and the $\gamma^* p \to \gamma^* p$ process are assumed to differ only by a common factor. In contrast to Ref. [47], all helicity-flip amplitudes are neglected. The real parts of the amplitudes T_{++}^{++} and T_{+-}^{+-} are assumed to be negligible, as well as in Ref. [47]. The ratio A_1^ρ/A_1^p was approximated by:

$$\frac{A_1^\rho}{A_1^p} \propto \frac{2}{1 + (A_1^p)^2}\ . \tag{3.2.12}$$

The inclusive DIS asymmetry, as measured at HERMES on a proton target, has a value of $A_1^p = 0.13$ at $x = 0.07$ [50]. This results in a ratio of double-spin asymmetries (3.2.12) of about 2, which is consistent with the above quoted prediction of Ref. [47].

3.2.2 Calculation in the Framework of Regge Model

As discussed above, a non-zero double-spin asymmetry in vector-meson production is induced by an interference between exchanges with natural and unnatural parities. A possible interpretation of the double-spin asymmetry in vector-meson production measured at HERMES is given in Ref. [51]. In the framework of Regge theory vector-meson electroproduction at intermediate energies is thought to proceed via natural parity (Pomeron, σ and f_2) exchanges, and unnatural parity (pion) exchange (citations within Ref. [51]). Natural-parity exchange is predicted to dominate. The calculation [51] shows that in general it is impossible to describe the measured double-spin asymmetry [46] by the interference of pion exchange with any natural-parity exchanges. Instead, the contribution of the exchange of the f_1 trajectory, introduced in Ref. [52, 53], to vector-meson production is considered.

The anomalous trajectory f_1 with unnatural parity has a very high intercept $\alpha_0 \approx 1$, a small slope $\alpha' \approx 0$ and possesses the quantum numbers $I^G(J^{PC}) = 0^+(1^{++})$. The notation f_1 stands for the dominant contribution of the axial vector meson $f_1(1285)$ [52]. Although the f_1 trajectory was suggested to explain the behavior of elastic hadron-hadron scattering as well as of light vector-meson photoproduction at high energies and momentum transfers, intermediate energies and small momenta transfers can also be considered [51, 54].

In Ref. [51] the mechanism of vector-meson production is related to t-channel Pomeron and f_1 exchange with weak energy dependence and secondary exchange of Reggeons (π, σ, f_2) with strong energy dependence. The Pomeron trajectory is parameterized, like in Ref. [18], by $\alpha_P(t) = 1.08 + 0.25t$. The parameters of the secondary Regge exchanges were obtained from fits to data on hadron-hadron scattering. The mesonic Regge trajectory is given by $\alpha_{\pi,\sigma}(t) = \alpha'(t - m^2_{\pi,\sigma})$ with the slope $\alpha' \approx 0.9$ GeV^{-2}. The calculated amplitude

of f_1 exchange has only a real part, therefore its interference with the nearly imaginary Pomeron amplitude is very small. In contrast, the f_2 amplitude contains a significant real part. Therefore it is concluded that the main contribution to the double-spin asymmetry comes from the interference between f_2 and f_1 exchanges.

Within the model [51] all amplitudes have the same Q^2 dependence, therefore the double-spin asymmetry is predicted to be independent on Q^2. The $|t|$-dependence of the double-spin asymmetry can be determined from that of the electromagnetic form-factors of the f_1-nucleon and Pomeron-nucleon vertices [52]:

$$F_{(f_1NN)} = \frac{1}{(1-t/m_{f_1}^2)^2} \ , \quad F_{(\mathbf{P}NN)} = \frac{4m_p^2 - 2.8t}{(4m_p^2 - t)(1-t/0.71)^2} \ , \tag{3.2.13}$$

where m_p is the proton mass. The axial vector form factor $F_{(f_1NN)}$ decreases slower with $|t|$ than the isoscalar form factor $F_{(\mathbf{P}NN)}$, therefore the f_1 contribution dominates over the Pomeron one at high $|t|$. At lower $|t| < 1$ GeV, however, the f_1 contribution increases with $|t|$ and one can expect the asymmetry increasing with $|t|$ as well.

The value predicted for the double-spin asymmetry in exclusive ρ^0-meson production at HERMES energies is $A_1^\rho \approx$ 10-15%. In contrast to the case of the ρ^0-meson, for ϕ- and J/ψ-mesons the main contribution to the double-spin asymmetry should be given by the interference between the f_1 and the Pomeron trajectory, as f_2 couplings vanish for these mesons [51]. Small and negative double-spin asymmetries for both ϕ- and J/ψ-mesons are expected.

The double-spin asymmetries for ρ- and ϕ-production from real photons at W = 100 GeV were discussed in Ref. [52]. The asymmetries averaged over $|t|$ in the region $|t| < 0.6$ GeV^2 are compatible with zero.

3.2.3 pQCD Calculation based upon Hadron-Parton Duality

In Ref. [55] the double-spin asymmetry in diffractive ρ^0-production on a polarized proton target was calculated in pQCD under the assumption of hadron-parton duality. In this framework it is predicted that A_1^ρ is related to the gluon distribution function $G(x)$. The hadron-parton duality hypothesis, described in detail in Ref. [56], implies the replacement of the total hadron production cross section averaged over a squared-mass interval, ΔM^2, (typically 1 GeV^2) by the partonic cross section:

$$\left\langle \sum_n \sigma(\gamma^* \to h = \rho, \omega, ...) \right\rangle_{\Delta M^2} \approx \left\langle \sum_n \sigma(\gamma^* \to q\bar{q}) \right\rangle_{\Delta M^2} . \tag{3.2.14}$$

The hadron-parton duality is applied to exclusive diffractive ρ^0-electroproduction for a $q\bar{q}$-state produced in the invariant mass interval containing the ρ^0-meson. Electroproduction of the ρ^0-meson is claimed to proceed via "open" $u\bar{u}$, $d\bar{d}$ production. This $q\bar{q}$-pair interacts with the proton without forming a vector-meson state. Only after the interaction with the proton, confinement distorts the $q\bar{q}$-state and forces it to form a ρ-meson. It was demonstrated that diffractive ρ-meson electroproduction on an unpolarized target can be well reproduced by

calculations in the framework of pQCD based on hadron-parton duality[3]. The calculation was performed for both the longitudinal and the transverse cross section of ρ-meson production. The model prediction for the Q^2-dependence of the ratio σ_L/σ_T is compared with HERA data in [56]. At high energies the amplitude of diffractive ρ^0-meson electroproduction on an unpolarized nucleon was calculated to be proportional to the gluon density $G(x)$.

For the polarized nucleon the amplitudes of the process were calculated in Ref. [55]. After the $\gamma \to q\bar{q}$ transition quark and gluon exchange are considered to contribute to the process of the interaction between the "open" $q\bar{q}$-pair and the nucleon. Both types of processes are schematically shown in fig. 3.2.1. The amplitude of the quark exchange process a)

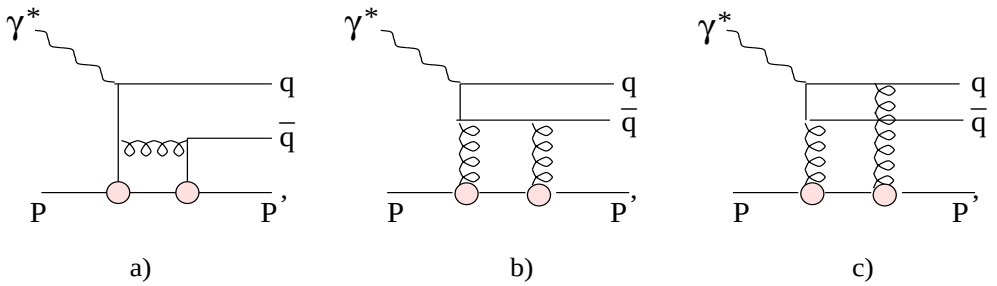

Figure 3.2.1: Schematic representation of a) quark- and b), c) gluon-exchange contributions to diffractive vector-meson production in the framework of the parton-hadron duality hypothesis.

conserves the helicity of the initial quark line in forward direction. The Born amplitude of the diffractive reaction $\gamma^* + q \to (q\bar{q} + q)$ is described by the sum of the diagrams b) and c). At least one gluon has to be transversely polarized, as a longitudinally polarized gluon does not carry any information about the target polarization [55]. The forward amplitude of diffractive "open" quark pair production on a polarized nucleon was calculated in Ref. [55]. The double-spin asymmetry in diffractive ρ-meson production was related to the unpolarized and polarized quark and gluon distribution based on the assumption of u-quark dominance. In the HERMES kinematics region ($Q^2 \leq 3.5$ GeV^2) and at medium x the asymmetry was obtained as an approximation

$$A^{\gamma^* p \to \rho p} \approx -\frac{\Delta G(x, \bar{Q}^2)}{2G(x, \bar{Q}^2)} \ . \tag{3.2.15}$$

Here the notation $\bar{Q}^2 = z(1-z)Q^2$ is used with z being the photon momentum fraction carried by the quark.

3.2.4 Asymmetry in Quasi-Real Photoproduction of Vector Mesons

A possible "direct" way to tag the gluon contribution to the nucleon spin is to measure spin asymmetries in the production of high-p_t jets from the photon-gluon fusion process [58]. At HERMES energies jet detection is not possible, so high-p_t hadrons can be taken as substitutes for jets [59]. However, semi-inclusive measurements are difficult due to marginal statistics.

[3]Once the hard scale is provided, by $Q^2 + M^2 > 5$ GeV^2[57].

Instead quasi-real photoproduction of high-p_t hadrons can be used [60]. Several different processes (PGF, VMD, QCDC and DIS) contribute to the total cross section of the photon-proton interaction at low Q^2 (cf. Eq. 1.3.7). Therefore the contributions of all subprocess asymmetries to the high-p_t asymmetry have to be estimated. Due to the relatively low energy of HERMES the PGF process is suppressed. The double-spin asymmetry for quasi-real photoproduction of vector mesons, i.e. the VMD contribution, was not measured up to now. The first measured double-spin asymmetry in quasi-real photoproduction of ρ^0- and ϕ-mesons will be discussed in section 5.4.

Chapter 4

The HERMES Experiment

The HERMES experiment was designed to determine the spin structure functions of proton and neutron by precision measurements of inclusive and semi-inclusive spin asymmetries in polarized DIS. It uses the longitudinally polarized electron beam of the HERA storage ring at DESY (Hamburg, Germany) and an internal target filled with polarized or unpolarized gas.

4.1 Polarized Electron Beam of HERA

The HERA storage ring facility consists of two separate accelerators. The proton ring was built for an energy of 820 GeV before and of 920 GeV after the accelerator upgrade in 1998. In the lepton ring polarized positrons (or electrons) of 27.5 GeV circulate in the opposite direction. Fig. 4.1.1 shows HERA with its four experiments. The experiments H1 and ZEUS analyze proton-electron collisions, HERA-B is a fixed target experiment and uses the proton beam. HERMES uses the lepton beam and an internal gas target. HERA can store electrons as well as positrons. For the H1 and ZEUS experiments the lepton charge does make a difference, as the cross section of weak interaction depends on it. For HERMES, in contrast, the lepton charge makes mostly[1] no difference, as the electromagnetic cross sections in both cases are identical. Until 1998 HERA was operated with positrons, that appeared to make a longer beam life-times possible. One possible explanation for a reduced lifetime of the electron beam could be capture of ionized dust particles. After the vacuum system upgrade in 1998 the electron beam was used, as well.

The electrons in the lepton ring are stored in 189 bunches with 96 ns separation in between. HERA runs 174 colliding and 15 so-called pilot bunches, used for background studies. Circulating in the beamline, the lepton beam gets self-polarized transverse to its direction of motion (Sokolov-Ternov effect, [62]). Passing the bending magnets in the accelerator, electrons (positrons) emit synchrotron radiation. A tiny asymmetry in the spin-flip amplitude of synchrotron radiation slightly enhances the polarization state where the spin of the electron (positron) is anti-parallel (parallel) to the magnetic field of the bending magnets. For

[1] For studies of the DVCS process, however, the charge of the lepton beam is important [61].

initially unpolarized electrons in uniform circular motion the beam transverse polarization rises exponentially with time

$$P(t) = P_\infty \cdot (1 - e^{-t/\tau}) \; . \tag{4.1.1}$$

Here P_∞ stands for the asymptotic degree of polarization. The characteristic polarization rise time is denoted by τ, it depends on the beam energy and the accelerator radius. For an accelerator with energy 27.5 GeV and bending radius of 707 m with homogeneous magnetic field these values are $p_\infty = \frac{8}{5\sqrt{3}} \approx 92.4\%$, $\tau = 37$ min. In a real machine depolarizing effects exist, like small misalignments of the magnets in the ring, beam-beam interactions between the lepton and proton beams in the interaction zones, spin diffusion and depolarizing resonances. They reduce with the self-polarization by the Sokolov-Ternov effect and hence decrease the maximum reachable polarization at HERA to a value about 70% with a rise time of about 20 min. The average beam polarization achieved at HERA is about 55%.

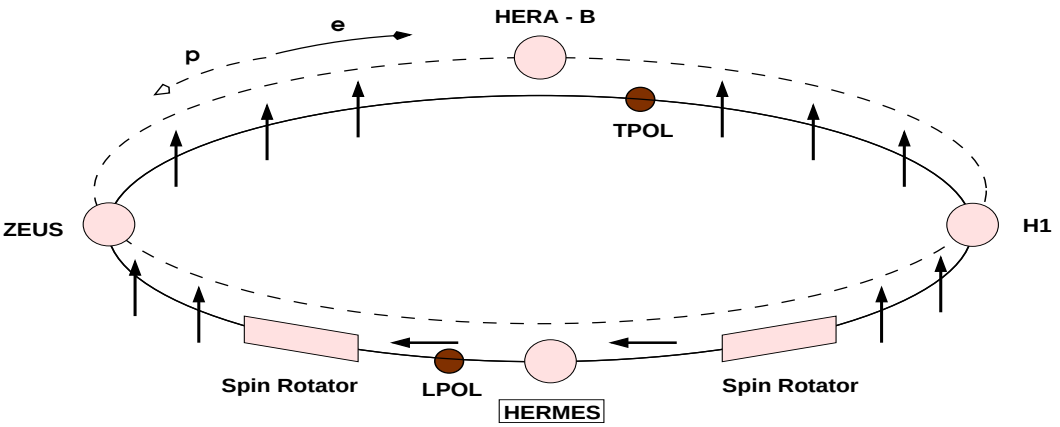

Figure 4.1.1: Sketch of the HERA storage ring with its four experiments.

To obtain longitudinal polarization of the beam two spin rotators are installed enclosing the HERMES interaction region, as shown in fig. 4.1.1. They consist of interleaved horizontal and vertical dipole magnets [63] which by means of succession of rotations cause the direction of the spin to be longitudinal without affecting the position and slope of the beam. The spin rotator upstream of the experiment rotates the transverse polarization of the beam into a longitudinal one. The spin rotator downstream of the experiment rotates the longitudinal polarization back into a transverse one, ensuring that the electrons remain polarized throughout the storage ring. The helicity of the longitudinally polarized beam can be made positive or negative. Reversal of the beam helicity requires a mechanical shift of the rotator magnets and can be only performed during a shutdown of the accelerator.

The polarization of the beam is measured independently by two Compton polarimeters, also indicated in fig. 4.1.1. Since no loss of polarization is expected due to spin rotators, the degree of transverse polarization in the ring is equal to that of the longitudinal polarization in the region of the HERMES experiment. The transverse polarimeter (TPOL) [64] uses the spin dependence of the Compton cross section: left- and right-circularly polarized laser light is scattered off the electron beam. The backscattered photons are detected in a position

sensitive calorimeter. The intensity of the backscattered photons is distributed asymmetrically with respect to the azimuthal scattering angle. The magnitude of the asymmetry is proportional to the transverse polarization of the beam. The laser intensity is chosen so that the probability of multiple Compton photons per bunch crossing is small and the position and the energy of single photons is used for the analysis ('single-photon' method).

The longitudinal beam polarization is measured with the longitudinal polarimeter (LPOL) [65], positioned close to the HERMES experimental area. It was designed to obtain an independent, more precise measurement of the beam polarization and has the capability to measure individual bunch polarizations. Like the transverse polarimeter, the longitudinal polarimeter makes use of asymmetries in the Compton scattering of a circularly polarized laser beam off the polarized electron beam. The longitudinal electron polarization produces an asymmetry in the energy spectrum of the backscattered Compton photons. The intensity of the laser beam is such that several thousands photons are scattered per electron bunch and detected by a calorimeter. The beam polarization is determined from the asymmetry of the energy deposition for left- and right-polarization states of the laser light.

4.2 Internal Gas Target

HERMES uses a gas target internal to the lepton beam, that can be operated with different polarized and unpolarized gases. The polarized target system [66, 67] consists of a source of polarized atoms, a magnetic holding field, a storage cell, and a polarimeter which measures the target polarization. In the following the polarized hydrogen/deuterium target is briefly described.

The atomic beam source (ABS) is used as a source of polarized hydrogen and deuterium atoms. Its operational principle is based on the Stern-Gerlach separation of atomic hydrogen or deuterium. Molecular gas is dissociated by 13.56 MHz radio frequency discharge into atoms. The atomic beam is fed through a system of sextupole magnets. Depending on the state of the electron spin of the atom the particle beam is focused or defocused. The electron spin is transfered into the nuclear spin by an adiabatic high-frequency transition unit. The spin quantization axis is determined by a magnetic holding field of 0.35 T, which is applied along the whole target cell. In 1996-2000 a longitudinally polarized target was used. The sign of the polarization was regularly flipped every 90 seconds by a change of the radio frequency.

The polarized atomic beam is injected into a thin T-shaped tube ("storage cell"), as shown schematically in fig. 4.2.1. The stored lepton beam passes parallel through the center of the tube without any interaction with walls or windows. A set of upstream collimators protects the storage cell from synchrotron radiation and secondary particle showers. Scattered particles emerge into the spectrometer acceptance through a stainless steel exit window.

The storage cell is made out of 70 μm thin aluminum foil. It has an elliptic form of 30 $\times$ 10 mm and is 400 mm long. The cell is mounted on aluminum rails. In order to reduce the velocity of the atoms and thereby increase the density of the target the storage cell is cryogenically cooled. The target density at an operating temperature of 100 K is about $8 \cdot 10^{13}$ atoms/cm^2. Performing wall collisions the atoms diffuse into the vacuum of

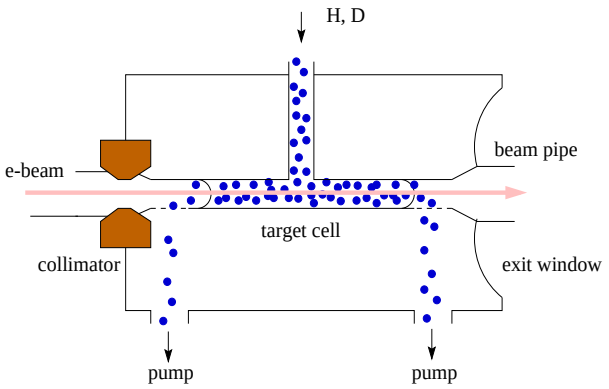

Figure 4.2.1: Schematic view of the HERMES target region.

the HERA beam line, where they are pumped away by a high-speed differential pumping system, providing ultra-high vacuum in the beam pipe.

During the traveling time inside the storage cell the atoms might suffer from small depolarization effects. Therefore the target polarization has to be monitored. A fraction of the target gas is collected by a sample tube and analyzed by a Breit-Rabi polarimeter (BRP), that reverses the ABS scheme. The nuclear polarization is determined combining measurements with different adiabatic high frequency transition units of the polarimeter. The relative number of atoms and molecules in the gas samples is measured by the Target Gas Analyzer (TGA). This measurement is used to determine the atomic fraction inside the storage cell.

The target polarization is calculated as follows [68]:

$$P_T = \alpha_0(\alpha_r + (1-\alpha_r)\beta)P_T^a. \tag{4.2.1}$$

Here α_0 represents the initial fraction of nucleons in the atomic state, α_r stands for the fraction of nucleons in atoms surviving recombination, so that $(1-\alpha_r)$ is the fraction of recombined molecules with relative polarization β. P_T^a is the polarization of the atoms in the target. The properties of the sampled gas and those of the gas in the storage cell are related by the sampling corrections c_α and c_P:

$$\alpha_r = c_\alpha \cdot \alpha_r^{TGA}, \qquad P_T^a = c_P \cdot P^{BRP} \tag{4.2.2}$$

The sampling corrections depend on the measured values α_r^{TGA} and P^{BRP}, on the geometry of the storage cell and on its surface properties. The polarization of the molecules is not precisely known and can vary between 0.2 and 1 for hydrogen [69]. It is the main contribution to the systematic error on the target polarization measurement. In 1996-1997 the polarized target was operated with hydrogen with an average polarization of 88%. In 1998-2000 the polarized target was operated with deuteron with an average polarization of 84%.

4.3 HERMES Spectrometer

The HERMES forward spectrometer [70] is divided horizontally into identical top and bottom halves by the electron and (unused) proton beam lines. A schematic view of the detector is given in fig. 4.3.1. The dipole magnet, operated at a deflecting power of 1.3 T·m, provides a vertical magnetic field so that charged particles are deflected horizontally. An iron plate shields the beam lines through the magnet. The angular acceptance is determined by the magnet aperture and the iron plate geometry. It covers the angle between ±40 mrad and ±140 mrad vertically and ± 170 mrad horizontally. Behind the magnet the horizontal acceptance is increased by 100 mrad to account for deflected particles.

In the HERMES coordinate system the z-axis points along the lepton beam direction, the y-axis points vertically upwards, hence the x-axis points out of the center of the ring. The spectrometer includes several sets of tracking chambers in front, inside and behind the magnet, and a group of particle identification (PID) detectors. The location of the all detectors is indicated in fig. 4.3.1.

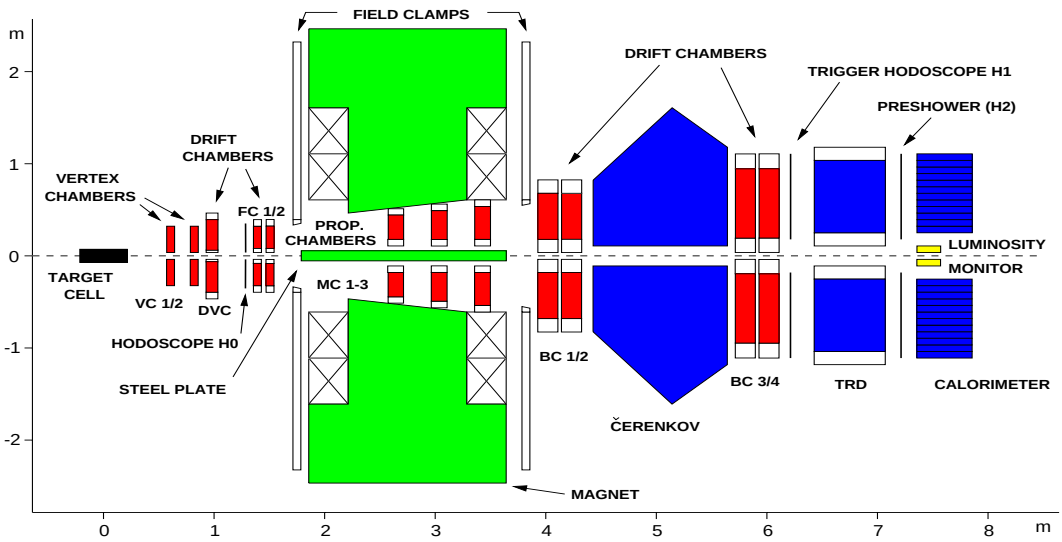

Figure 4.3.1: Schematic view of the HERMES spectrometer.

4.3.1 Tracking Chambers

The reconstruction of the vertex position within the target region and the definition of the scattering angles is provided by the detectors in front of the magnet. These are the microstrip gas counters, referred to as vertex chambers (VC[2]), the drift vertex chambers (DVC) and the front drift chambers (FC). The measurement of the magnetic deflection and hence of the momentum is facilitated by the back drift chambers (BC) , located behind the magnet [71].

[2]Due to efficiency problems the VCs were dismounted in 1998. The recent HERMES data sets for 1996-2000 were reproduced using track reconstruction without VC information. This detector is not discussed any further.

The proportional chambers inside the magnet are used for momentum analysis of low energy decay products which are deflected too much to reach the downstream tracking detectors.

The drift chambers DVC, FC and BC are of conventional horizontal-drift type. Each layer of drift cells consists of a plane of alternating cathode and anode wires between a pair of cathode foils. The cathode wires and foils are at negative high voltage, while the sensitive anode wires are at ground potential. Six drift layers are combined into three coordinate doublets UU', XX', VV' and are assembled as a module. The wires of the X plane are oriented vertically, those of the U and V planes are assembled at an angle of $\pm 30^0$ to the vertical direction. The U', X' and V' planes are staggered by half the cell size with respect to the U, X and V planes, respectively. This is done in order to resolve the left-right ambiguities in the coordinate determination.

A non-flammable gas mixture $Ar(90\%)/CO_2(5\%)/CF_4(5\%)$ at atmospheric pressure is used. The gas system is common for all the drift chambers. A large fraction of the flow is recirculated through the purifiers that remove oxygen and water vapor.

The read-out system of the chambers consists of Amplifier/Shaper/Discriminator (ASD) cards, mounted on-board, driving ECL signals to LeCroy 1877 Multihit FastBus TDCs in the external electronic trailer.

Differences in chamber performance are determined by their design. The efficiency of the chambers is about the same, varying over the planes between 96-99% for DVCs, 98-99% for FCs and 99% for BCs. The spatial resolution for DVCs and FCs is about 230μm and is about 300 μm for BCs. This yields for momentum resolution ($\Delta p/p$) of the whole system about 1% - 2% for the detector configuration used before 1998 and 1.5% - 3% from 1998 on. The angular uncertainty is about 1 mrad. The performances of the detectors are permanently monitored.

Since correlations between atmospheric pressure and the BC performance were observed, they are permanently corrected by a dynamical adjustment of the high voltage settings. A nominal voltage of 1770 V was chosen at an atmospheric pressure of 1013 mbar.

The magnet chambers MC are multi-wire proportional chambers, each consisting of three submodules U, X and V. These are laminated into one module with common gas volume. Each submodule consists of an anode plane at ground potential and two cathode planes with a common negative high voltage connection. A gas mixture $Ar(65\%)/CO_2(30\%)/CF_4(5\%)$ is used. The read-out electronics of the MCs is the LeCroy PCOS-4 system, with the cards mounted on-board, giving digital single bit-per-wire readout. The spatial resolution of the MCs is about 700 μm.

4.3.2 Track Reconstruction

The HERMES reconstruction code (HRC) makes use of the tree-search algorithm for fast track finding and a look-up table for fast momentum determination of the tracks [72].

As a first step, 'partial' tracks have to be found in projections (X,U,V), separately in the region in front of and behind the magnet. The tree-search algorithm looks at the whole hit pattern of the detectors with variable (increasing) resolution as illustrated in fig. 4.3.2. At

each step of the iteration the entire partial track is seen. The iteration procedure is continued until the experimental detector resolution (250 μm) is reached.

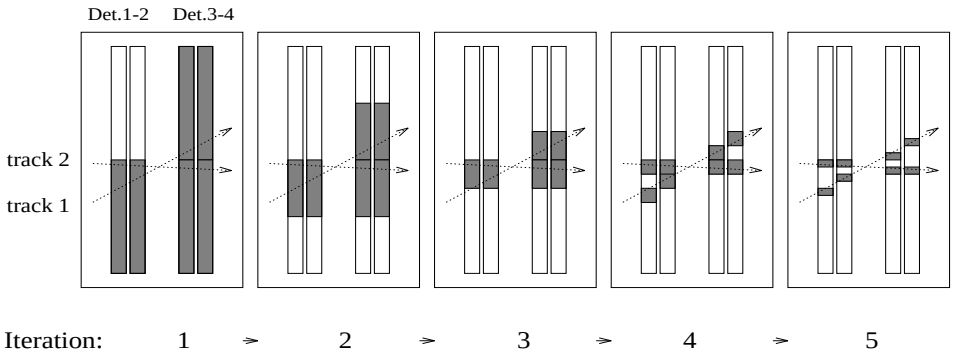

Figure 4.3.2: The tree search algorithm looks at the hits in the tracking detectors with artificially reduced resolution. At each new iteration the resolution is improved by a factor of two.

The number of iterations is typically about 11 and is defined by the detector resolution. The algorithm requires that the pattern contains the sub-pattern, consistent with the allowed track. Allowed patterns are generated and stored in a data base at the initialization step of the program. A large look-up table is generated during initialization. It contains the momentum of a given track as a function of the position and the slope of the track in front of the magnet and its horizontal slope behind the magnet. The comparison is very fast, as almost no calculations have to be done and only look-up tables are used. The number of allowed track patterns at the full resolution is about 10^8.

4.3.3 Particle Identification Detectors

The HERMES particle identification (PID) detector system is designed to distinguish between electrons and hadrons. The rate of DIS electrons is about two orders of magnitude lower than that of hadrons from quasi-real photoproduction. The PID system provides a hadron rejection factor (HRF[3]) of at least 10^4, so that the contamination of the positron sample by hadrons stays below 1% over the whole kinematic range.

The PID detector system consists of a lead-glass calorimeter, two plastic scintillator hodoscopes, one of which is preceded by two radiation lengths of lead and acts as a pre-shower detector, and a transition radiation detector. Until 1998 it was complemented by a threshold Cherenkov counter, which was then replaced by the ring-imaging Cherenkov detector (RICH) that will be described in more detail in section 4.4.

The electromagnetic calorimeter is used in the first level trigger to select DIS events by measuring the particle's energy deposition in a localized spatial region. It allows to suppress

[3]The HRF is determined as the total number of hadrons in the spectrometer acceptance divided by the number of hadrons misidentified as electrons.

hadrons by a factor of 100 in the off-line analysis. The calorimeter consists of radiation-hard lead glass blocks (18 radiation lengths each), arranged in two walls of 420 blocks each above and below the beamline. Each block is viewed by a photomultiplier tube. The long time stability of the detector is determined by a measurement of the mean value of the E/p distribution in each run. Here E and p denote the electron energy measured in the calorimeter and the momentum determined by the tracking system.

Before 1998 pion identification was provided by a threshold Cherenkov detector, located between the two BC groups. As radiator a gas mixture of 30 % nitrogen and 70% C_4F_{10} at atmospheric pressure was used. The momentum thresholds for pions, kaons and protons were 3.8, 13.6 and 25.8 GeV, respectively. The body of the detector was constructed of aluminum with entrance and exit windows made of composite mylar-tedlar foil. An array of 20 spherical mirrors focused the Cherenkov light onto 20 large-diameter phototubes.

The transition radiation detector (TRD) provides a hadron rejection factor of about 100 for 90% electron identification efficiency at energies above 5 GeV. The HERMES TRD consists of 6 modules above and below the beamline. Each module contains a radiator and a detector. A pseudo-random, predominantly two-dimensional matrix of plastic fibers is used as a radiator. The detectors are proportional chambers of conventional design, filled with a flammable gas mixture Xe (90%)/CH_4(10%) which is recirculated and purified. The cathode foils are at ground potential, the anode wires are at +3100 V potential necessary to form the field between the wires and sufficient to collect the ionization electrons within the 1 μs ADC gate used in the readout electronics. Both electrons and hadrons deposit energy in the detector due to ionization of the chamber gas. The energy deposited by a 5 GeV pion is about 11 keV. Electrons deposit approximately twice as much due to transition radiation. In the detector response analysis the truncated mean method is used: the largest signal from the six modules is discarded and the average of the signals of the remaining five modules is used. This is done to suppress the contribution of high energy hadrons into the distribution of energy deposited by electrons.

4.3.4 Particle Identification Scheme

To provide good hadron rejection the responses of all PID detectors are combined for further use in a probability-based analysis.

In the PID scheme used before 1998 the responses of calorimeter, preshower and Cherenkov detector were combined to calculate the quantity "PID3",

$$\mathrm{PID3} = lg\ \frac{\mathcal{L}^e_{Cal}\mathcal{L}^e_{Pre}\mathcal{L}^e_{Cher}}{\mathcal{L}^h_{Cal}\mathcal{L}^h_{Pre}\mathcal{L}^h_{Cher}}\ , \tag{4.3.1}$$

representing the logarithmic likelihood that a certain particle has been identified by all these detectors as an electron rather than a hadron. Here $\mathcal{L}^i_j$ is the conditional probability that the observed signal of a detector j was induced by a particle of type i. These probabilities are determined by comparing the detector response functions for every track to typical detector response functions called "parent distributions". The momentum- and angle-dependent parent distributions are derived for each detector from the experimental data or from Monte-Carlo simulations.

The TRD information is combined into the quantity "PID5"

$$\text{PID5} = lg \frac{\prod_{i=1}^{6} \mathcal{L}_{TRD}^{e}}{\prod_{i=1}^{6} \mathcal{L}_{TRD}^{h}} . \tag{4.3.2}$$

Combining the PID information of all four PID detectors, the quantity PID3+PID5 is used in the analysis of 1996-1997 data. From 1998 on, the logarithmic likelihood "PID2" is used. It is defined similarly to PID3, but using only the calorimeter and the preshower information. The sum PID2+PID5 is used to distinguish electrons from hadrons in the analysis of data from 1998 on. The distributions of the quantity PID3+PID5 is shown in fig. 4.3.3. The

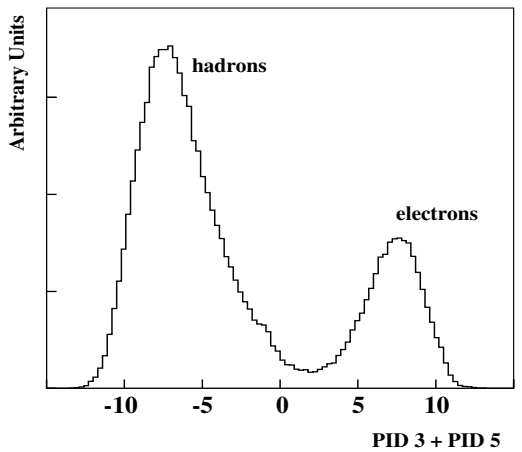

Figure 4.3.3: Distribution of PID3+PID5, the quantity used as PID parameter in 1996-1997 data.

hadron contamination in the electron sample was determined by a fit to the total probability distribution using an assumed shape for the tails of each particle samples in the overlap region. For the hadron contamination a value of 1% at 99% electron identification efficiency was found once the correction for particle fluxes were applied [73].

4.3.5 Luminosity Measurement

The luminosity measurement is based on the detection of elastic Bhabha (Möller) scattering of the beam positrons (electrons) off the target gas electrons, $e^+e^- \to e^+e^-$ ($e^-e^- \to e^-e^-$). The cross sections are known precisely including radiative corrections. The scattered particles exit the beam pipe at z=7.2 m and are detected in coincidence by two calorimeters with a horizontal acceptance of 5÷9 mrad. The symmetric scattering angle, where both scattered particles carry half of the beam energy, is 6 mrad. Each calorimeter is a 3×4 array of 12 radiation-hard Cherenkov $NaBi(WO_4)_2$ crystals, wrapped in aluminized foil and coupled to photomultipliers. The statistical accuracy of the luminosity measurement is about 1% within a measurement time of 100 s.

4.3.6 Trigger

HERMES uses several physics triggers corresponding to deep-inelastic electron scattering and quasi-real photoproduction processes, as well as additional triggers for detector monitoring and calibration.

The DIS trigger is activated if there were hits in the three scintillator hodoscopes H0, H1 and H2, indicated in fig.4.3.1, in conjunction with sufficient energy deposition in two adjacent columns of the calorimeter and in coincidence with the accelerator bunch signal (HERA-clock). H0 suppresses the backwards-going particles from the HERA proton beam, and in conjunction with H1 it rejects the neutral particle background. A calorimeter threshold of 1.4 GeV was used from late 1996 on. The requirement of a calorimeter threshold suppresses the rate of charged hadronic background.

The quasi-real photoproduction trigger detects hadrons produced in electron-nucleon scattering at low Q^2 and decaying into two or more charged particles. Typically the scattered angle of the outgoing electron is too small so that it does not reach the spectrometer acceptance. This trigger requires charged particle tracks in both top and bottom halves of the spectrometer, as identified by the three hodoscopes, the back drift chamber BC1 and the HERA-clock. The back chamber requirement eliminates showers originating from the upstream collimators.

4.4 Ring-Imaging Cherenkov Detector

Pion, kaon and proton identification makes it possible to extract the flavor dependence of the polarized structure functions and the polarization of the sea quarks. Good pion and kaon identification in the momentum range of $2 \div 6$ GeV helps selecting the ρ^0- and ϕ-meson decays for studying the spin properties of vector-meson production.

Monte-Carlo studies show that in the HERMES kinematic region the momenta of 95 % of the hadrons found within the spectrometer acceptance are distributed between 2 and 16 GeV. This defines the momentum range where hadron identification is necessary. The threshold Cherenkov detector at HERMES was only able to identify pions in the momentum region between 4 and 13 GeV. In 1998 it was replaced by a dual-radiator ring-imaging Cherenkov detector (RICH). The HERMES RICH is able to identify pions in the momentum range 0.5-16 GeV, kaons between 2 and 16 GeV and protons between 2 and 20 GeV by the combination of likelihoods calculated for both radiators.

4.4.1 Design Parameters

To cover the necessary momentum range between 2 and 16 GeV a dual-radiator system is used in the detector layout. These radiators are C_4F_{10} gas and clear silica aerogel (SiO_2). The Cherenkov angles for both radiators as a function of the particle momenta are shown in fig. 4.4.1. The refractive index of the gas is 1.0014 which determines the pion, kaon and proton momentum thresholds as 2.7, 9.4 and 17.9 GeV, respectively. The refractive index of

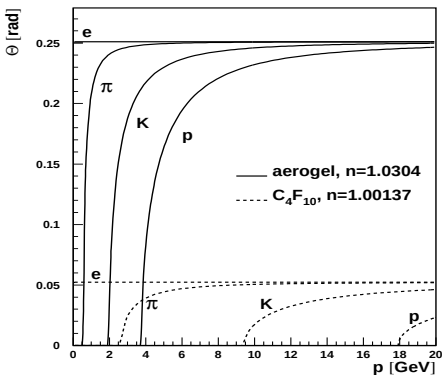

Figure 4.4.1: Cherenkov angle versus hadron momenta for aerogel and gas radiators. If the momentum of the particle is higher than the threshold value for a radiator, it radiates Cherenkov photons on a conical surface under the polar angle θ. The asymptotic value of the Cherenkov angle for high energy particles is about 240 mrad for aerogel and 44 mrad for gas.

aerogel is chosen to be about 1.03, resulting in pion, kaon and proton thresholds of 0.6, 2.0 and 3.8 GeV, respectively.

The HERMES RICH detector [74] consists of two symmetric detector halves installed above and below the beamline, referred to as top and bottom RICH. One half is drawn in fig. 4.4.2. The radiators, the spherical mirror, imaging the Cherenkov light onto a the photon detector, and the photomultiplier (PMT) matrix are shown.

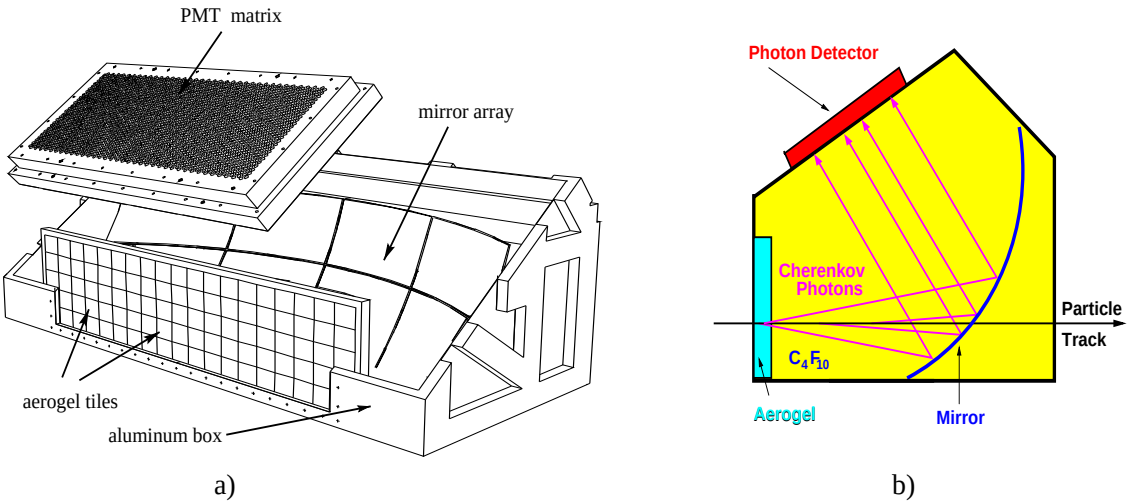

Figure 4.4.2: A cutaway drawing of the (top) RICH counter a) and its operational principle b). Cones of Cherenkov photons, radiated in aerogel and in the gas, are reflected by the mirror onto the photomultiplier matrix (photon detector), producing the ring images.

The detector reuses the aluminum boxes of the old Cherenkov counter. The entrance and exit windows are made of 1 mm thick aluminum. The inner walls of the box are blackened to reduce wall reflections. The aerogel wall is positioned directly behind the entrance window.

The aerogel wall represents a 5.5 cm thick matrix of $17 \times 5 \times 5$ aerogel tiles, commercially available from Matsushita Electric Works. The aerogel tiles in the top and the bottom detectors were selected according to their refractive indices, the resulting averages being 1.0307 and 1.0304, respectively [75]. The remaining volume of the detector is filled with gas at a slight overpressure with respect to the atmosphere.

Each of the spherical mirrors consist of eight segments, arranged in 2×4 arrays. The segments are fabricated from a graphite fiber composite, coated with an epoxy film to provide an optically smooth surface and aluminized, yielding a reflectivity of above 85 %. The radius of curvature of the mirror arrays is 2.2 m.

In the aerogel the Cherenkov photons are emitted mostly in the visible wavelength range. These in the gas have an ultra-violet (UV) component. Therefore Phillips XP1911/UV (green-enhanced) PMTs were chosen as photodetectors. These PMTs, with a sensitive area of about 2.7 cm^2, are arranged on a hexagonal closed-packed matrix of 147×63 cm, centered on the mirror focal point. The elementary cell of the array is a hexagon with the PMT in the center. To increase the amount of collected light a conical funnel is inserted in front of each PMT.

The readout of the photon detector is accomplished by the LeCroy PCOS4 acquisition system. Each detector half is read out by a set of 8 sections, each containing 15 PCOS4 cards. Each card processes signals from 16 PMTs. When the PMT pulse exceeds the threshold of 0.1 photoelectrons, a digital "yes" response is recorded. No analog information is provided.

4.4.2 Angle Reconstruction

The sensitive face of the flat photon detector does not conform to the true focal surface of the mirror. Therefore the patterns seen by the PMT matrix are not rings, but in general asymmetrically distorted ellipses. Hence a ring fitting procedure can not be applied for an accurate reconstruction of the Cherenkov angles. Two algorithms of Cherenkov angle reconstruction for the HERMES RICH were developed: the direct ray tracing (DRT) and the inverse ray tracing (IRT) methods. As input information in both approaches the list of PMT hits per event and parameters of the particle tracks determined by the tracking detectors are used. These algorithms are described in detail in Ref. [76], Ref. [77] considers the possibility to combine both methods into a uniform reconstruction scheme.

The DRT method is based upon Monte Carlo simulations. The generation of Cherenkov photons is simulated along every reconstructed track for each particle type hypothesis. These photons are tracked to the photon detector and the probability for those to hit a PMT is calculated. This hit probability is then compared to the actual hit pattern which results in the probability that the detected hits were caused by Cherenkov light from the observed tracks. The advantage of this method is the accurate determination of the hit probability for each PMT. This makes it possible to easily treat multiple-track events. However, because of the large number of calculations the method is time-consuming and no intermediate information (e.g. Cherenkov angle) can be delivered.

Currently the inverse ray tracing method is used for Cherenkov angle reconstruction at HERMES. The geometrical problem of the IRT can be formulated as follows: for each track

and radiator, given the photon emission point E, the center of the fired PMT D and center of the mirror C, find the reflection point on the mirror S, as shown in fig. 4.4.3. The IRT method

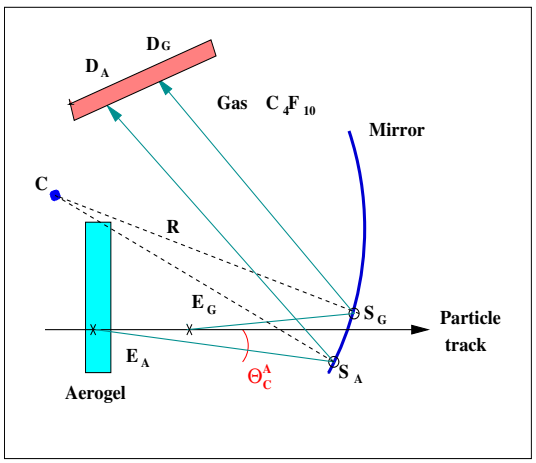

Figure 4.4.3: The geometrical problem of the inverse ray tracing method.

reconstructs the emission angle for each hit, provided the emission vertex is known. For each track it is assumed that the hit could be coming from the aerogel or from the gas, and the emission vertex is estimated accordingly. For each radiator hypothesis the emission angle is then reconstructed. In case of the aerogel radiator the reconstructed angle is corrected for the additional refraction on the boundary between the aerogel and the gas, as described in Ref. [75]. The selection of the most probable particle type is made by calculation of the likelihood that each particle type would generate the measured IRT spectrum.

The yields of aerogel and gas hits vary strongly over the spectrometer acceptance. Therefore the particle identification is based on reconstructed average angles, determined in the window $[\theta_{th} - \sigma_w; \theta_{th} + \sigma_w]$, imposed on the reconstructed angular spectra. The theoretically expected angles θ_{th} are calculated for every particle type hypothesis. The width of the window σ_w is set to $4\times\sigma$, where σ is the single-photon resolution which was determined to be about 8 mrad for both radiators.

The reconstruction delivers the Cherenkov angle and the number of fired PMTs for every track. This data together with other track information (position, momentum, hadron/lepton PID from TRD and calorimeter) are used for the calculation of likelihoods for a hadron to be of a specific type (π, K, p) following the selection rules, as shown in fig. 4.4.4. The theoretical Cherenkov angle θ_{th}, the measured average Cherenkov angle $< \theta >$ and the single photon resolution σ are used as input parameters. The likelihoods are calculated for gas and aerogel separately and then combined by multiplication to form the likelihoods for a hadron to fulfill the pion, kaon and proton hypothesis.

A RICH quality parameter (RQP) is defined as decadic logarithm, $RQP = lg\left(\frac{L_1}{L_2}\right)$, where L_1 is the maximum likelihood for a certain particle type hypothesis and L_2 is the second largest likelihood. If the likelihoods for the two most likely hypotheses are equal (RQP=0), the hadron type can not be identified. Hence the RICH classifies hadrons as kaons (K),

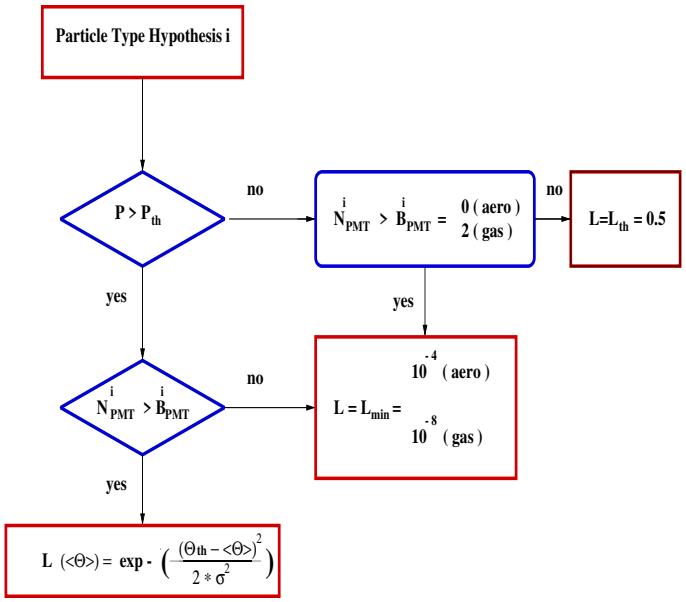

Figure 4.4.4: Flow-chart of the likelihood mechanism: p – particle momentum, N_{PMT} – number of fired PMTs, L – likelihood for the hypothesis i; p_{th} – momentum threshold for aerogel or gas; B_{PMT} – number of background PMTs, L_{th} – threshold likelihood; L_{min} – minimum likelihood.

pions (π), protons (p) or as non-identified particles (X). The advantages of the IRT method are its speed and the fact that intermediate information is available on the Cherenkov angle for every track. The treatment of multiple tracks, however, might be problematic (cf. the discussion in the next section). The Cherenkov angles for pions, kaons and protons measured at HERMES, reconstructed with the IRT method, are plotted versus momentum in fig. 4.4.5.

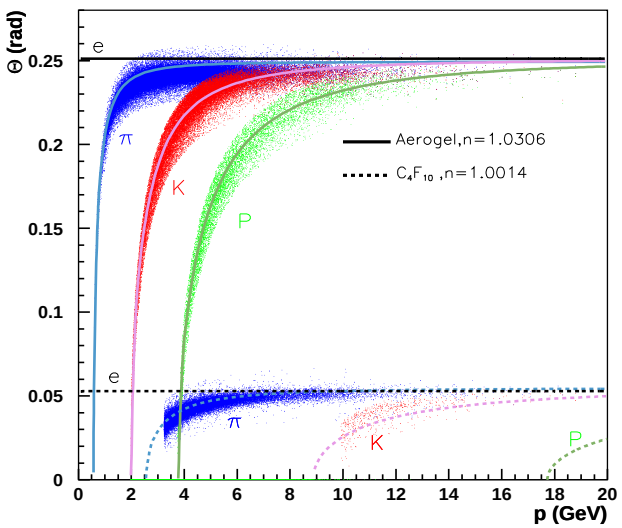

Figure 4.4.5: Momentum dependence of the Cherenkov angle in the HERMES RICH for different particle types. Points represent data and lines theoretical curves (cf fig. 4.4.1).

4.4.3 Hadron Identification Efficiencies

The RICH particle identification efficiencies were studied in Ref. [78]. Other PID detectors are used to select the hadron sample and the RICH PID is used to separate different hadron types. The probabilities for a hadron of the true type t ($t = \pi$, K, p) to be identified as type i ($i = \pi$, K, p, X) form the matrix $P = P_t^i$ of efficiencies and misidentifications:

$$P = P(\pi, K, p) = \begin{pmatrix} P_\pi^\pi & P_K^\pi & P_p^\pi \\ P_\pi^K & P_K^K & P_p^K \\ P_\pi^p & P_K^p & P_p^p \\ P_\pi^X & P_K^X & P_p^X \end{pmatrix} . \tag{4.4.1}$$

The diagonal elements P_i^i of the 3×3 sub-matrix of the matrix (4.4.1) without the last row, containing the not identified particles, are called efficiencies. The remaining elements of the P-matrix are called misidentifications. The P-matrix describes the performance of the detector and can therefore be sensitive to all detector effects. It can depend on particle momentum, position of the track in the detector and track multiplicity of the event.

Note that in general for the analysis of inclusive hadron production the number of hadrons identified with the RICH has to be weighted by purities and contaminations. These are the probabilities Q_t^i that a particle, identified as type i, is truly of type t. Purities and contaminations form the matrix $Q = Q_t^i$:

$$Q = Q(\pi, K, p) = \begin{pmatrix} Q_\pi^\pi & Q_\pi^K & Q_\pi^p & Q_\pi^X \\ Q_K^\pi & Q_K^K & Q_K^p & Q_K^X \\ Q_p^\pi & Q_p^K & Q_p^p & Q_p^X \end{pmatrix} . \tag{4.4.2}$$

The diagonal elements Q_i^i of the 3×3 sub-matrix of the matrix (4.4.2), without the last column, are called purities. The remaining elements of the Q-matrix are called contaminations. If the hadron flux factors ϕ_h are known, the elements of the Q-matrix can be obtained from those of the P-matrix:

$$Q_t^i = \frac{P_t^i \cdot \phi_t}{\sum P_s^i \cdot \phi_s} . \tag{4.4.3}$$

When studying the RICH PID efficiencies and contaminations the task can be formulated as follows [79]: given a number of hadrons identified with the RICH as π, K, p or X, determined by $\vec{I} = (I_K, I_\pi, I_p, I_X)$, find the true number of pions, kaons and protons $\vec{N} = (N_\pi, N_K, N_p)$. The vectors $\vec{I}$ and $\vec{N}$ are connected via the efficiency matrix P and the purity matrix Q.

In Ref. [78] the matrix elements P_t^i are determined in dependence on the particle momentum considering different track multiplicities. The efficiencies are shown to be independent on the position of the track in the detector [80]. As there is no other detector at HERMES able to separate pions, kaons and protons, hadron decays of ρ^0, ϕ, K_s^0 and Λ were chosen to select clearest possible pion, kaon and proton samples.

Usage of particle decays for the determination of the P-matrix elements utilizes the fact that the peak in an invariant mass distribution of decay hadrons contains only hadron types, specific for this decay. For illustration the decay $\phi \to KK$ can be used. In fig. 4.4.6 the

invariant mass of two hadrons with the kaon mass assumption is shown for different RICH PID hypotheses on the hadron type. The top left picture corresponds to the invariant mass distribution of two hadrons with no requirement on the RICH response. The top right one corresponds to the requirement that one of two hadrons was identified as a kaon. In such a way the following samples are formed: one hadron identified with the RICH as a kaon (K H), both are identified as kaons (K K), one identified as kaon while the second is identified as pion (K π), proton(K p), or not identified (K X).

In case of a 100% efficient RICH PID the invariant mass of the events with hadrons not identified as kaons should not form a peak. The observed peaks in any of the distributions (K, not-K) are formed by misidentified kaons produced in ϕ-meson decays. The efficiency and misidentification values of the row P_K^i of the matrix are then determined as

$$\begin{aligned} P_K^K &= N(KK)/N(KH) \ , \\ P_K^\pi &= N(K\pi)/N(KH) \ , \\ P_K^p &= N(Kp)/N(KH) \ , \\ P_K^X &= N(KX)/N(KH) \ . \end{aligned}$$

Here N stands for the number of events in the peak of the invariant mass distribution after background subtraction.

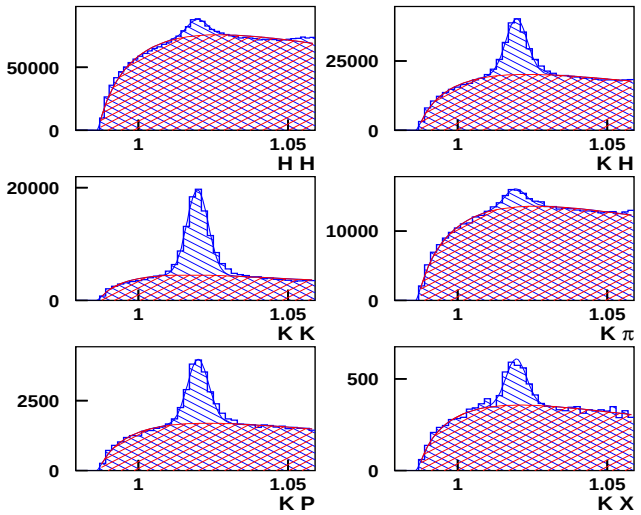

Figure 4.4.6: Reconstructed invariant mass distributions of two hadrons with a kaon mass assumption. One hadron is identified with the RICH as a kaon, the other hadron in the pair has different RICH hypotheses, indicated by the label under the horizontal axis of each plot.

The elements of the P-matrix determined is such a way and binned in hadron momentum are shown in fig. 4.4.7. Different track multiplicities per detector half are separately considered: 1, 2, and more than 2 tracks in case of pions, and 2 and more than 2 tracks in case of kaons and protons[4]. Several features of these dependences are discussed in the following.

[4]The track multiplicity per detector half in case of Λ- and ϕ-decays is defined by the decay topology in the detector acceptance, e.g. 95% of the kaons from ϕ-meson decays end up in the same detector half.

A drop in the pion efficiency appears at about 2 GeV where pions are just starting to radiate in the gas. Close to the threshold, pions might fire not yet enough gas PMTs to satisfy the pion hypothesis, therefore the gas likelihood is low. Above 9 GeV the pion Cherenkov angle is close to that of kaons which makes it difficult to distinguish between these hadrons. Between 2 and 4 GeV pions accompanied by more than one additional track are more likely to be misidentified as kaons, because due to ring overlap a few gas hits belonging to a pion can be assigned to an accompanying track.

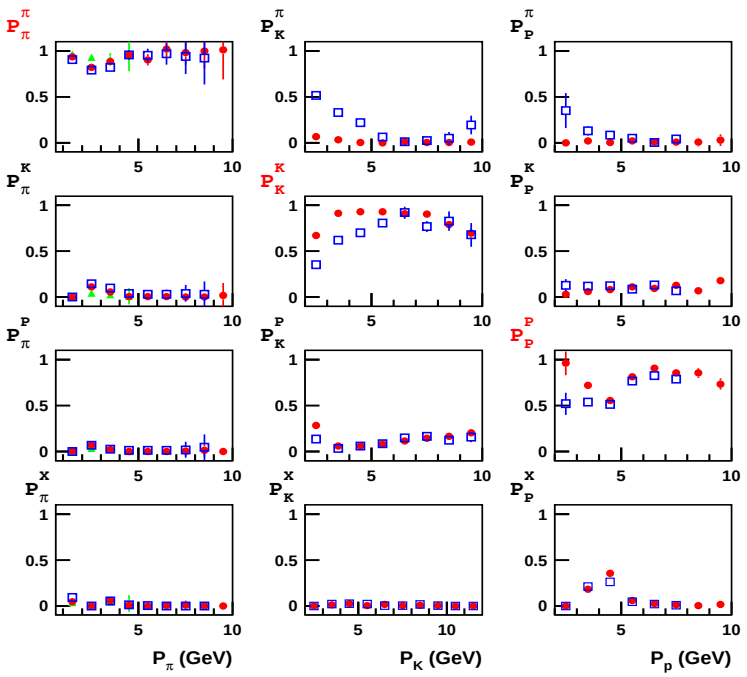

Figure 4.4.7: The efficiency matrix elements P_t^i, determined from particle decays, shown in dependence on hadron momentum. Different track multiplicities per detector half are considered separately: 1 track (triangles), 2 tracks (filled circles), more than 2 tracks (empty squares).

In the momentum range between 2 and 3 GeV, near the aerogel threshold, kaons produce too few Cherenkov photons to have enough PMT hits in the kaon aerogel window. Therefore they can be misidentified as subthreshold protons. If another track accompanies the kaon in the event, the kaon can be misidentified as pion due to ring overlap. After 3 GeV the efficiency stays as high as about 80% up to momenta of about 9 GeV. Above 9 GeV kaons start radiating in the gas which results in a decrease of the kaon likelihood similarly to that in the pion case. In addition, as already mentioned, above 9 GeV the kaon Cherenkov angle is close to that of pions which makes it difficult to distinguish between these hadrons. If the event has more than 2 tracks per detector half, hits in the gas window of the additional track can be combined with kaon hits in the aerogel window. This also leads to misidentification of kaons as pions.

The RICH identification of the proton starts at 2 GeV. If a hadron with momentum between 2 and 4 GeV has hits neither in the aerogel nor in the gas, it is identified as proton. From 4 GeV on the likelihood calculation is applied for protons, leading to a drop in the identification efficiency.

Chapter 5

Analysis of Double-Spin Asymmetries

Double-spin asymmetries in exclusive diffractive production and quasi-real photoproduction of ρ^0- and ϕ-mesons in lepton-nucleon scattering were investigated. Data of the HERMES experiment were used, obtained using longitudinally polarized proton and deuteron targets. Double-spin asymmetries in exclusive ρ^0-meson production on proton and deuteron targets were measured for the first time at SMC [81] at the $\gamma^* N$ center-of-mass energy of $< W >= 15$ GeV. No significant asymmetry for both targets was observed in the region $0.01 < Q^2 < 5$ GeV^2. At intermediate energies of HERMES, $< W >= 4.5$ GeV, the double-spin asymmetry in the cross-section of exclusive diffractive production of ρ^0-meson on a proton target is described in Refs. [82, 46]. An evidence for a positive double-spin asymmetry in exclusive ρ^0-meson production was reported. Double-spin asymmetries in vector-meson production in the quasi-real photoproduction regime were not investigated at HERMES up to now.

5.1 Event Selection Criteria

The first important step in the event selection for the specific physics analysis is to assure a good quality of the data sample regarding the detector performance. This is done in order to minimize systematic uncertainties caused by the experimental conditions. All subsystems of the spectrometer have to operate reliably and stable, good beam conditions and a high quality of target operation are required.

Additional 'physics' cuts have to be applied to select the desirable physics process. Events originating from other processes and forming the 'background' for the studied one have to be removed. These particular selection criteria are chosen to minimize the background contamination in the event sample, keeping the statistics of useful events as high as possible.

5.1.1 Data Organization and Data Quality

The data collected at HERMES have to undergo several steps of processing before they can be used in the physics analysis. A basic unit in data taking and processing is an event. One event corresponds to an interaction of a beam particle with the target nucleon, it contains all

detector information recorded by the data acquisition system (DAQ) for a generated trigger. During the data taking the event stream is artificially divided into bursts, about 10 seconds long each. These bursts are grouped into runs. The amount of data collected in each run is determined by the tape size of the central storage system. A run contains roughly 50 bursts. Each run belongs to a certain beam fill of the HERA machine, which typically lasts for about 8 hours. The data is further characterized by the data taking year during which it is collected.

The conversion of the raw detector data into the analyzable form is performed in several steps. First, the raw run files in EPIO (Experiment Physics Input Output) format are translated by the HERMES decoder program (HDC) into the output format, based on the tabular structure of the ADAMO package. The decoded detector information is passed to HRC. On this stage of the data production calibration, alignment and efficiencies of the tracking chambers are calculated. The data from the HRC outputs are combined with the corresponding information from the slow control, accomplished by some additional expert information. Compact run files are then produced in a form of μDSTs (Data Summary Tapes), to be finally used in physics analysis. The data quality criteria are slightly different for every year of data taking, as the experimental conditions varied in different running periods. In the following only general requirements on data will be discussed, more or less common for every μDST production.

Data quality selection is done on the fill, run and burst level. Fills and runs dedicated to detector calibration or maintenance and machine studies are removed. If the slow control information is missing for a certain run, this run is discarded. The general data quality requirements are listed in table 5.1.1.

parameter	cut
beam polarization	$0.3 \leq P_B \leq 0.8$
burst length	$0 \leq L_b \leq 11$ s
trigger lifetime	$50 < \tau_{life} < 100\%$
beam current	5 mA $\leq I \leq$ 50 mA
fitted luminosity rate	5 Hz $\leq L \leq$ 60 Hz
target state	2-state flipping mode
tracking detectors	no high voltage trips
PID detectors	fully operating
spectrometer magnet	on
luminosity monitor	no dead blocks
calorimeter, H2	no dead blocks

Table 5.1.1: General data quality cuts on the experimental conditions

Periods of low polarization do not contribute much to the asymmetry measurements and are removed from the data set. The beam polarization value is required to be within certain limits. The lower limit cuts away periods with low polarization. It removes also the data taken at the beginning of each fill when the polarization value was still rising.

A well-defined nuclear polarization state of the target is required. While the polarization direction of the polarized target is flipped, it stays undefined for a few seconds. In addition the atomic fractions α_0 and α_r (cf. Eq. (4.2.1)) are restricted to be positive values and a regular update of the α measurement is required.

The data acquisition system is required to perform stable in time. The DAQ performance can be characterized by the lifetime, the fraction of time the DAQ system is able to accept and record new incoming data without being blocked due to processing of previously accepted data. The lifetime is determined in every burst as a ratio between the number of accepted triggers and the total number of generated triggers.

The lifetime and the burst length are used in the luminosity normalization. Therefore they are required to range within certain limits. The first burst of each run is removed from the data to discard the periods of the initialization of the detector settings.

If during a fill or run any single component of the spectrometer was not working properly or operates unstable in time, all data of the concerned data sample has to be skipped in the analysis. Stable performance of both spectrometer halves at the same time is required.

5.1.2 Selection of the Physics Sample

The ρ^0 and ϕ-mesons decay immediately[1] after their formation and do not reach the spectrometer. At HERMES these vector mesons can be detected only by their decay products in the channels $\rho \to \pi^+\pi^-$ and $\phi \to K^+K^-$.

Two topologies of vector-meson production are considered in the selection of the vector-meson sample for asymmetry analysis. In *exclusive* vector-meson production the scattered electron is detected in the spectrometer acceptance together with the meson decay products. In *quasi-real photoproduction* of vector mesons, in contrast, only the decay products of the vector meson are detected, while the scattered electron remains undetected in or close to the beam pipe.

The nucleon, recoiled in the process of vector-meson production, remains undetected[2]. The kinematics of the recoiled nucleon in exclusive vector-meson production process can be reconstructed using the kinematics of the meson decay products and the scattered electron. In the case of quasi-real photoproduction the event kinematics can not be fully determined.

Several track reconstruction methods were used in the data production to cope with different configurations of the tracking system in front of the magnet. The information from the vertex chambers (VCs) is used in the standard track reconstruction method (STD), while is ignored in the NOVC method. In 1998 the VCs were dismounted and the usage of the STD reconstruction became impossible from 1998 on. For consistency the NOVC reconstruction algorithm was used for all data productions, i.e. the μDST versions 96c1, 97c1, 98c1, 99b2, 00b1. The first two digits in this notation stand for the year of data taking. At the time of carrying out this analysis these μDST versions were the most recent productions available.

[1]The lifetime of these vector mesons can be estimated from their widths as $\tau = \frac{h}{\Gamma}$. The calculation gives lifetimes $\tau_\rho = 4.4 \cdot 10^{-24}$ s and $\tau_\phi = 1.7 \cdot 10^{-22}$ s.

[2]It is not yet possible at HERMES to detect the recoiled particle. Presently, an effort is being made to construct a recoil detector at HERMES [83].

The data collected in 1996 and 1997 were obtained using the polarized proton target, from 1998 on the polarized deuteron target was used.

To select a clean data sample, to exclude background and to separate electrons and hadrons of different types, certain constraints were applied on every track in the event. Each track in the event is required to come from inside the target cell. Therefore cuts were imposed on the position of the reconstructed vertex along the z-axis and the transverse offset of the vertex from the z-axis. To ensure that the electron has deposited all its energy in the calorimeter, a fiducial volume cut is applied. The same cut helps avoiding the region of the shielding plate in the magnet. A kinematic limitation on the photon fractional energy y (Eq.(1.1.6)) was set to select the region where radiative corrections are minimal. Tracks with a momentum below 0.5 GeV do not reach the back region of the detector. These short tracks are excluded from the analysis and only full tracks are used. The track selection criteria for ρ^0- and ϕ-meson samples are listed in table 5.1.2.

Quantity	Cut
Particle Identification	
electron identification	PID3+PID5>0 (1996-1997) PID2+PID5>0 (1998-2000)
hadron identification	PID3+PID5<0 (1996-1997) PID2+PID5<0 (1998-2000)
pion identification	Cherenkov.: pion ID (1996-1997) RICH: pion ID (1998-2000)
kaon identification	Cherenkov.: pion ID(1996-1997) RICH: kaon ID (1998-2000)
Vertex and Geometry	
reconstructed vertex	$\lvert z_{vert}\rvert < 18$ cm
transverse vertex offset	$\lvert t_{vert}\rvert < 0.75$ cm
fiducial volume cut	passed
Kinematics	
small radiative corrections	$y < 0.85$

Table 5.1.2: Track selection criteria

To separate hadron and electron tracks, cuts according to the PID scheme were applied. To identify between the hadron types the PID information of the Cherenkov detector was used for the data collected in 1996-1997, from 1998 on the RICH PID was applied. The Cherenkov detector information, however, was used only for the samples of quasi-real photoproduction of ρ^0- and ϕ-mesons, as discussed in the following.

5.1.3 Selection of Exclusive Diffractive Events

Exclusive vector-meson production $e + N \to e' + V + N'$ requires that no other particle was produced in the process, e. g. through target break-up. Therefore only those events having

exactly 3 tracks are selected, containing the scattered electron and two oppositely charged hadrons of the specific type. Three main types of background can be distinguished:

- Non-resonant background formed by events that contain hadron pairs produced in the fragmentation process, through the production of other particles decaying into hadrons. Exclusive pion pair production without formation of an intermediate vector-meson state belongs to this class of background, as well.
- Non-exclusive background formed by events which contain one or more additional tracks that escaped the detector acceptance. These events originate e.g. from ρ^0-meson production in the fragmentation process.
- Background formed by events originating from non-diffractive processes.

For background suppression, as described in the following, certain limitations on kinematic variables have to be used and the hadron separation, if available, should be applied. The summary of the cuts is given in table 5.1.3. The numbers of obtained ρ^0- and ϕ-candidates are listed in Appendix 1.

Quantity	Limitation	
	$\rho^0 \to \pi^+\pi^-$	$\phi \to K^+K^-$
Hadron Identification	RICH pion ID (1998-2000) $p_\pi > 0.5$ GeV	RICH kaon ID (1998-2000) $p_K > 2.0$ GeV
Invariant mass	$0.6 < M_{\pi\pi} < 0.9$ GeV	$1.01 < M_{KK} < 1.03$ GeV
Background mass	$M_{KK} > 1.06$ GeV (1996-1997)	none
Missing energy	$\Delta E < 0.6$ GeV	$\Delta E < 1.0$ GeV
Momentum transfer	$-t' < 0.4$ GeV^2	$-t' < 0.6$ GeV^2

Table 5.1.3: Set of requirements for the selection of exclusive diffractive ρ^0- and ϕ-candidates.

Hadron Identification In the analysis of ρ^0- and ϕ-mesons production it is required that both detected hadrons are pions or kaons, respectively. For the data collected in 1996-1997 hadron separation can be performed using the Cherenkov detector. The capability of this detector to identify pions is limited to a certain momentum range. To avoid losses of statistics, the information of the Cherenkov detector is not used for the hadron identification in the sample of candidates for exclusive ρ^0- and ϕ-meson production. The pion and kaon samples are therefore contaminated with hadrons of other types. From 1998 on the possibility of hadron separation with the RICH detector is used. Cuts on the hadron momenta were applied to provide the efficient hadron identification: $p_K > 2$ GeV, $p_\pi > 0.5$ GeV.

Invariant Mass The production of ρ^0- or ϕ-mesons is identified by the resonance peak in the invariant mass distribution of two hadrons with pion or kaon mass assumption, respectively. The invariant mass of two hadrons is determined as

$$M_{h^+h^-} = \sqrt{(p_{h^+} + p_{h^-})^2}\ , \tag{5.1.1}$$

where $p_{h^\pm}$ are 4-momenta of positive and negative hadrons, which are assumed to be pions or kaons. The 2-hadron invariant mass distributions for pions and kaons are shown in fig. 5.1.1. The candidates of the ρ^0- and ϕ-meson production are those in the peak of the invariant

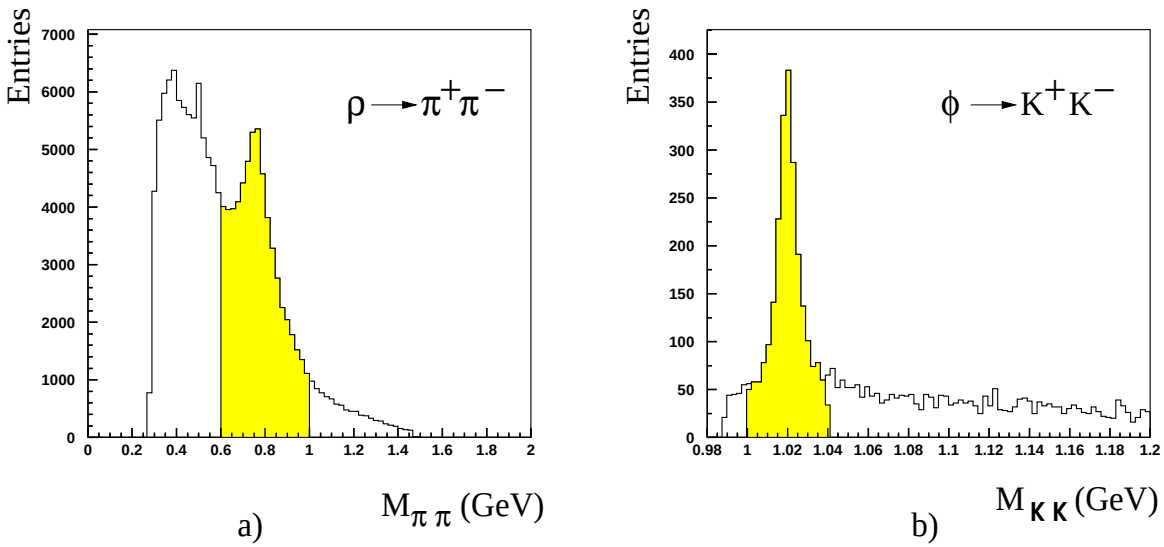

Figure 5.1.1: Invariant mass distributions of two a) pions from ρ^0-decays and b) kaons from ϕ-decays. The narrow peak in the lower mass region on the panel a) corresponds to K_s^0 production. Combined 1998-2000 data set, obtained with polarized deuteron target. The shaded areas mark events used for analysis. Pion and kaon identification is performed with the RICH detector.

mass distributions within the windows $0.6 < M_{\pi\pi} < 0.9$ GeV and $1.01 < M_{KK} < 1.03$ GeV, respectively.

As discussed above, no hadron separation is performed for the data collected in 1996-1997. Therefore to select the ρ^0-meson candidates, additional requirement on the invariant mass of two hadrons is applied. Some background events coming from ϕ-meson production end up in the mass range of 0.3-0.45 GeV. To clean up the invariant mass spectrum of the ρ^0-meson candidates, the cut on the invariant mass of two hadrons in the ρ^0 sample, assuming these are kaons, $M_{KK} > 1.06$ GeV, is used. In the data, collected in 1998-2000 the RICH pion identification is used and this additional limitation is not necessary.

Missing Energy The missing energy ΔE is determined as the difference in the invariant mass of the incoming nucleon and that of the undetected hadronic system

$$\Delta E = \frac{M_x^2 - M_N^2}{2M_N} = \nu - E_v + \frac{t}{2M_N} \ . \tag{5.1.2}$$

Here M_x stands for the rest mass of the recoiling system, $M_x = \sqrt{(p+q-p_v)^2}$. For exclusive events M_x will be equal to the mass of the target nucleon M_N, giving $\Delta E = 0$. The reconstructed ΔE distributions with the invariant mass in the window of ρ^0- and ϕ-mesons

production are shown in fig.5.1.2. Exclusive events are those in the peak around zero. The width of the peak is determined by the detector resolution. For data taken in 1996-1997 the resolution for the missing energy was about 0.28 GeV for exclusive ρ^0-meson production. After the RICH installation in 1998 the ΔE resolution for these vector mesons increased by about 0.10 GeV due to the presence of additional material.

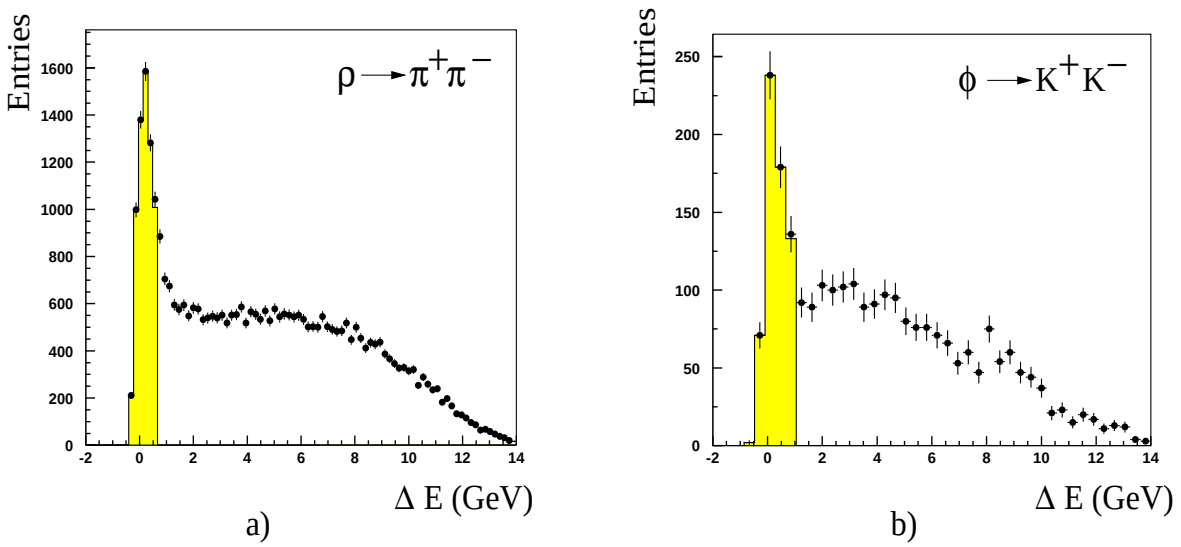

Figure 5.1.2: Missing energy distributions for a) ρ^0 and b) ϕ-mesons production from the combined 1998-2000 data on a polarized deuteron target. The shaded areas mark the events used for analysis. The invariant mass windows $0.6 < M_{\pi\pi} < 0.9$ GeV and $1.01 < M_{KK} < 1.03$ GeV are imposed. Here and further the error bars represent statistical uncertainties unless otherwise noted.

In the case of scattering on a composite nucleus contributions of two processes should be separated: incoherent scattering, where the nucleus goes into an excited state or breaks up and the scattering process proceeds on individual nucleons; and coherent scattering off the entire nucleus. Therefore for the "coherent" part of Eq. (5.1.2) the mass of the target nucleus should be taken as M_N. Due to limited detector resolution it is impossible to distinguish between coherent and incoherent scattering. Hence for scattering on both hydrogen and deuterium targets the proton mass is taken as M_N in Eq. (5.1.2). The exclusive coherent scattering events give slightly negative values in the ΔE distribution. Events with non-zero ΔE values correspond to non-exclusive processes. The cut ΔE <0.6 GeV is used to select the exclusive ρ^0-meson candidates [84, 85]. Selection of the exclusive ϕ-meson candidates is accomplished by the cut $\Delta E < 1.0$ GeV. The missing energy limit for ϕ-meson selection is relaxed in comparison to the case of the ρ^0-meson in order to improve the statistics of the ϕ-meson candidate sample.

Photon Energy For better selection of the exclusive processes the photon energy ν was required to be within a certain region $9 < \nu < 22$ GeV. The lower limit is necessary because of the kinematic relationship between ΔE and ν. At $\nu < 9$ GeV the non-exclusive events

occur at $\Delta E < 3$ GeV and can not be cleanly separated from the exclusive events. The requirement of the upper limit forces the electron energy to be well above the calorimeter threshold of the trigger and ensures high trigger efficiency.

Momentum Transfer to the Target Diffractive interactions are dominated by forward scattering, i.e. they occur at small values of squared four-momentum transfer to the target, $|t'|$. To suppress non-diffractive background the cut $-t' < 0.4$ GeV^2 is imposed on the ρ^0-sample. A wider cut is used for the ϕ-meson sample, $-t' < 0.6$ GeV^2, in order to improve the statistics of the ϕ-sample.

The cross section of diffractive processes exhibits an exponential fall-off (cf. Eq. 1.2.2). As described in section 1.2, in the optical model of diffraction the slope of this fall-off can be associated with the transverse size of the two scattering objects. The distributions of the four-momentum transfer to the target in case of ρ^0-meson production on proton and deuteron targets are shown in fig. 5.1.3 a) and b), respectively.

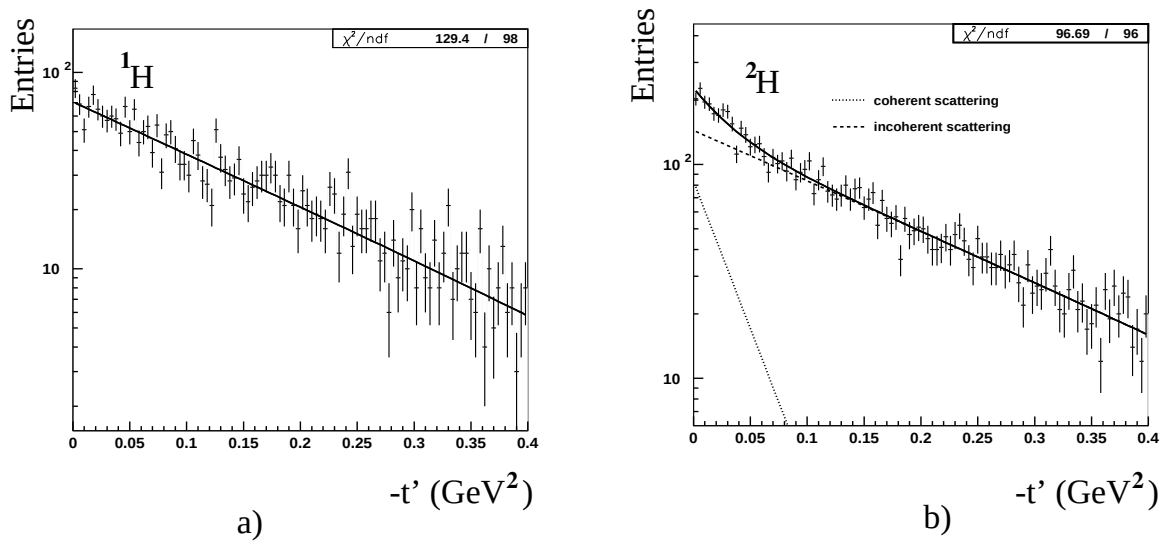

Figure 5.1.3: The $-t'$ distributions for exclusive diffractive ρ^0-meson production on a) proton and b) deuteron targets. The data for the proton target are described by a single exponential. The data for the deuterium are described by a double-exponential shape, taking into account different contributions from coherent scattering off the nucleus and incoherent scattering off the nucleon.

The data show the expected exponential behavior. In the case of the proton target the $-t'$-distribution was fitted with a single exponential function. The resulting slope is given in table 5.1.4. In the general case of scattering on a composite nuclei, the $-t'$-spectrum is described by a double exponential function [84]

$$\frac{d\sigma}{d|t'|} = A(\sigma_{inc} b_{inc} e^{-b_{inc}|t'|} + \sigma_{coh} b_{coh} e^{-b_{coh}|t'|}). \tag{5.1.3}$$

The incoherent and coherent parts of the cross section are determined by the slopes b_{inc} and b_{coh}, respectively. The $-t'$-distributions for deuteron target was fitted with the shape (5.1.3) using the free parameters A, σ_{inc}, σ_{coh}, b_{inc} and b_{coh}. The resulting slopes are also listed in

N	slope	χ^2/ndf
^{1}H	6.1 ± 0.2 GeV^{-2}	129/98
^{2}H	b_{inc}=5.4 $\pm$ 0.4 , b_{coh}=32 $\pm$ 11 GeV^{-2}	97/96

Table 5.1.4: The fitted slope parameters for the ρ^0 production on proton and deuteron targets.

table 5.1.4. The incoherent slope for the deuteron is compatible with the spole measured for the proton. The parameters in table 5.1.4 are in good agreement with results from Refs. [33, 84]. Details of coherent and incoherent scattering are discussed in Ref. [86].

Double-Dissociative Diffraction Both single- and double-dissociative diffraction contribute to exclusive vector-meson production. In contrast to single-dissociative vector meson production, where the nucleon stays intact and the photon forms a vector meson state, in double-dissociative process both particles are excited to a multi-particle state. As the nucleon final state remains undetected at HERMES, it is impossible to distinguish between single- and double-dissociative diffraction. In Ref. [87] the contamination of double dissociation in electroproduction of ρ^0-mesons at high Q^2 is estimated to be as high as $\sim$20%. In Ref. [88] the value of the double-dissociation contribution varies between 20% and 37%, although for a worse ΔE resolution. Within the selected missing energy region $\Delta E < 0.6$ the contamination of double-dissociative diffraction is estimated to vary between 2.7% and 5.3% for HERMES [84]. The cross section of exclusive diffractive ρ^0-meson production can be corrected for the contamination of double-dissociative diffraction [33, 84]. When measuring double-spin asymmetries, however, this correction can not be applied as the asymmetry of double-dissociative diffractive vector-meson production is not known, yet. Therefore the measured double-spin asymmetries include contributions from both single and double dissociative diffractive production of vector mesons.

5.1.4 Selection of Quasi-Real Photoproduction Events

The quasi-real photoproduction events are those at lowest possible Q^2 (cf. definition in section 1.1). Experimentally, the selection of low-Q^2 events is accomplished by the requirement that the scattered electron does not reach the acceptance of the spectrometer and is therefore not detected. The candidate events of quasi-real photoproduction of vector mesons are those with only two tracks in the detector acceptance that are oppositely charged hadrons of the specific type. Hadron separation is especially important in this case. The kinematics of such events can only be partially reconstructed, as the information about the scattered electron track is missing, and any measure of exclusivity like ΔE is not calculable. Hence there is no direct way to suppress the non-exclusive background in the selected sample. The momentum transfer to the target, $|t|$ or $|t'|$, can not be reconstructed, as well. To suppress the background from other processes only the 2-hadron invariant mass can be used. The numbers of selected ρ^0- and ϕ-candidates are given in Appendix 1.

Hadron Separation The information of the Cherenkov detector can be used for hadron identification in the data sample taken in 1996-1997. To suppress the low-energy background

in the ρ^0-candidate events a cut on the momentum of both hadrons, $p_\pi > 3.5$ GeV, was applied. To identify pions the requirement of a signal in the Cherenkov detector (> 0.25 photoelectrons) was used. For kaon identification in the ϕ-meson candidate events, pion rejection is used. The pion contamination in the kaon sample is suppressed by requiring that the momenta of both hadrons in the pair exceed the pion momentum threshold in the Cherenkov counter (4.0 GeV) and produce no signal in this detector (< 0.25 photoelectrons). For the data collected in 1998-2000 the RICH pion and kaon identification was used with the requirement for hadron momenta to exceed the momentum threshold in the aerogel radiator, $p_\pi > 0.5$ GeV and $p_K > 2.0$ GeV, respectively. No further cuts on the kinematics of the event are applied.

5.2 Monte-Carlo Simulations

The determination of the full kinematics in quasi-real photoproduction of vector mesons is experimentally impossible, since the scattered electron is not detected. Some of the kinematic variables can be estimated, however, using the Monte Carlo simulation of such events. In the following the determination of the average values $< x >$ and $< Q^2 >$ for quasi-real photoproduction of ϕ- and ρ^0-mesons is described. The resolution of the invariant mass of ϕ-meson in the HERMES detector is studied using the Monte Carlo simulations, as well.

Determination of $< x >$ and $< Q^2 >$ The Monte-Carlo data were generated with the PYTHIA event generator version 6.1 that was developed from version 5.7 [8] according to the model of photon-proton and photon-photon interactions described in Refs. [7, 89]. The simulation of $\gamma^* p$-interactions is based on the understanding of the photon structure discussed in section 1.3. The process is described [7] by a Q^2-dependent combination of several types of processes, such as direct processes, resolved processes (VMD, GVMD) and DIS, all contributing to the total $\gamma^* p$ cross section. The default settings[3] for kinematic cutoffs, fragmentation parameters, etc. have been tuned to fit data from LEP and TEVATRON with center-of-mass energies of a few hundred GeV. Therefore it can be expected that some of these settings are not applicable at HERMES energies. The tuning of PYTHIA parameters for HERMES is ongoing.

Unpolarized positron-proton scattering was simulated within the simplified "box" acceptance of the HERMES detector selecting events with at least one track in the detector acceptance with a momentum of more than 0.5 GeV. The photon structure was defined according to Ref. [9] implying the mixture of all processes contributing to the total $\gamma^* p$ cross section. The events corresponding to quasi-real photoproduction of ρ^0 (ϕ) - mesons were selected requiring two accepted tracks belonging to oppositely charged pions (kaons) having ρ^0 (ϕ) as a parent particle. No explicit requirement of exclusive ρ^0- or ϕ-meson production was applied[4]. The average values of Q^2 and x for these events were calculated using the kinematics of the scattered positron that escaped the detector acceptance. The distributions of Q^2 and x for quasi-real photoproduction of ρ- and ϕ-mesons are shown in fig. 5.2.1. To check the consistency of data and simulations the distributions of those kinematic variables

[3]The description of the parameter settings used for the event generation can be found in [90].

[4]The fraction of exclusive vector-meson events is 85%, proton break-up occurs in 12% of the cases, the remaining 3% of events originate from other processes

which are calculable both in data and Monte-Carlo have to be compared. The shapes of the momentum distributions of pions (kaons), produced in ρ^0 (ϕ) - meson decays for simulated and experimental data are compared in fig. 5.2.2. The data, collected in 2000, corrected

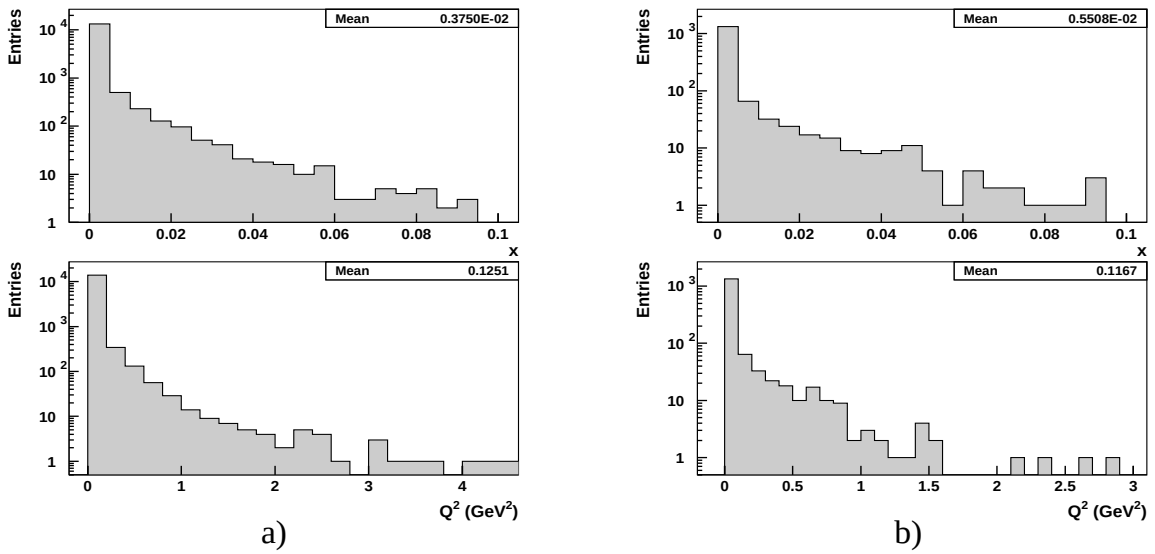

Figure 5.2.1: The distributions of Q^2 and x for quasi-real photoproduction of a) ρ^0-meson and b) ϕ-meson, simulated with the PYTHIA-6.1 generator.

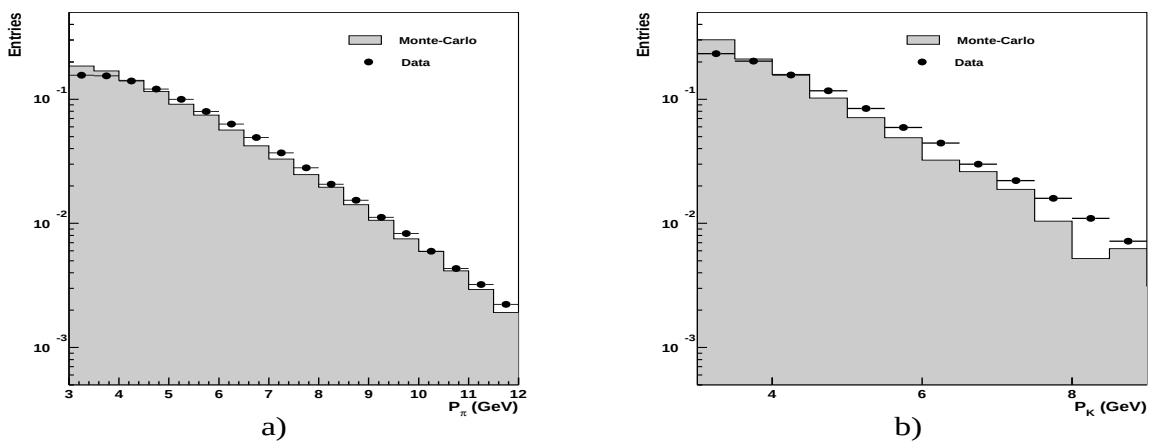

Figure 5.2.2: The momentum distributions of a) pions, produced in ρ^0-meson decay and b) kaons produced in ϕ-meson decay. The data (closed circles), collected in 2000 are compared to PYTHIA-6.1 simulations (shaded histogram).

for trigger efficiencies [91] and RICH identification efficiencies are used. A momentum cutoff at 3.0 GeV was used to select the region of minimal misidentification (cf. fig. 4.4.7). The areas of the spectra are normalized to one. Both pion and kaon momentum spectra are in a fair agreement with the Monte-Carlo simulations.

Smearing of the Invariant Mass Distribution Due to limited detector resolution and efficiency the momentum and angular distributions of the tracks and, in turn, the reconstructed invariant mass distribution are smeared with respect to their original values. This

effect can be negligible in the invariant mass distribution of broad resonances, e.g ρ^0, but it can affect the Breit-Wigner shape of narrow ones. The effect of the two-kaon invariant mass smearing is shown in fig. 5.2.3. The generated invariant mass spectrum of the two kaons from ϕ-meson decay, simulated with PYTHIA-6.1, was fitted with the Breit-Wigner distribution, giving the natural width of the ϕ-meson of $\Gamma_0 = 4.4$ MeV which is in a good agreement with the PDG value.

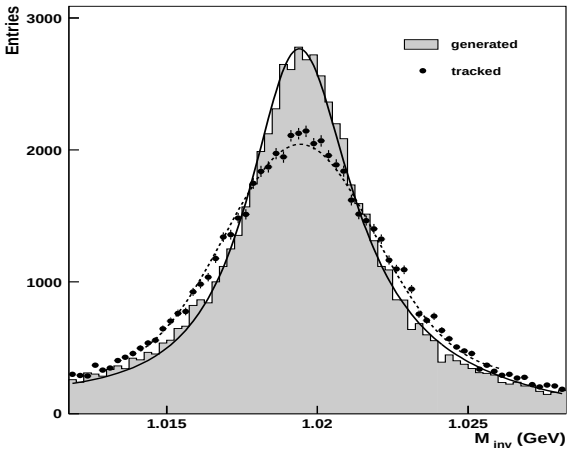

Figure 5.2.3: The two-kaon invariant mass distribution for the generated (shaded histogram) and tracked (closed circles) Monte-Carlo data. The solid line represents the fit to the generated distribution using a Breit-Wigner shape. The dashed line represents the fit to the tracked Monte-Carlo data with a Gaussian distribution.

Monte-Carlo / Data	Fit Function	M_ϕ (MeV)	Width (MeV)	χ^2/ndf
MC generated	Breit-Wigner	1019.5 ± 0.01	$\Gamma_0 = 4.3 \pm 0.2$	164/82
MC tracked	Breit-Wigner	1019.6 ± 0.03	$\Gamma_0 = 6.8 \pm 0.1$	287/82
	Gauss	1019.5 ± 0.02	$\sigma = 3.1 \pm 0.1$	115/8
Data 1997	Gauss	1020.0 ± 0.07	$\sigma = 3.5 \pm 0.2$	62/59

Table 5.2.1: The fitted values of the free parameters of the 2-kaon invariant mass distribution in the Monte-Carlo simulations compared with parameters obtained in the experimental data (cf. section 5.3.2).

The generated events were tracked through the detector using the GEANT - based [92] detector simulation tool HMC (HERMES Monte-Carlo) which includes resolutions and efficiencies of the subsystems. The detector geometry used in the Monte-Carlo corresponds to the detector configuration of 1997. The tracked events were then reconstructed by HRC similarly to the experimental data. The invariant mass distribution after the reconstruction is considerably broader and can no longer be described by a Breit-Wigner shape. A Gaussian distribution is used as an alternative fit shape. The fit parameters are listed in tab. 5.2.1, where the fit parameters, obtained from the experimental data of 1997 are given for comparison.

5.3 Exclusive Diffractive Vector-Meson Production

Double-spin asymmetries in the cross section of exclusive diffractive production and quasi-real photoproduction of ρ^0- and ϕ-mesons are determined using data taken with longitudinally polarized proton and deuteron targets.

Once the selection procedure has been performed, candidate samples of exclusive diffractive ρ^0- and ϕ-meson production are obtained. In those samples the background is already mostly suppressed in the stage of event selection. Further background subtraction is necessary because the events originating from non-resonant hadron pair production and non-exclusive resonance formation, that have passed the selection cuts, are still present in the analyzed samples and can influence the asymmetry measurement. As described in the following, the non-resonance part of the background is subtracted by a fit to the invariant mass distributions. The contribution of non-exclusive background is estimated and is accounted for in the double-spin asymmetry measurement as a dilution factor. The experimental lepton-nucleon double-spin asymmetry $A_{||}^{VM}$ (Eq. 3.2.1) of exclusive diffractive vector-meson production is determined as

$$A_{||}^{VM} = \frac{1}{1-\gamma} \cdot \left(\frac{N^{\overleftarrow{\Rightarrow}} L^{\overrightarrow{\Rightarrow}} - N^{\overrightarrow{\Rightarrow}} L^{\overleftarrow{\Rightarrow}}}{N^{\overleftarrow{\Rightarrow}} L_p^{\overrightarrow{\Rightarrow}} + N^{\overrightarrow{\Rightarrow}} L_p^{\overleftarrow{\Rightarrow}}} - \gamma A_{||}^{ne} \right) . \tag{5.3.1}$$

In Eq. (5.3.1) $N^{\overleftarrow{\Rightarrow}}$ ($N^{\overrightarrow{\Rightarrow}}$) denotes the number of vector mesons produced in lepton-nucleon scattering with the beam spin oriented antiparallel (parallel) to the target spin. These numbers represent the amount of particles in the signal of the invariant mass distribution after subtraction of the non-resonant background events. The notation $A_{||}^{ne}$ stands for the asymmetry of the non-exclusive events and the factor γ represents the fraction of these events within the limit $\Delta E < 0.6$ GeV. In the following the details of the extraction of double-spin asymmetries for ρ^0- and ϕ-meson production are presented.

5.3.1 Spin Asymmetries in ρ^0-production

The double-spin asymmetries $A_{||}^{\rho}$ and A_1^{ρ} in exclusive diffractive production of ρ^0-mesons on proton and deuteron targets were measured in dependence on the kinematic variables Q^2, x, W and $-t'$.

The asymmetry of exclusive ρ^0-meson production on the proton target was studied in Refs. [82, 46]. This measurement did not account for the contribution of the asymmetry of exclusive non-resonant pion pair production. Data collected with the proton target were re-analyzed using improved[5] data sets (μDST productions 96c1 and 97c1). The most recent parameterization of the cross section ratio R^{ρ} was used.

[5]The data quality of the μDST production 97b2, used for the analysis [82], and the most recent μDST production 97c1 was compared. A wrong treatment of short tracks in the μDST 97b2 was found, resulting in a false track multiplicity determination in an event and therefore introducing a potential error source in the analysis of exclusive events.

Experimental Asymmetry $A_{||}^{\pi\pi}$ of Pion-Pair Production in the (ΔE, $M_{\pi\pi}$) – Plane
To estimate possible contributions from non-exclusive and non-resonant background events the double-spin asymmetry $A_{||}^{\pi\pi}$ of diffractive pion-pair production was measured. Four regions of interest in the (ΔE, $M_{\pi\pi}$)-plane were investigated:

- exclusive resonance region ($\Delta E < 0.6$ GeV, $0.6 < M_{\pi\pi} < 0.9$ GeV), containing primarily exclusive ρ^0 production,
- exclusive non-resonance region ($\Delta E < 0.6$ GeV, $M_{\pi\pi} > 1.2$ GeV or $M_{\pi\pi} < 0.3$ GeV), containing primarily exclusive pion pair production without forming an intermediate ρ^0-resonance,
- non-exclusive resonance region ($2.2 < \Delta E < 5$ GeV, $0.6 < M_{\pi\pi} < 0.9$ GeV), containing primarily resonance production in the process of target fragmentation etc.,
- non-exclusive non-resonance region ($2.2 < \Delta E < 5$ GeV, $M_{\pi\pi} > 1.2$ GeV or $M_{\pi\pi} < 0.3$ GeV), containing primarily non-resonant pion pair production in the DIS target fragmentation process.

The contribution of exclusive and non-exclusive events in the region $0.6 < \Delta E < 2.2$ GeV is unknown, therefore this region is excluded. Note that every type of events, dominating in a certain region, contributes as background in the other regions. The asymmetry $A_{||}^{\pi\pi}$ was measured in every region as

$$A_{||}^{\pi\pi} = \frac{N^{\overleftarrow{\Leftarrow}} L^{\overrightarrow{\Rightarrow}} - N^{\overrightarrow{\Rightarrow}} L^{\overleftarrow{\Leftarrow}}}{N^{\overleftarrow{\Leftarrow}} L_p^{\overrightarrow{\Rightarrow}} + N^{\overrightarrow{\Rightarrow}} L_p^{\overleftarrow{\Leftarrow}}} , \tag{5.3.2}$$

where $N^{\overleftarrow{\Leftarrow}}$ ($N^{\overrightarrow{\Rightarrow}}$) stands for the number of events per target and beam spin configuration in a certain region of the (ΔE, $M_{\pi\pi}$)-plane. The results are summarized in table 5.3.1. The

missing energy (GeV)	invariant mass (GeV)	asymmetry $A_{||}^{\pi\pi}$	
		^{1}H	^{2}H
$\Delta E < 0.6$	$0.6 < M_{\pi\pi} < 0.9$	0.11 ± 0.05	0.02 ± 0.03
$\Delta E < 0.6$	$M_{\pi\pi} > 1.2$ GeV, $M_{\pi\pi} < 0.3$	0.26 ± 0.11	0.12 ± 0.06
$2.2 < \Delta E < 5$	$0.6 < M_{\pi\pi} < 0.9$	0.00 ± 0.03	0.02 ± 0.02
$2.2 < \Delta E < 5$	$M_{\pi\pi} > 1.2$ GeV, $M_{\pi\pi} < 0.3$	-0.01 ± 0.04	0.02 ± 0.03

Table 5.3.1: Double-spin asymmetry $A_{||}^{\pi\pi}$in different regions of the $(\Delta E, M_{\pi\pi})$-plane.

measured double-spin asymmetry in the non-exclusive region is consistent with zero, while in the exclusive region it is significantly positive.

Non-exclusive and non-resonant background events can not be subtracted at the same time as they are not correlated. As it will be described in the following, the non-resonant background events were subtracted from the ρ^0-resonance sample in each spin state separately, and therefore the asymmetry of this type of background does not influence the measurement of the asymmetry of the resonance sample. The asymmetry of the non-exclusive events, although consistent with zero, dilutes the exclusive ρ^0 asymmetry of the remaining sample and is taken into account through a weighting "dilution" factor.

Treatment of Non-Resonant Background The non-resonant background events are subtracted from the analyzed sample through a fit to the invariant mass distribution, performed separately for each spin configuration of beam and target. Separately for each spin state the number of resonance ρ^0 events is determined by estimating the area under the peak in the invariant mass distribution, after the background subtraction.

The pion-pair invariant mass distribution is fitted with a relativistic p-wave Breit-Wigner function for a spin-1 object decaying into two spin-0 objects [93]:

$$\begin{aligned} \frac{d\sigma}{dM_{\pi\pi}} &\equiv BW(M_{\pi\pi}) = \frac{M_{\pi\pi} m_\rho \Gamma_\rho}{(M_{\pi\pi}^2 - m_\rho^2)^2 + m_\rho^2 \Gamma_\rho^2}, \\ \text{with} \quad \Gamma_\rho &= \Gamma_0 \left(\frac{\sqrt{M_{\pi\pi}^2 - 4m_\pi^2}}{\sqrt{m_\rho^2 - 4m_\pi^2}} \right)^3 \frac{m_\rho}{M_{\pi\pi}} \ . \end{aligned} \tag{5.3.3}$$

Here $M_{\pi\pi}$ is the invariant mass of the pion pair and Γ_0 stands for the natural width of the resonance. The skewing of the ρ^0-peak to lower mass values is taken into account by using the models of Ross-Stodolsky [94] and Söding [95].

In the Ross-Stodolsky model [94] for the ρ^0-photoproduction cross section the dissociative-diffractive production is described by Pomeron-like exchange in the t-channel, with only natural-parity exchanges being allowed. Exact SCHC and predominant imaginarity of the elastic ρ^0-amplitude are assumed. Non-diagonal transitions like $\gamma \to \rho'$, $\rho' + p \to \rho p$ are neglected. The mass of the state produced in dissociative diffraction is predicted to be shifted to lower masses by a factor $m_\rho^4 / M_{\pi\pi}^4$. This skewing effect is expected to be observable only in the case of wide resonances like the ρ^0-meson. In electroproduction of ρ^0-mesons, the mass-skewing factor is calculated in the form $m_\rho^4/(-t + M_{\pi\pi}^2)^2$, and expected to vanish at high $-t$ [94].

A parameterization based on this model,

$$\frac{d\sigma}{dM_{\pi\pi}} = BW(M_{\pi\pi}) \cdot \left(\frac{m_\rho}{M_{\pi\pi}} \right)^{n_{skew}} , \tag{5.3.4}$$

is used to describe the shape of the experimental pion-pair invariant mass distribution in the exclusive ρ^0 electroproduction sample, with n_{skew} denoting the skewing parameter. In the model [94] $n_{skew} = 4$ is predicted. The mass of the resonance m_ρ, its natural width Γ_0 and the skewing parameter are free parameters of the fit. An additional parameter was added to the function (5.3.4) to account for the flat non-resonant background.

In the Söding approach [95] the cross section of ρ^0-meson photoproduction is calculated considering the "Drell-type" process [96] in the framework of the one-pion exchange model, where the photon-proton interaction is assumed to proceed via an intermediate high-energy pion [97]. In this process a (virtual) pion is diffractively scattered off the proton, forming a non-resonant background for the ρ^0 production process. In Ref. [95] the skewing of the invariant mass distribution is related to the interference between the amplitudes of ρ^0-meson photoproduction and the Drell process, with an expected mass shift of 25 MeV. The sign of the shift is not predicted, but expected to depend in particular on the sign of the $\rho\pi\pi$ coupling constant.

The amplitudes of the two processes were added coherently as in Ref. [98]:

$$\begin{aligned}\frac{d\sigma}{dM_{\pi\pi}} &= \left| A_{res}\frac{\sqrt{M_{\pi\pi}m_\rho\Gamma_\rho}}{M_{\pi\pi}^2 - m_\rho^2 + im_\rho\Gamma_\rho} + A_{nr}\right|^2, \\ &= A_{res}^2\frac{M_{\pi\pi}m_\rho\Gamma_\rho}{(M_{\pi\pi}^2 - m_\rho^2)^2 + m_\rho^2\Gamma_\rho} \\ &+2A_{res}A_{nr}\frac{\sqrt{M_{\pi\pi}m_\rho\Gamma_\rho}(M_{\pi\pi}^2 - m_\rho^2)}{(M_{\pi\pi}^2 - m_\rho^2)^2 + m_\rho^2\Gamma_\rho^2} + A_{nr}^2 \ .\end{aligned} \tag{5.3.5}$$

Here A_{nr} and A_{res} denote the non-resonant and resonant amplitudes, respectively. A_{res} is taken to be real.

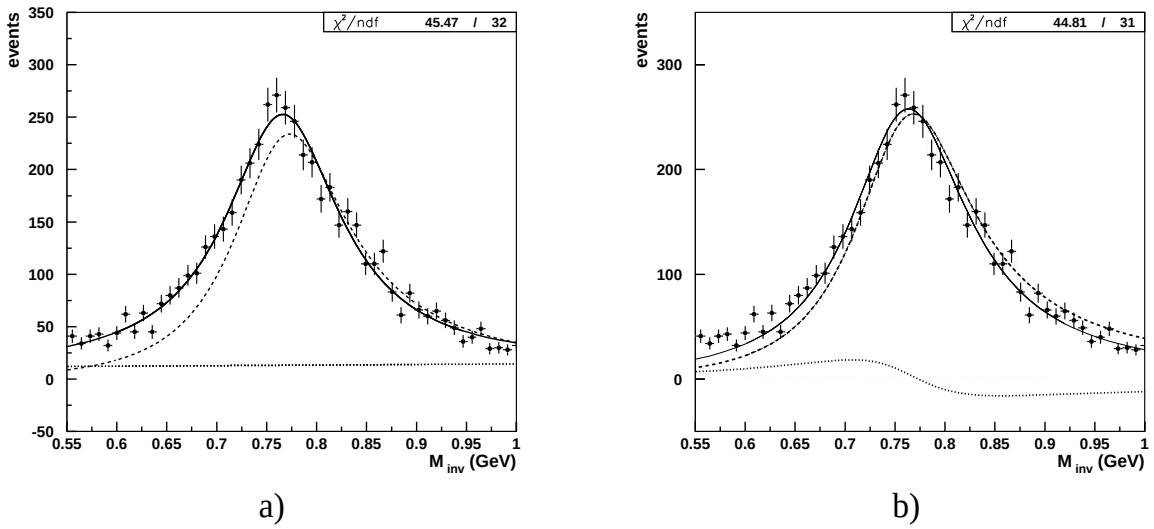

Figure 5.3.1: The invariant mass distribution for exclusive diffractive ρ^0-production on a deuteron target, fitted with the Breit-Wigner shape using the mass skewing models of a) Ross-Stodolsky and b) Söding. Dashed lines indicate the stand-alone Breit-Wigner shape, dotted lines represent a) flat background, b) interference term.

Fit function	m_ρ (GeV)	Γ_0 (GeV)	χ^2/ndf	A_{nr}/A_{res}	n_{skew}
Söding	0.773 ± 0.006	0.152 ± 0.009	45/31	0.26 ± 0.05	–
Ross & Stodolsky	0.778 ± 0.002	0.149 ± 0.011	46/32	–	2.2 ± 0.5

Table 5.3.2: The fitted values of the free parameters of the pion-pair invariant mass distribution

The results of the fits to the data using the functions (5.3.4) and (5.3.5) are shown in fig. 5.3.1 and the fit parameters are listed in table 5.3.2. The numbers of ρ^0-mesons are obtained in both cases by counting the events under the Breit-Wigner function after background subtraction.

Both fit functions describe the invariant mass shape equally well and the fitted parameters m_ρ, Γ_0 agree with PDG values [1]. Although the choice of the fit function does not influence

the asymmetry value (cf. systematic studies below), the Söding parameterization is chosen for the further analysis, as the Ross-Stodolsky model is based on the too strict assumptions of exact SCHC and natural-parity exchange. The fraction of the non-resonant background in the sample, determined as the ratio of the number of background events to the total number of events in the sample, is on the order of 3% for both proton and deuteron targets.

Treatment of Non-Exclusive Background The non-exclusive background appears at non-zero values of missing energy (fig. 5.1.2). It is formed mostly by events, where the final state contains a product of the DIS fragmentation process, e.g. a hadron pair, a vector meson or other particles, decaying into them. Given the limited detector resolution, a certain amount of such events appear under the exclusivity peak in the missing energy distribution, if the recoiling proton is undetected. Hence in the region of the exclusive peak it is impossible to separate the non-exclusive background from the exclusive events on an event-by-event basis.

The asymmetry $A_{||}^{ne}$of the non-exclusive background, measured in the invariant mass range $0.6 < M_{\pi\pi} < 0.9$ GeV and missing energy region $2.1 < \Delta E < 5$ GeV, is found to be consistent with zero for both hydrogen and deuterium targets. The values of the asymmetry for every year of data production and certain combinations of them, representing running with the same target, are shown in fig. 5.3.2.

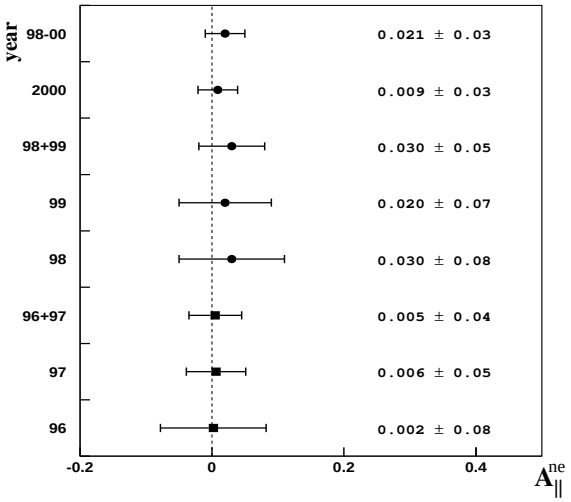

Figure 5.3.2: The double-spin asymmetry $A_{||}^{ne}$ of non-exclusive background events for different data taking periods and certain combination of them, representing running with the same target. The filled circles indicate data collected with the deuteron target, the squares represent data collected with the proton target. The values of the asymmetries are shown together with their statistical errors.

If the fraction of non-exclusive events is significant, the asymmetry of these events, $A_{||}^{ne}$, can influence the measurement of the double-spin asymmetry $A_{||}^{\rho}$ of the exclusive sample, even if $A_{||}^{ne}$ is consistent with zero. Therefore it has to be taken as a dilution factor while calculating the final value of $A_{||}^{\rho}$. The dilution factor δ^{ne} is defined as $\delta^{ne} = A_{||}^{ne} \cdot \gamma$. The fraction γ of non-exclusive events in the exclusivity region $\Delta E < 0.6$ GeV was estimated using two methods, as will be described in the following.

The first method to determine the fraction of non-exclusive events in the exclusive ρ^0-sample, referred to as "fit" method, is based on a fit of an empirical function to the missing energy spectra. Gaussian and Landau distributions were used to describe the exclusive peak in the ΔE spectrum. The fit with the Landau function appeared to be unstable under the variation of e.g. the bin width of the fitted spectrum, therefore the Gaussian distribution was preferred.

Higher order polynomials and exponential functions were used as background models, giving similar values of the fraction γ. The best values of χ^2/ndf were obtained using the function

$$f(\Delta E) = a_0 \cdot (\Delta E - a_1) \cdot e^{-a_2\sqrt{\Delta E - a_1}} \ . \tag{5.3.6}$$

The data before and after the non-exclusive background subtraction are shown in fig. 5.3.3. The parameters of the Gaussian fit to the peak and the estimated fraction γ of non-exclusive

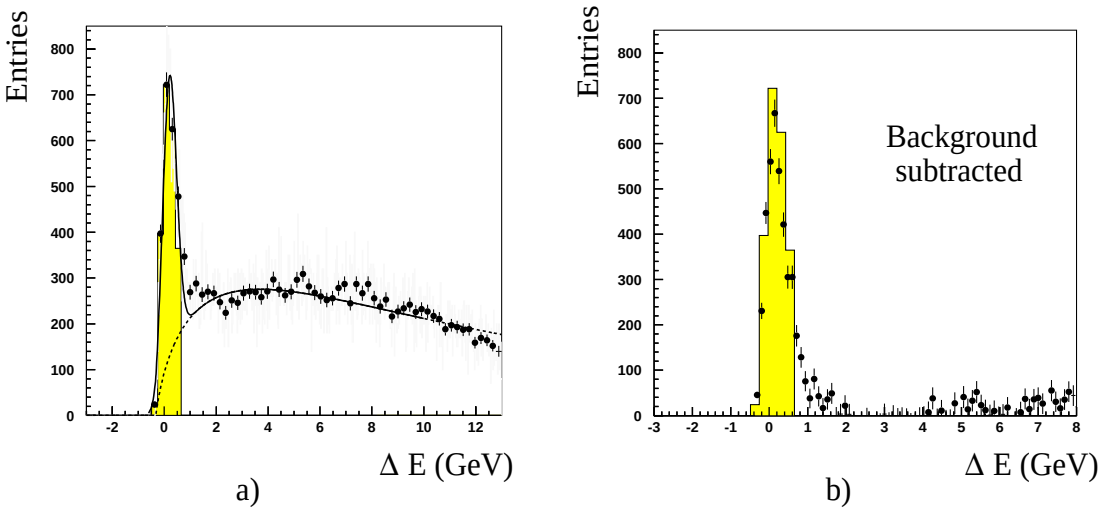

Figure 5.3.3: Subtraction of non-exclusive background by a fit (solid line) to the ΔE distribution a). The exclusive peak is described by a Gaussian, the background by the function (5.3.6), the latter represented by the dashed line. Panel b) represents the ΔE distribution after the background subtraction. Data obtained with the proton target are shown. The shaded areas indicate the exclusive region.

events for both proton and deuteron targets are listed in the table 5.3.3.

N	Gaussian $<\Delta E>$ (GeV)	Gaussian $\sigma\Delta E$ (GeV)	χ^2/ndf	γ
^{1}H	0.23 ± 0.01	0.27 ± 0.02	118/85	0.130 ± 0.011
^{2}H	0.27 ± 0.07	0.35 ± 0.02	167/88	0.150 ± 0.007

Table 5.3.3: The fitted parameters of the missing energy distribution.

The fraction γ was estimated in each kinematic bin separately (cf. discussion below), integrated over the spin state. The value of γ varies for different kinematic bins between 0.08 ± 0.09 and 0.17 ± 0.12 independent of the target gas.

Another method to subtract the DIS background and to determine the fraction γ, referred to as "normalization" method, makes use of the non-diffractive character of the DIS fragmentation process that dominates at higher values of $-t'$. Therefore the DIS background under the ΔE distribution can be determined using events with $-t' > 0.8$ GeV^2. The missing energy distribution of events with high $-t'$ was normalized to that with $-t' < 0.4$ GeV^2 (cf. fig. 5.3.4) in the region of $\Delta E > 3$ GeV, where the DIS events are expected to dominate. These normalized data are then subtracted from the ΔE distribution in the region of low $-t'$. The tail of the non-exclusive background under the exclusivity peak in the ΔE distribution

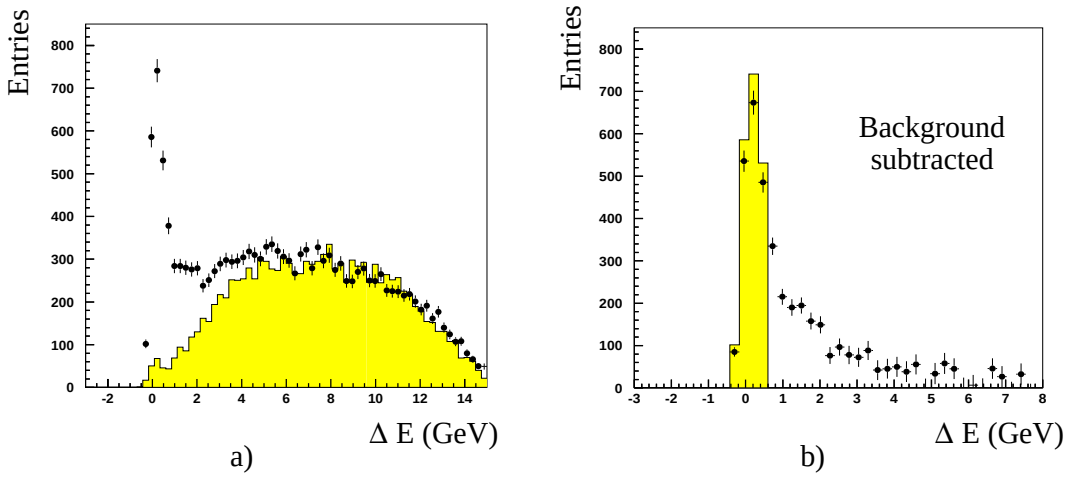

Figure 5.3.4: Panel a) represents the ΔE distribution at high $-t' > 0.8$ GeV^2 (shaded histogram), normalized to that at low $-t'$ values. Panel b) shows the ΔE distribution after the background subtraction, shaded area indicates the exclusive region. Data obtained with the proton target are shown.

looks similar to that obtained with the fit method. However, in the region $0.6 < \Delta E < 3$ GeV the assumed background shape does not match the data as good as it does in the case of the fit method.

The values of the fraction γ, obtained with the normalization method of non-resonant background subtraction to be γ =0.139 $\pm$ 0.011 and γ =0.145 $\pm$ 0.007 for proton and deuteron, respectively, are compatible with the values obtained using the fit method. Note that the shape of the ΔE spectra varies slightly with $-t'$, as also with other kinematic variables, although the normalization method of non-exclusive background subtraction assumes independence of the spectrum on $-t'$.

Asymmetry $A_{||}^{\rho}$ of the Lepton-Nucleon Interaction The double-spin asymmetry of exclusive ρ^0 electroproduction was determined as (cf. Eq. (5.3.1)):

$$A_{||}^{\rho} = \frac{1}{1-\gamma}\left(A_{||}^{meas} - \gamma A_{||}^{ne}\right), \quad A_{||}^{meas} = \frac{N^{\overrightarrow{\Leftarrow}} L^{\overrightarrow{\Rightarrow}} - N^{\overrightarrow{\Rightarrow}} L^{\overrightarrow{\Leftarrow}}}{N^{\overrightarrow{\Leftarrow}} L_p^{\overrightarrow{\Rightarrow}} + N^{\overrightarrow{\Rightarrow}} L_p^{\overrightarrow{\Leftarrow}}} \; . \tag{5.3.7}$$

Here $N^{\overrightarrow{\Leftarrow}}$ and ($N^{\overrightarrow{\Rightarrow}}$) stands for the number of ρ^0-mesons, produced when the spin of the beam is parallel (antiparallel) to the spin of the target nucleon, after the non-resonant background

subtraction. The fraction and the asymmetry of the non-exclusive events are denoted by γ and $A_{||}^{ne}$, respectively. The measured asymmetry, averaged over the kinematics in the HERMES acceptance[6], is shown in fig.5.3.5 separately for every year of data taking and certain combinations of them, representing running with the same target. The statistical

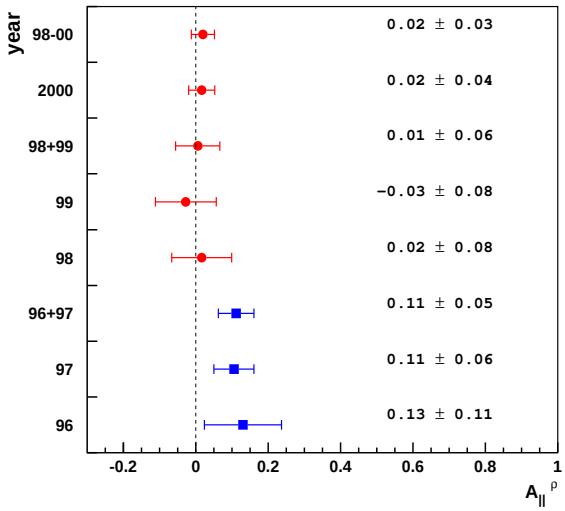

Figure 5.3.5: The double-spin asymmetry $A_{||}^{\rho}$ of exclusive ρ^0 electroproduction for different data taking periods and certain combination of them, representing running with the same target. The filled circles indicate data collected with the deuteron target, the squares represent data collected with the proton target. The values of the asymmetries are shown together with their total uncertainties which are obtained by adding statistical and systematic uncertainties in quadrature.

uncertainties of the measured asymmetries $A_{||}^{ne}$, $A_{||}^{meas}$ and of the fraction γ are propagated into the statistical uncertainty of the asymmetry $A_{||}^{\rho}$.

No systematic change of the asymmetry value is observed when different methods of background subtraction are used. Therefore only the systematic uncertainties from the measurements of beam and target polarization are assigned as experimental systematic uncertainties to the asymmetry measurement. The systematic uncertainties of the target polarization were 6.3%, 4.4% in 1996 and 1997, 8% in 1998-1999 and 4% in 2000, respectively. The systematic uncertainty of the beam polarization was 3.4 % in 1996-1998 and 1.6% in 1999-2000. The resulting systematic uncertainties for the combined hydrogen and deuterium data samples are 6% and 5.4%, respectively, and are negligible in comparison to statistical uncertainties.

The values of the asymmetry $A_{||}^{\rho}$ obtained from the data of different years are consistent. In the following the data collected in different years with a certain target are combined. The measured lepton-nucleon asymmetry $A_{||}^{\rho}$, averaged over all kinematic variables within the HERMES acceptance is $A_{||}^{\rho} = 0.11 \pm 0.05$ on the proton target, and $A_{||}^{\rho} = 0.02 \pm 0.03$ on the deuteron target. The total uncertainty is obtained by adding statistical and systematic uncertainties in quadrature and is dominated by the statistical uncertainty. The slightly positive asymmetry $A_{||}^{\rho}$ obtained with the proton target is in very good agreement[7] with Refs. [46, 82].

[6]The acceptance corrections and radiative corrections are discussed in Appendices 3 and 4, respectively.

[7]The asymmetry measured on the proton target is compared in detail with the analysis [82] in the Appendix 2.

The dependence of $A_{||}^{\rho}$ on the kinematic variables Q^2, x, W^2 and $-t'$ was investigated. For every variable, the exclusive ρ^0-sample was divided into several kinematic bins with approximately equal statistics. The subtraction of the non-resonant background was performed in every bin for both spin configurations of beam and target separately, as to exclude a possible asymmetry in this subsamples. Marginal statistics of non-exclusive events in the sample results in large statistical uncertainties of the asymmetry $A_{||}^{ne}$ which propagate into the uncertainties of the asymmetry $A_{||}^{\rho}$. To decrease these uncertainties the kinematically averaged asymmetries of non-exclusive events $A_{||}^{ne}$ are taken instead for every bin. The dependence of the resulting asymmetry $A_{||}^{\rho}$ on different kinematic variables is shown in fig. 5.3.6.

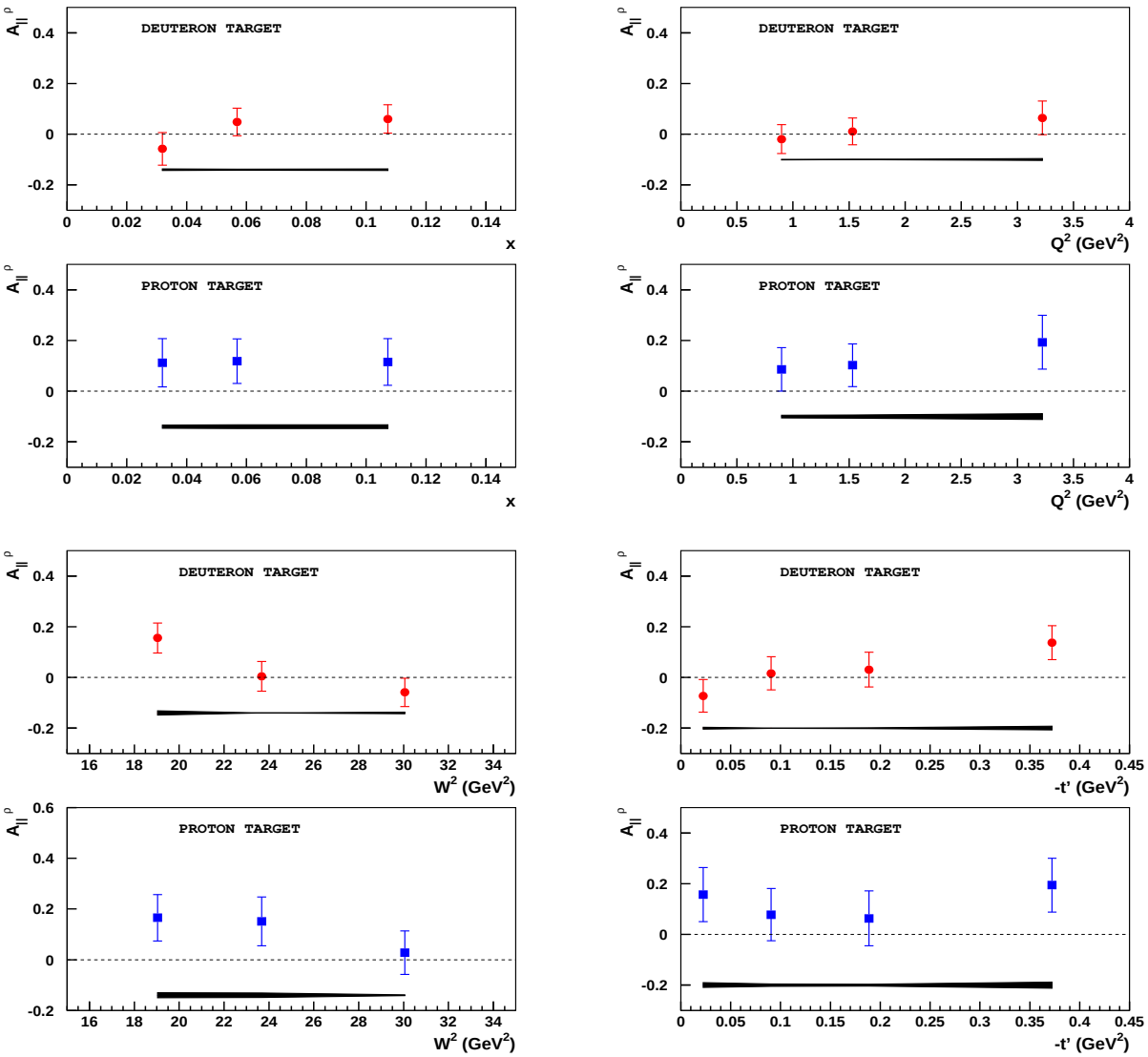

Figure 5.3.6: Dependence of the double-spin asymmetry $A_{||}^{\rho}$ of exclusive diffractive ρ^0-electroproduction on the kinematic variables x (top left), Q^2 (top right), W^2 (bottom left) and $-t'$ (bottom right). Filled circles represent the data collected with the deuteron target, squares show the data with the proton target. Error bars represent the statistical uncertainties, the systematic uncertainties are indicated by dark bands.

No significant dependence of the asymmetry $A_{||}^{\rho}$, measured with the proton target, is observed in any kinematic variable. The deuteron asymmetry $A_{||}^{\rho}$, however, shows a slight increase with x and $-t'$. It is assumed here that the decrease of $A_{||}^{\rho}$ with W^2 is intrinsically included in its behavior over x, because of the correlation between these kinematic variables. For further discussion see section 5.5.

Photon-Absorption Asymmetry The photon-absorption asymmetry A_1^{ρ} of exclusive diffractive ρ^0-electroproduction was calculated using the measured lepton-nucleon asymmetry $A_{||}^{\rho}$ (cf. Eq. (3.2.2)) as

$$A_1^{\rho} = \frac{A_{||}^{\rho}}{D^{\rho}} - \eta\sqrt{R^{\rho}} \; , \tag{5.3.8}$$

where $\sqrt{R^{\rho}}$ represents the contribution from the interference asymmetry A_2^{ρ}. The parameterization (2.3.19) from Ref. [33] was used for the determination of the cross section ratio R^{ρ}. The uncertainties on the values of asymmetry $A_{||}^{\rho}$, cross section ratio R^{ρ} and effective polarization parameter D^{ρ} are propagated into the uncertainties of the asymmetry A_1^{ρ}. A slightly positive photon-absorption asymmetry $A_1^{\rho} = 0.24 \pm 0.15$ is obtained with the proton target. With the deuteron target the asymmetry $A_1^{\rho} = -0.05 \pm 0.09$ is measured.

bin boundaries	bin center	$A_{\|\|}^{\rho}$		A_1^{ρ}	
		^{1}H	^{2}H	^{1}H	^{2}H
$x < 0.043$	0.032	0.11 ± 0.09	-0.06 ± 0.06	0.21 ± 0.20	-0.15 ± 0.14
$0.043 < x < 0.073$	0.057	0.12 ± 0.08	0.04 ± 0.05	0.29 ± 0.27	0.08 ± 0.16
$0.073 < x$	0.110	0.12 ± 0.09	0.06 ± 0.06	0.31 ± 0.35	0.12 ± 0.20
$Q^2 < 1.15$	0.89 GeV^2	0.09 ± 0.09	-0.02 ± 0.06	0.17 ± 0.20	-0.09 ± 0.14
$1.15 < Q^2 < 2.05$	1.53 GeV^2	0.10 ± 0.08	0.01 ± 0.05	0.24 ± 0.26	-0.03 ± 0.16
$2.05 < Q^2$	3.22 GeV^2	0.19 ± 0.10	0.06 ± 0.07	0.53 ± 0.37	0.11 ± 0.20
$W^2 < 21.5$	19.04 GeV^2	0.16 ± 0.09	0.16 ± 0.06	0.57 ± 0.40	0.53 ± 0.26
$21.5 < W^2 < 26.0$	23.68 GeV^2	0.15 ± 0.10	0.00 ± 0.06	0.39 ± 0.30	-0.05 ± 0.17
$26.0 < W^2$	30.05 GeV^2	0.03 ± 0.08	-0.06 ± 0.06	0.02 ± 0.18	-0.16 ± 0.12
$-t' < 0.04$	0.023 GeV^2	0.16 ± 0.11	-0.07 ± 0.06	0.37 ± 0.30	-0.27 ± 0.19
$0.04 < -t' < 0.10$	0.091 GeV^2	0.08 ± 0.10	0.02 ± 0.07	0.16 ± 0.30	-0.02 ± 0.19
$0.10 < -t' < 0.19$	0.189 GeV^2	0.06 ± 0.11	0.03 ± 0.07	0.11 ± 0.31	0.02 ± 0.20
$0.19 < -t'$	0.372 GeV^2	0.19 ± 0.11	0.14 ± 0.07	0.47 ± 0.31	0.32 ± 0.20

Table 5.3.4: Measured values of lepton-nucleon asymmetry $A_{||}^{\rho}$ and photon-absorption asymmetry A_1^{ρ} in the cross section of exclusive diffractive ρ^0-electroproduction, shown for bins in a certain kinematic variable while averaging over the other three variables. Only statistical uncertainties are given.

In fig. 5.3.7 the dependence of A_1^{ρ} on the kinematic variables x, Q^2, W^2 and $-t'$, respectively, is shown obtained by averaging over the other three variables. The measured values of the lepton-nucleon asymmetry $A_{||}^{\rho}$ and of the photon-absorption asymmetry A_1^{ρ} in

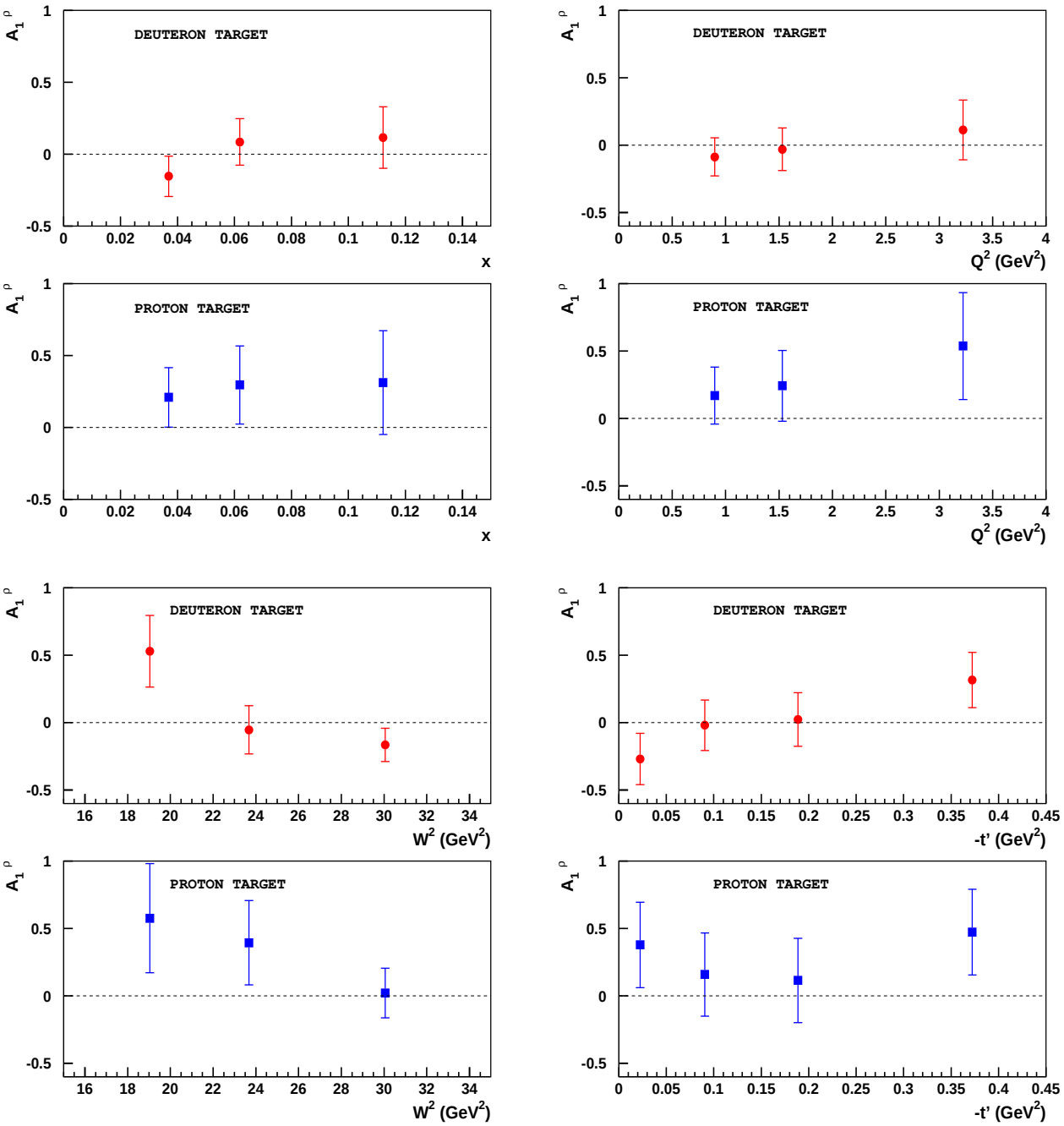

Figure 5.3.7: Dependence of the photon-absorption asymmetry A_1^ρ in exclusive diffractive ρ^0-electroproduction on the kinematic variables x (top left), Q^2 (top right), W^2 (bottom left) and $-t'$ (bottom right), obtained by averaging over the other three variables. Filled circles represent the data collected with the deuteron target, squares show the data with the proton target. The error bars represent the total uncertainty, with statistical and systematic uncertainties added in quadrature.

each kinematic bin are listed in table 5.3.4. The comparison of the results with theoretical predictions and possible interpretations of the asymmetries are discussed in section 5.5.

5.3.2 Spin Asymmetries in ϕ-production

The double-spin asymmetry in the cross section of ϕ-meson electroproduction was measured in a way similar to that of ρ^0-meson production. As in the case of ρ^0-meson production there are several sources of background, contaminating the sample of exclusively diffractively produced ϕ-mesons:

- events originating from the DIS fragmentation process,
- non-resonant kaon-pair production,
- pion-pair production, contaminating the kaon-pair sample (relevant for data collected before the RICH was installed),
- double-dissociative diffractive ϕ-meson production,
- $s\bar{s}$-knockout from the nucleus.

The last two types of background are not studied in the asymmetry analysis. The events corresponding to double-dissociative diffraction are not subtracted from the sample, as in the case of ρ^0-production. The events originating from ϕ-meson production by the $s\bar{s}$-knockout process are estimated to have an at least 10 times lower rate than those from diffractive ϕ-production [99] and are not subtracted, as well.

As in the case of ρ^0-meson production, the measurement of the double-spin asymmetry $A_{||}^{\phi}$ could possibly be diluted by the asymmetries in non-exclusive DIS fragmentation and non-resonant hadron pair production. Therefore the hadron-pair asymmetry $A_{||}^{hh}$ is measured in the two regions of missing energy and hadron-pair invariant mass. The results are listed in table 5.3.5. The treatment of the background events is discussed in the following.

missing energy (GeV)	invariant mass (GeV)	asymmetry $A_{||}^{hh}$	
		^{1}H	^{2}H
$\Delta E < 1.0$	$M_{hh} > 1.04$	0.16 ± 0.05	0.05 ± 0.15
$1.0 < \Delta E < 4.0$	$1.01 < M_{\pi\pi} < 1.026$	0.03 ± 0.10	0.05 ± 0.12

Table 5.3.5: Asymmetry $A_{||}^{hh}$ of hadron pair production on proton and deuteron targets.

Treatment of Non-resonant Background As in the case of ρ^0-meson production, the non-resonant background is subtracted from the sample of exclusive ϕ-mesons by a fit to the invariant mass distribution of the two hadrons, under the assumption that they are kaons. The fit to the data is shown in fig. 5.3.8 with the fit parameters being listed in table 5.3.6. The natural width of the ϕ-resonance is 4.4 MeV [1] and its shape is in principle described by the p-wave Breit-Wigner function. As described in section 5.2, since the resolution of the HERMES detector is limited, the Breit-Wigner shape of the invariant mass distribution is smeared to a Gaussian. The background is described by an empirical function:

$$f(M_{KK}) = A \cdot (M_{KK} - M_{KK}^{min}) \cdot e^{B \cdot \sqrt{M_{KK} - M_{KK}^{min}}} , \tag{5.3.9}$$

where A and B are free parameters, M_{KK} stands for the kaon-pair invariant mass and M_{KK}^{min} denotes the threshold of the kaon-pair invariant mass distribution, corresponding to the turn-on of the kaon-pair phase space. The slight difference in the widths of the invariant mass

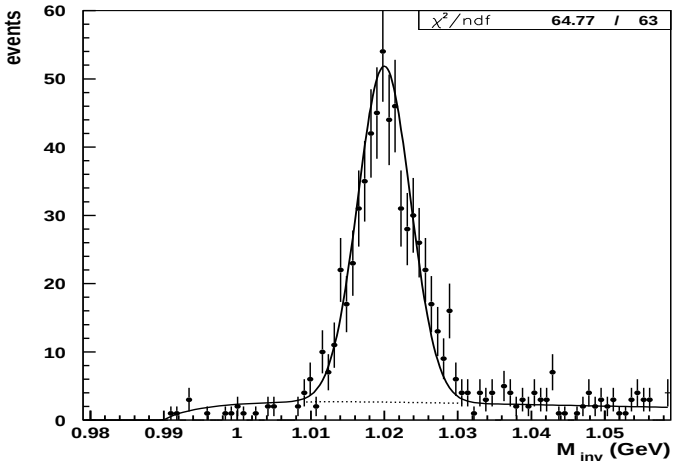

Figure 5.3.8: Fit to the invariant mass distribution of two hadrons assuming these are kaons. Data collected with the deuteron target are shown.

N	M_ϕ (MeV)	Gaussian σ (MeV)	threshold M_{KK}^{min}	χ^2/ndf	Signal/Background
^{1}H	1019.5 ± 0.7	3.4 ± 0.1	0.989 ± 0.009	63/59	2.7
^{2}H	1020.0 ± 0.1	3.6 ± 0.1	0.989 ± 0.005	65/63	8.0

Table 5.3.6: The fitted values for the free parameters of the kaon-pair invariant mass distribution.

distribution between proton and deuteron data is introduced by the difference in the detector resolution between 1996-1997 and 1998-2000 after the RICH installation (cf. section 5.1.2). The use of the RICH kaon identification leads to an improvement of the signal-to-background ratio under the peak of the invariant mass distribution by a factor of 3.

Treatment of Non-exclusive Background The fraction γ of the non-exclusive background events corresponding to DIS fragmentation is estimated by normalization of the ΔE spectra in the ϕ-meson mass window in two regions of the $-t'$ distribution ($-t' < 0.6$ GeV^2 and $-t' > 0.8$ GeV^2), similarly to the case of ρ^0-meson production. This method of non-exclusive background subtraction is illustrated in fig. 5.3.9. For the fraction a value of $\gamma = 0.09 \pm 0.02$ was obtained. Complementary, a DIS background subtraction using a Monte-Carlo simulation [34] gave a non-exclusive background fraction of $\gamma = 0.09$, in good agreement with the measured value. Unlike the case of ρ^0-meson production, the shape of the ϕ-meson ΔE distribution could not be fitted by any empirical function providing a good χ^2.

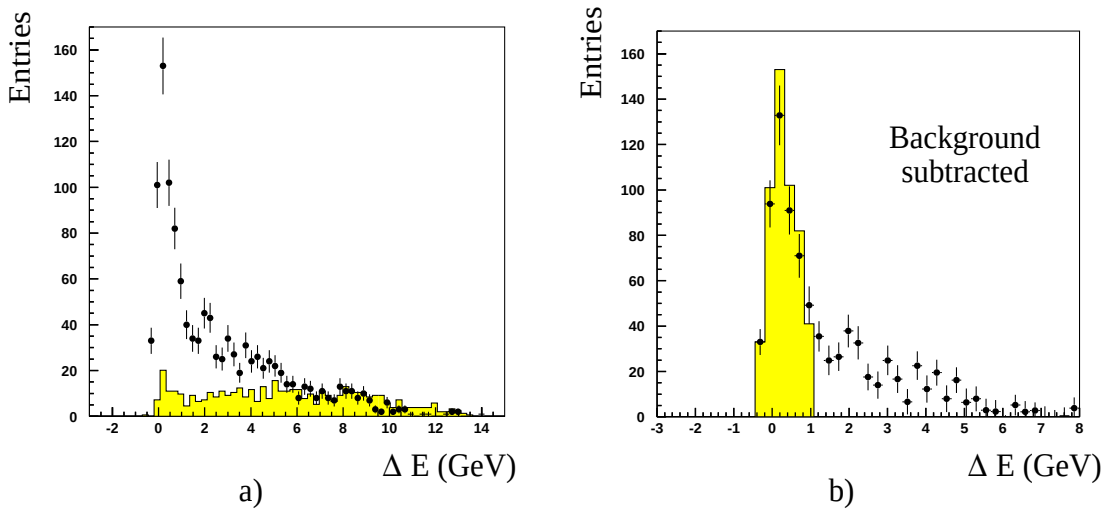

Figure 5.3.9: a) ΔE distribution at high $-t' > 0.8$ GeV^2 (shaded histogram), normalized in the large ΔE region to that at low $-t'$ values (data points). Panel b) shows the ΔE distribution after the background subtraction. The exclusive area is shaded. Data obtained with the deuteron target are shown.

Lepton-Nucleon Asymmetry As in the case of ρ^0-production the double-spin asymmetry in the cross section of ϕ-production can be determined as

$$A_{||}^{\phi} = \frac{1}{1-\gamma}\left(A_{||}^{meas} - \gamma A_{||}^{ne}\right), \qquad A_{||}^{meas} = \frac{N^{\vec{\Leftarrow}}L^{\vec{\Rightarrow}} - N^{\vec{\Rightarrow}}L^{\vec{\Leftarrow}}}{N^{\vec{\Leftarrow}}L_p^{\vec{\Rightarrow}} + N^{\vec{\Rightarrow}}L_p^{\vec{\Leftarrow}}}\,, \tag{5.3.10}$$

where $N^{\vec{\Leftarrow}}$ ($N^{\vec{\Rightarrow}}$) denotes the number of ϕ-mesons produced when the spin of the beam is oriented parallel (antiparallel) to the spin of the target nucleon. The double-spin asymmetry $A_{||}^{\phi}$ is calculated with the contribution from an asymmetry of non-exclusive events taken into account according to Eq. (5.3.10), and without it. The results appear to be the same, therefore the contribution from $A_{||}^{ne}$ is neglected in the following. The values for the lepton-nucleon asymmetries of exclusive diffractive ϕ-meson electroproduction for proton and deuteron targets are listed in table 5.3.7. Because of marginal statistics the dependence of the asymmetry $A_{||}^{\phi}$ on kinematic variables could not be measured.

Photon-Absorption Asymmetry The photon-absorption asymmetry A_1^{ϕ} was calculated for exclusive ϕ-meson production as

$$A_1^{\phi} = \frac{A_{||}^{\phi}}{D} - \eta\sqrt{R^{\phi}}\,, \tag{5.3.11}$$

where $\sqrt{R^{\phi}}$ represents the contribution from the asymmetry A_2^{ϕ}. The parameterization of the cross section ratio R^{ϕ} was discussed in section 2.3.5. As in the case of the ρ^0-meson production, the statistical uncertainty of the R^{ϕ}-parameterization propagates into the uncertainty of the measured asymmetry A_1^{ϕ}. In order to decrease this uncertainty, the parameterization (2.3.19) was taken for determination of the ratio R^{ϕ} instead of (2.3.20), (cf. discussion in

section 2.3.5). The values of the double-spin asymmetry A_1^ϕ measured with the proton and deuteron targets are listed in table 5.3.7. As in the case of the ρ^0-meson only systematic uncertainties of the determination of beam and target polarization contribute to the systematic uncertainty of the asymmetry measurement.

N	$< W^2 >$, GeV^2	$< Q^2 >$, GeV^2	$< x >$	$A_{\|\|}^\phi$	A_1^ϕ
^{1}H	21	2.1	0.098	0.1 ± 0.2	0.2 ± 0.5
^{2}H	22	1.8	0.082	0.1 ± 0.1	0.1 ± 0.3

Table 5.3.7: Values for the lepton-nucleon asymmetry $A_{||}^\phi$ and photon-absorption asymmetry A_1^ϕ in the cross section of exclusive diffractive ϕ-meson electroproduction, integrated over all kinematic variables within the HERMES acceptance. The total uncertainty is obtained by adding the statistical and systematic uncertainties in quadrature.

5.4 Quasi-Real Photoproduction of Vector Mesons

As discussed above, the events corresponding to quasi-real photoproduction of ρ^0- and ϕ-mesons are required to contain only two oppositely charged hadrons of the specific type. Since the kinematics of these events can not be fully reconstructed, the fraction of non-exclusively produced vector mesons can not be calculated. The non-resonant background, however, can be subtracted as in the case of exclusive vector-meson production by a fit to the invariant mass distribution of the two hadrons, assuming they are pions or kaons, respectively.

5.4.1 Spin Asymmetries in ρ^0-production

The lepton-nucleon double-spin asymmetry $A_{||}^\rho$ in the cross section of quasi-real photoproduction of ρ^0-mesons produced on a polarized proton or deuteron target is obtained as

$$A_{||}^\rho = \frac{N^{\vec{\Leftarrow}} L^{\vec{\Rightarrow}} - N^{\vec{\Rightarrow}} L^{\vec{\Leftarrow}}}{N^{\vec{\Leftarrow}} L_p^{\vec{\Rightarrow}} + N^{\vec{\Rightarrow}} L_p^{\vec{\Leftarrow}}} \ , \tag{5.4.1}$$

where $N^{\vec{\Leftarrow}}$ ($N^{\vec{\Rightarrow}}$) denote the number of ρ^0-mesons, produced when the spin of the beam is oriented antiparallel (parallel) to that of the target, after subtraction of the non-resonant background. The invariant mass of the pion-pair is fitted as in the case of exclusive ρ^0-meson production. The fitted parameters are listed in table 5.4.1. In fig. 5.4.1 the double-spin asymmetry $A_{||}^\rho$ is shown, as obtained after integration over all kinematic variables within the HERMES acceptance. The average values of Q^2 and x for quasi-real photoproduction of ρ^0-mesons are estimated using the Monte-Carlo simulation for proton target, as discussed in section 5.2. Using these average values the cross-section ratio R^ρ and the effective polarization factor D^ρ are calculated. The photon-absorption asymmetry A_1^ρ for the quasi-real

Parameterization	M_ρ (GeV)	Γ_0 (GeV)	χ^2/ndf	A_{nr}/A_{res}	n_{skew}
Söding	0.770 ± 0.002	0.160 ± 0.003	110/53	0.24 ± 0.002	–
Ross & Stodolsky	0.770 ± 0.001	0.139 ± 0.002	98/49	–	2.8 ± 0.1

Table 5.4.1: Fitted values of the free parameters of the 2-pion invariant mass distribution.

photoproduction of ρ^0-mesons is extracted as in the case of exclusive ρ^0 production. The values of the lepton-nucleon asymmetry $A_{||}^\rho$ and the photon absorption asymmetry A_1^ρ are listed in table 5.4.2. Systematic uncertainties are introduced only by the measurements of beam and target polarization.

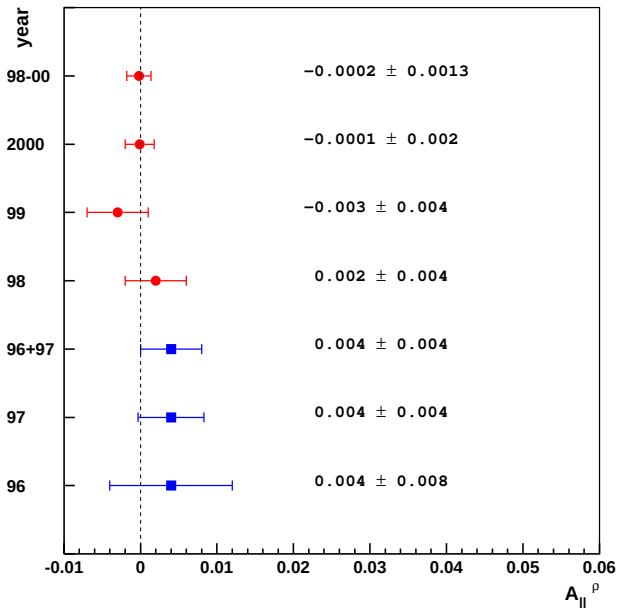

Figure 5.4.1: Double-spin asymmetry $A_{||}^\rho$ of quasi-real photoproduction of ρ^0-mesons for every year of data taking and certain combination of them, representing running with the same target. The filled circles indicate data collected with the deuteron target, the squares represent the data collected with the proton target. The values of the asymmetries are shown together with their total uncertainties which are obtained by adding statistical and systematic uncertainties in quadrature.

N	$< Q^2 >$, GeV^2	$< x >$	$A_{||}^\rho$	A_1^ρ
^{1}H	0.12	0.0038	0.004 ± 0.004	0.015 ± 0.017
^{2}H	0.12	0.0038	-0.0002 ± 0.0013	-0.004 ± 0.006

Table 5.4.2: Values for the lepton-nucleon asymmetry $A_{||}^\rho$ and the photon-absorption asymmetry A_1^ρ in the cross section of quasi-real photoproduction of ρ^0-mesons. The total uncertainty is obtained by adding the statistical and systematic uncertainties in quadrature.

5.4.2 Spin Asymmetries in ϕ-production

The double-spin asymmetries $A_{||}^{\phi}$ and A_1^{ϕ} in the cross section of quasi-real photoproduction of ϕ-mesons were obtained similarly to those in the case of ρ^0-meson production. The non-resonant background was subtracted from the sample by a fit to the invariant mass distribution as in the case of exclusive ϕ-meson production. The fitted parameters are listed in table 5.4.3. The obtained lepton-nucleon asymmetries for every year of data taking are shown in fig. 5.4.2. The photon-absorption asymmetry A_1^{ϕ} is calculated using R^{ϕ} and D^{ϕ}, calculated at average values of Q^2 and x, obtained by Monte-Carlo simulation, as in the case of ρ^0-mesons. The values of the asymmetries are given in table 5.4.4.

N	M_{ϕ} (MeV)	Gaussian σ (MeV)	threshold M_{KK}^{min}	χ^2/ndf	Signal/Background
^{1}H	1019.9 $\pm$ 0.6	3.4 $\pm$ 0.3	0.987 $\pm$ 0.001	107/83	2.4
^{2}H	1019.8 $\pm$ 0.3	3.7 $\pm$ 0.1	0.987 $\pm$ 0.005	142/84	3.0

Table 5.4.3: Fitted values for the free parameters of the kaon-pair invariant mass distribution.

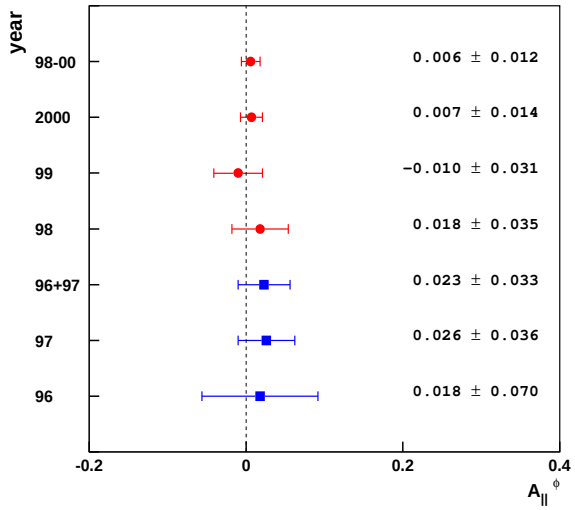

Figure 5.4.2: Double-spin asymmetry $A_{||}^{\phi}$ of quasi-real photoproduction of ϕ-mesons for every year of data taking and certain combinations of them, corresponding to running with the same target. The filled circles indicate data collected with the deuteron target, the squares represent the data collected with the proton target. The values of the asymmetry are shown with their total errors which are obtained by adding statistical and systematic uncertainties in quadrature.

N	$< Q^2 >$ GeV^2	$< x >$	$A_{||}^{\phi}$	A_1^{ϕ}
^{1}H	0.12	0.005	0.023 ± 0.033	0.07 ± 0.11
^{2}H	0.12	0.005	0.006 ± 0.012	0.02 ± 0.04

Table 5.4.4: Double-spin asymmetries $A_{||}^{\phi}$ and A_1^{ϕ} in quasi-real photoproduction of ϕ-mesons. The total uncertainty is obtained by adding statistical and systematic uncertainties in quadrature.

5.5 Comparison with Theoretical Expectations

5.5.1 Comparison with a GVMD-based Prediction

A slightly positive double-spin asymmetry A_1^ρ is observed in the cross section of exclusive production of ρ^0-mesons on the proton target, while the value of the asymmetry on the deuteron target is measured to be consistent with zero.

These results appear consistent when comparing them through Eq. (3.2.9) which relates the double-spin asymmetry A_1^ρ to the double-spin asymmetry A_1^N in inclusive DIS scattering, as proposed in [47]. The inclusive DIS asymmetries measured at HERMES [100, 101] using proton and deuteron targets are shown in fig. 5.5.1. Averaged values of these asymmetries

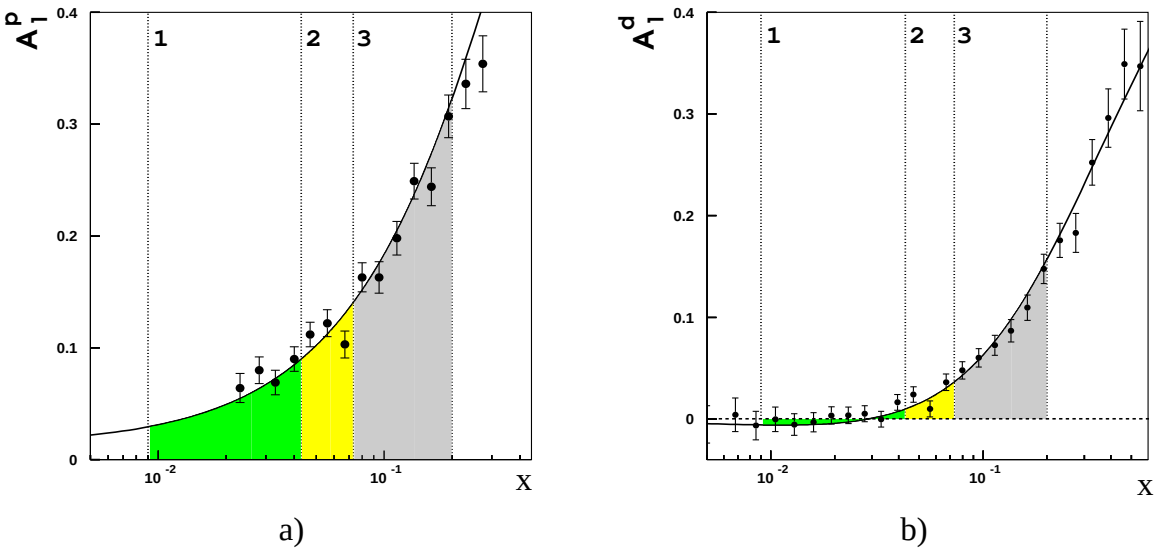

Figure 5.5.1: The x-dependence of the double-spin asymmetries measured in inclusive DIS at HERMES [100] on a) proton and b) deuteron targets. Dotted lines represent the boundaries of regions of x (marked 1, 2, 3), where the average asymmetries are calculated for this analysis. Fits from Ref. [102] were used to smooth the data. Error bars represent statistical and systematic uncertainties added in quadrature.

are calculated in the same 3 bins of x, in which also the asymmetry A_1^ρ is measured. In order to smooth the data, fits to A_1^p and A_1^d are used [102]. The average values of the asymmetries A_1^N in each x bin are given in table 5.5.1.

bin	$< x >$	$< Q^2 >$, GeV^2	A_1^p	A_1^d
1	0.032	0.9	0.0599± 0.0058	-0.0011± 0.0030
2	0.057	1.5	0.1154± 0.0067	0.0220± 0.0045
3	0.110	2.4	0.2358± 0.0063	0.0980± 0.0042

Table 5.5.1: Averaged inclusive DIS asymmetries for proton and deuteron calculated in 3 x-bins. The total error is obtained by adding statistical and systematic uncertainties in quadrature.

Using the HERMES measurement of inclusive DIS asymmetries A_1^N, values for the expected asymmetries A_1^ρ are calculated from the approximate ratio (3.2.12) as

$$A_1^\rho = \frac{2A_1^N}{1 + (A_1^N)^2} \ . \tag{5.5.1}$$

The uncertainties of the DIS asymmetries were propagated into those of the expected asymmetries A_1^ρ. In fig. 5.5.2 the measured photon absorption asymmetries A_1^ρ are compared with the expected values, calculated according to Eq. (5.5.1) in three bins of x.

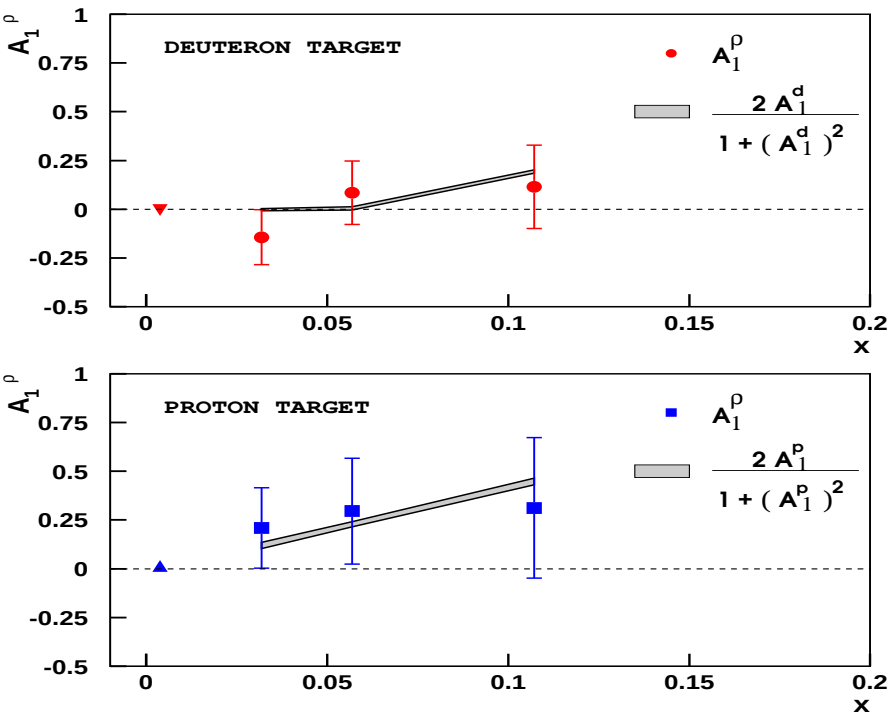

Figure 5.5.2: The x-dependence of the photon-absorption asymmetry A_1^ρ in the cross section of ρ^0-meson production for proton and deuteron targets in comparison with the theoretical expectation (5.5.1). Closed squares (circles) represent the measured asymmetry in exclusive ρ^0-meson production on the proton (deuteron) target. The gray bands indicate the values of the asymmetry A_1^ρ, expected according to Eq. 5.5.1. The triangles (shown at low x) correspond to the measured double-spin asymmetries in quasi-real photoproduction of ρ^0-mesons on proton or deuteron. The error bars indicate the total errors, obtained by adding statistical and systematic uncertainties in quadrature. In case of quasi-real photoproduction the error bars are covered by the symbol.

A qualitative agreement between the theoretical expectation and the measurement is observed for both proton and deuteron targets. This supports the relation between the two asymmetries, derived in Ref. [47], and indicates a substantial contribution of an exchange of an object with unnatural parity (e.g. a di-quark object) in ρ^0-meson production from transverse photons. No prediction for the asymmetry in quasi-real photoproduction of ρ^0-mesons was made in the framework of this approach.

5.5.2 Comparison with a Regge-based Model

The value of the double-spin asymmetry A_1^ρ, measured on the proton target, is consistent with the expectation of Ref. [51] which assumes an f_1-exchange contribution in vector-meson electroproduction. In this approach the value of the asymmetry measured with the deuteron target is expected to be the same as for the proton [54]. The coupling of the exchange object to the nucleon is related to the isospin projection T_3, therefore the coupling of the f_1-trajectory ($T=T_3=0$) to the deuteron is expected to be the same as that to the proton. A zero asymmetry on the deuteron would mean the contribution from the exchange of an object with isospin T=1, e.g. of the A_2- or A_1-meson. It was calculated that the coupling constant of the A_2-trajectory with a nucleon is very small in comparison to that of the f_2. Therefore the A_2 contribution can be neglected. The A_1-exchange can lead to an asymmetry of about 0.2 for the proton and about 0.1 for the deuteron, however, with slope and intercept that are unusual for this trajectory. Furthermore, a sufficient A_1-contribution would increase the ω-meson photoproduction cross section, which would contradict the world measurements [54].

Due to inherent simplifications in the model [51, 52, 53], no dependence of the asymmetry A_1^ρ on Q^2 or x is expected. In fig. 5.5.3 the dependence of the asymmetry $A_{||}^\rho$ on Q^2 is shown. As discussed in section 3.2.2, a slight rise of the asymmetry A_1^ρ with $-t'$ is expected [52, 54].

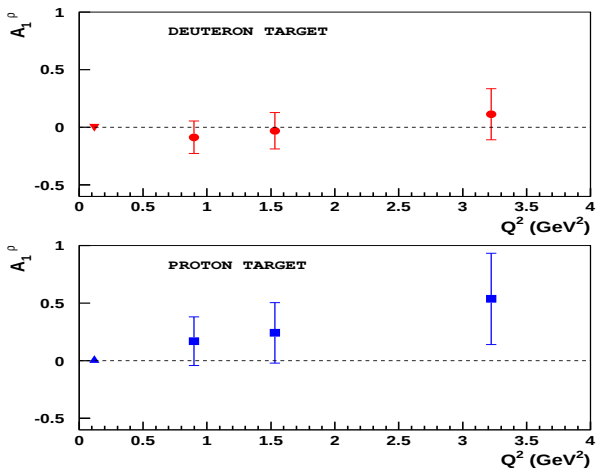

Figure 5.5.3: Q^2-dependence of the double-spin asymmetry $A_{||}^\rho$ in exclusive diffractive production (closed symbols) and quasi-real photoproduction (open symbols) of ρ^0-mesons.

In fig. 5.5.4 the prediction of the $-t'$ behavior of the asymmetry A_1^ρ is shown in comparison with the measured values. A qualitative agreement is observed.

The asymmetry $A_{||}^\rho$ for quasi-real photoproduction of ρ^0-mesons is found to be consistent with zero for both proton and deuteron targets.

There exists no theoretical prediction for the asymmetry $A_{||}^\rho$ at very low Q^2. The closest theoretical consideration is the prediction of a vanishing asymmetry $A_{||}^\rho$ for real photoproduction ($Q^2 = 0$), as discussed in section 3.2.2. It is not clear, however, if the comparison of the result measured at HERMES with the calculation for real photons is possible.

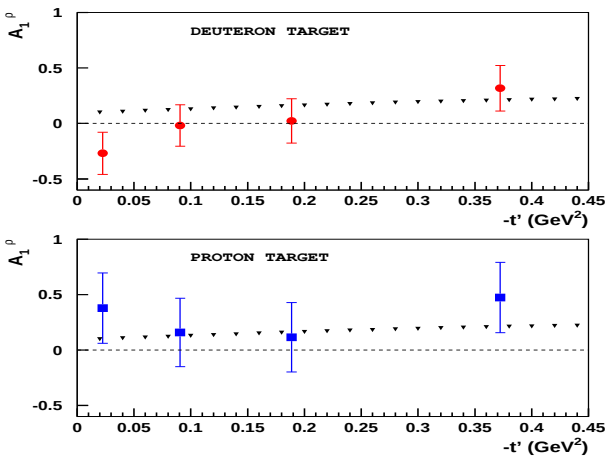

Figure 5.5.4: Double-spin asymmetry A_1^ρ in exclusive diffractive production of ρ^0-mesons in dependence on the momentum transfer $-t'$. The squares (circles) represent measurements with proton (deuteron) target, the triangles indicate the theoretical expectation of Ref. [54].

The asymmetries in the cross section of exclusive ϕ-meson production on both proton and deuteron targets are consistent with zero within statistical uncertainties. This does not disagree with the prediction [53] of small asymmetries in ϕ-meson production. No prediction for the asymmetry in ϕ-meson production was made in the framework of the model [47]. No significant dependence on Q^2 or x is observed: both the asymmetry for exclusive production and that for quasi-real photoproduction of ϕ-mesons are consistent with zero, as shown in fig. 5.5.5.

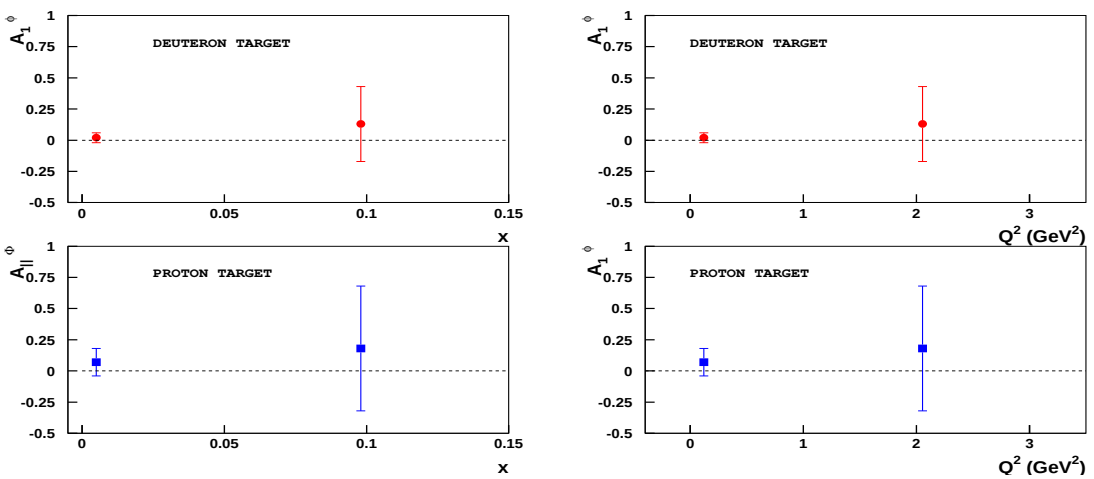

Figure 5.5.5: Double-spin asymmetry A_1^ϕ of exclusive diffractive production and quasi-real photoproduction of ϕ-mesons in dependence on Q^2 and x.

5.5.3 Prediction Based on Hadron-Parton Duality

In section 3.2.3 a relation of the double-spin asymmetry in ρ^0-meson production, A_1^ρ, to the gluon polarization $\Delta G/G$ was discussed. According to the approach of Ref. [55] the measured positive asymmetry in exclusive ρ^0-meson electroproduction A_1^ρ on the proton would result in a negative gluon contribution to the proton spin. In case of the deuteron $\Delta G/G$ would be consistent with zero.

The value of $\Delta G/G$ is predicted to be positive, although within large uncertainties, by most of the world NLO QCD fits [103]. On the other hand, theoretical predictions of negative gluon polarization still exist, as well, e.g. Ref. [104]. These predictions, however, depend strongly on the validity of the underlying models. A clear answer is expected to be given by the measurements planned at COMPASS and RHIC in the near future.

Conclusions

The double-spin asymmetries in the cross section of exclusive diffractive electroproduction and quasi-real photoproduction of ρ^0- and ϕ-mesons, respectively, were measured in scattering longitudinally polarized leptons of HERA off longitudinally polarized proton and deuteron targets at HERMES.

In the measurement of the double-spin asymmetry of *exclusive diffractive electroproduction* of ρ^0-mesons the background events corresponding to non-resonant hadron pair production were subtracted from the analyzed sample. This was realized by a fit to the invariant mass distribution of two pions, produced in the decay of the ρ^0-meson in each spin configuration of beam and target. The asymmetry of non-exclusive ρ^0-meson production was found to be consistent with zero for both targets and was taken into account as a dilution factor. The photon-absorption asymmetry A_1^ρ was calculated taking into account the contribution of the interference asymmetry A_2^ρ, as given by the longitudinal-to-transverse cross section ratio R^ρ. The photon-absorption asymmetry measured on a proton target is found to be slightly positive, confirming an earlier HERMES result, while this asymmetry measured on a deuteron target vanishes within the experimental uncertainties. Double-spin asymmetries in *exclusive diffractive electroproduction* of ϕ-mesons were measured in a similar way. The asymmetries for both proton and deuteron targets are found to be consistent with zero.

The double-spin asymmetries in *quasi-real photoproduction* of ρ^0- and ϕ-mesons were measured taking into account the non-resonant background as in the case of exclusive production. The kinematics of such events can not be fully reconstructed, as the scattered electron stays out of the spectrometer acceptance. The average values of the kinematic variables x and Q^2 for this type of process were estimated using Monte-Carlo simulations. The double-spin asymmetries for both ρ^0- and ϕ-mesons were found to be consistent with zero for both proton and deuteron targets.

Possible interpretations of the asymmetries measured in this thesis are based upon the comparison of the observed results with different theoretical models of vector-meson production mechanisms:

- The measured double-spin asymmetries A_1^ρ in exclusive ρ^0-production on proton and deuteron target are consistent with an expectation [47] that is based on the Generalized Vector Meson Dominance (GVMD) description of both exclusive ρ^0-meson production and inclusive deep inelastic scattering (DIS), with a certain relation between double-spin asymmetries in these two processes. In the approach [47] a non-zero asymmetry indicates a contribution of an unnatural-parity object exchange to ρ^0-meson production

from transverse photons. Di-quark objects have both natural and unnatural parities and therefore could be candidates for such an exchange, while the Pomeron has natural parity which would result in a zero asymmetry.

- The dependence of the asymmetry A_1^ρ on the momentum transfer to the target, $-t'$, was found to be in qualitative agreement with a recently developed prediction [51] based on the interference of the Regge trajectories f_1 and f_2 that contribute to ρ^0 production. In this approach, however, similar asymmetries for proton and deuteron targets are expected. The measured double-spin asymmetries in exclusive ϕ-production agree with the theoretical expectation [51] that is based on the interference of f_1 and Pomeron exchanges which dominate ϕ-meson production. Marginal statistics, however, do not allow to arrive at more specific conclusions.

- The quark-exchange mechanism is predicted by a pQCD calculation [28, 29] to dominate ρ^0-meson production in the HERMES energy range. The double-spin asymmetry, however, can not be estimated in this model, as the necessary underlying factorization theorem does not exist for transverse photons, yet.

There exists no theoretical calculation on double-spin asymmetries in quasi-real photoproduction of vector mesons ($Q^2 \approx 0$). Since the double-spin asymmetries in quasi-real photoproduction of ϕ- and ρ^0-mesons were measured to be consistent with zero, they do not contribute to the measurement of the double-spin asymmetry in high-p_t hadron production. However they have to be taken into account as dilution. This is important information for future HERMES analyses to access the polarized gluon contribution to the nucleon spin. No theoretical predictions for double-spin asymmetries in quasi-real photoproduction of vector mesons exist up to now.

The double-spin asymmetries in exclusive diffractive ρ^0-meson measured at HERMES for proton and deuteron are compared to those investigated at the SMC experiment [81] in a different kinematic region, $140 < W^2 < 310$ GeV^2. In this region Pomeron exchange is thought to dominate [11] vector-meson production. In [81] the asymmetries were found to be consistent with zero for both proton and deuteron targets in the region $0.01 < Q^2 < 5$ GeV^2, and slightly negative at $Q^2 \sim$10 GeV^2 which confirms the dominance of Pomeron exchange at high energies. The double-spin asymmetries measured in this thesis indicate a significant Reggeon- or di-quark object-exchange to vector meson production in a different kinematic region and therefore does not contradict the SMC result.

In summary, the observed relation of the double-spin asymmetry in exclusive ρ^0-production with that in inclusive DIS and the consistence of the measured asymmetry with the GVMD prediction [47] indicate a significant contribution of an exchange of a di-quark object with unnatural parity to ρ^0-meson production at HERMES energies. Unnatural-parity object exchange is supported by a calculation in the framework of a recently developed model [51, 52, 53] and an expectation [28] obtained in the framework of pQCD for longitudinal photons. The direct measurements of ρ^0 spin density matrix elements [33] show that the unnatural-parity amplitude does not contribute significantly into the cross section of exclusive ρ^0-meson production. The double-spin asymmetries, however, are sensitive to unnatural-parity amplitudes through their interference with natural-parity amplitudes. The conclusion

can be drawn that at the intermediate energies of the HERMES experiment ρ^0-meson production follows the GVMD scheme with subsequent scattering of the vector-meson state off the nucleon proceeding via exchange of both Reggeon(s) and Pomeron(s) in the t-channel.

More information about unnatural-parity contributions can be obtained in future measurements of spin density matrix elements in lepton scattering off a *transversely* polarized proton target, as they are planned at HERMES in the near future.

Appendices

1. Additional Tables

The numbers of vector-meson candidates, obtained from the analyzed samples after applying the selection cuts discussed in section 5.1 without further background subtraction, are listed in table A.1.1, separated according to the used μDST productions. The values of beam and target polarization are given as well as the number of DIS electrons and the integrated luminosity $\mathcal{L}$. The integrated luminosity was estimated from the number of DIS electrons

μDST production		96c1	97c1	98c1	99b2	00b1
Exclusive diffractive	N^{ρ}	542	1569	836	924	4880
production	N^{ϕ}	75	217	76	92	442
Quasi-real	N^{ρ}	111937	323832	587995	645107	2217849
photoproduction	N^{ϕ}	3077	7610	9135	10422	48756
Number of DIS electrons	$N_{DIS} \times 10^6$	0.614	1.743	1.114	1.218	6.361
Luminosity	$\mathcal{L}$ (pb^{-1})	12.2	34.8	25.2	27.5	144.0
Target polarization	P_T	0.794	0.865	0.812	0.805	0.857
Beam polarization	P_B	0.529	0.529	0.510	0.532	0.536

Table A.1.1: Statistics used in the analysis, separated by the μDST production.

in every data sample using the known DIS cross section on nuclear targets. For HERMES it is known that one million DIS electrons corresponds to the integrated luminosity of 21.8 pb^{-1}. The DIS electrons were selected applying the following limitations, additional to the track selection criteria discussed in section 5.1:

- charge of the scattered lepton equal to charge of the beam lepton,
- energy deposited in the calorimeter is above 3.5 GeV,
- kinematic cuts : $Q^2 > 1$ GeV^2, $W^2 > 4$ GeV^2, $0 < y < 0.85$.

The average kinematic values for exclusive diffractive ρ^0- and ϕ-meson production at HERMES are listed in table A.1.2. Table A.1.3 contains the values of the effective polarization D^ρ and the contribution of the asymmetry A_2^ρ, given by the longitudinal-to-transverse cross section ratio R^ρ in every studied kinematic bin, separately for proton and deuteron target.

Variable	$< D >$	$< \eta\sqrt{R} >$	x	$< Q^2 >$ GeV^2	$< W^2 >$ GeV^2	$< -t' >$
ρ^0	0.357	0.062	0.070	1.77	24.4	0.121
ϕ	0.359	0.064	0.078	1.75	22.5	0.179

Table A.1.2: Average kinematic variables for ρ^0- and ϕ-meson production at HERMES

bin boundaries	D^ρ		$\eta\sqrt{R^\rho}$	
	^{1}H	^{2}H	^{1}H	^{2}H
$x < 0.043$	0.47	0.47	0.030	0.030
$0.043 < x < 0.073$	0.34	0.34	0.056	0.056
$0.073 < x$	0.28	0.28	0.102	0.099
$Q^2 < 1.15$	0.42	0.41	0.037	0.038
$1.15 < Q^2 < 2.05$	0.33	0.34	0.064	0.062
$2.05 < Q^2$	0.30	0.30	0.100	0.099
$W^2 < 21.5$	0.25	0.25	0.094	0.092
$21.5 < W^2 < 26.0$	0.33	0.32	0.064	0.066
$26.0 < W^2$	0.48	0.47	0.037	0.039
$-t' < 0.04$	0.36	0.35	0.062	0.063
$0.04 < -t' < 0.10$	0.35	0.36	0.066	0.063
$0.10 < -t' < 0.19$	0.36	0.35	0.062	0.066
$0.19 < -t'$	0.36	0.35	0.067	0.067

Table A.1.3: Average effective polarization factor D and contribution from the asymmetry A_2 of ρ^0-meson production on proton and deuteron in every kinematic bin.

2. Comparison with the Previous HERMES-Publication

The first measurement of the double-spin asymmetry in exclusive diffractive ρ^0-meson production on a proton target at HERMES was presented in Refs. [82, 46]. The data, collected on a polarized proton target in the period 1996-1997, were re-analyzed using the improved data production set and the most recent parameterization of the cross-section ratio R^ρ. The μDST production 97b2, used for the analysis of Ref. [82], and the recent μDST production 97c1 were compared in detail. It was found that the information about short tracks was missing in the production 97b2. This affects the selection criteria for exclusive production, based on the requirement of only 3 tracks in the event. An event with e.g. 3 full tracks and an additional short one would be treated as an exclusive event candidate in the 97b2

production, since the information about this short track is missing. However, for the cross-check of the presented data and those analyzed in [82], the production 97b2 was used. Using the selection criteria of the analysis [82], excellent agreement in the number of selected ρ^0-candidates was obtained. The comparison of the double-spin asymmetry $A_{||}^{\rho}$ on the proton target, measured in [82], and the asymmetry obtained in the present analysis using the data from the 1996-1997 data taking period is shown in fig. A.2.1

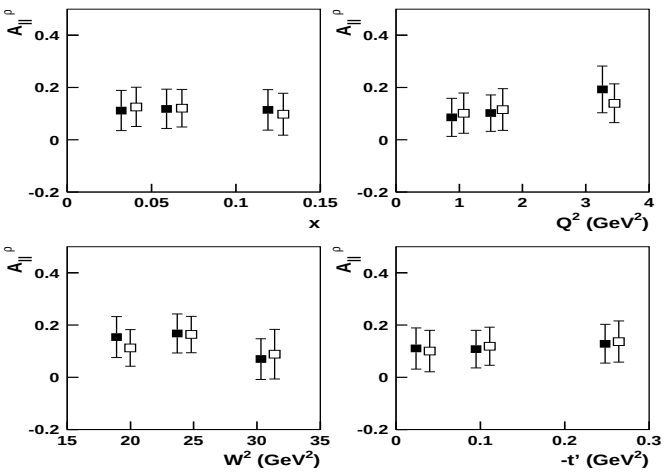

Figure A.2.1: The double-spin asymmetry A_1^{ρ} of exclusive diffractive production of ρ^0-mesons on the proton target in dependence on kinematical variables. The data of analysis [82] (closed symbols) and the present analysis (open symbols) are compared.

3. Acceptance Corrections

In the general case of a cross section determination the results of the measurements with the HERMES spectrometer have to be corrected for its limited acceptance which affects the original distribution of a certain kinematic variable in the 4π-geometry.

In the case of double-spin asymmetries the spin dependence of the acceptance itself is important. The double-spin asymmetry in 4π-geometry reads:

$$A_{||} = \frac{a^{\vec{\Leftarrow}} N^{\vec{\Leftarrow}} L^{\vec{\Rightarrow}} - a^{\vec{\Rightarrow}} N^{\vec{\Rightarrow}} L^{\vec{\Leftarrow}}}{a^{\vec{\Leftarrow}} N^{\vec{\Leftarrow}} L_p^{\vec{\Rightarrow}} + a^{\vec{\Leftarrow}} N^{\vec{\Rightarrow}} L_p^{\vec{\Leftarrow}}} \tag{A.3.1}$$

where $N^{\vec{\Leftarrow}}$ ($N^{\vec{\Rightarrow}}$) and $a^{\vec{\Leftarrow}}$ ($a^{\vec{\Rightarrow}}$) denote the number of produced vector mesons and the acceptance correction factor in a certain kinematic bin with the target spin oriented antiparallel (parallel) to the beam spin, respectively. Once the acceptance correction function appears to be spin independent, it cancels out in Eq. A.3.1. The spin dependence of acceptance corrections at HERMES has not been studied, yet. There exists no Monte-Carlo simulation yet, where any of the spin-dependent mechanisms of the asymmetry in vector-meson production, discussed in section 5.5, has been implemented.

The effect of a possible spin dependence of the HERMES acceptance could be seen from a comparison of vector-meson angular distributions in both spin configurations of beam and

target. In fig. A.3.1 the angular distributions of exclusive ρ^0-meson production are shown for both spin configurations of beam and target. No difference can be seen from comparing both distributions in any of the presented variables within the given statistical accuracy.

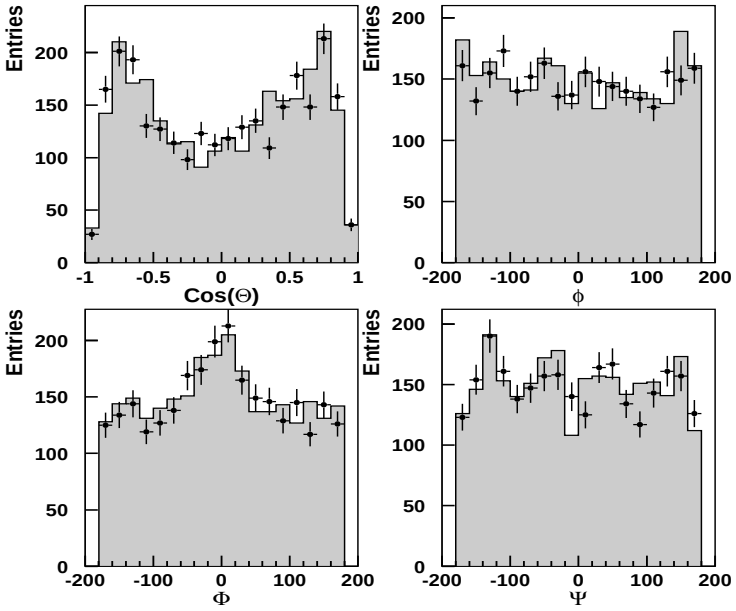

Figure A.3.1: Angular distributions for exclusive ρ^0-meson production when the target spin is oriented parallel (shaded histogram) or antiparallel (closed symbols) to the spin of the beam.

4. Radiative Corrections

In Ref. [105] radiative corrections to the Born cross section of ρ^0 production (cf. fig. 1.1.1 b)) were estimated to vary between 10% and 20% for HERMES energies, weakly depending on Q^2 for $Q^2 > 1$ GeV^2 and vanishing at lower Q^2. The spin dependence of radiative corrections in exclusive vector-meson production is discussed in Ref. [106], where the SCHC-violation in the ρ^0 spin density matrix element, r^5_{00}, is related to radiative corrections originating from non-observed QED effects. For the majority of the SDMEs, forbidden by SCHC, radiative corrections turned out to be about 1%. The radiative corrections were applied in Ref. [33] in the measurement of the SDME for the ρ^0-meson and appeared to be negligible. Therefore it can be concluded that radiative effects do not affect the measurement of double-spin asymmetries in exclusive diffractive ρ^0-production.

References

[1] Particle Data Group, Review of Particle Physics, Eur. Phys. J. 3 (1998) 188

[2] J. David Jackson, 'Klassische Elektrodynamik', W. de Gruyter, New York; Berlin (1983)

[3] D. H. Perkins, 'Introduction to high energy physics', MIR, Moscow, (1975)

[4] G. Shaw, 'Introduction to diffractive processes', hep-ph/0011007, (2000)

[5] H. Abramowicz, 'Diffraction and the Pomeron', hep-ph/00011054, (2000)

[6] T. H. Bauer et. al, 'Hadronic properties of the photon', Rev. Mod. Phys., Vol. 50, No 2, (1978)

[7] Chr. Friberg, 'Aspects of QCD and photon structure', Ph. D. Thesis (2000)

[8] T. Sjostrand, 'PYTHIA 5.7 and Jetset 7.4', Physics and manual, (1993)

[9] Chr. Friberg, 'Total Cross Section with Virtual Photons',hep-ph/0005048, (2000)

[10] A. Borissov, 'Diffractive physics at HERMES', conference proceedings, International Workshop on Deep Inelastic Scattering and QCD (DIS 99) (1999)

[11] D. Schildknecht, G.A. Schuler, B. Surrow, 'Vector-Meson Electroproduction from Generalized Vector Dominance', Phys.Lett. B449 (1999) 328-338

[12] D. Schildknecht, G. Cvetic, A. Soshi, 'Off-diagonal generalized vector dominance in DIS and QCD', 1999 Acta Phys.Polon. B30 (1999) 3265-3284

[13] J.J. Sakurai, D. Schildknecht, 'Generalized vector dominance and inelastic electron-proton scattering', Phys. Lett. B 40 (1972), 121-126

[14] D. Schildknecht, G. Cvetic, A.Soshi, 'Deep inelastic scattering, QCD and off-diagonal generalized vector dominance', Eur.Phys.J. C13 (2000) 301-314

[15] H. Fraas et. al, 'On the differential cross section and the slope of vector meson electroproduction', Nuclear Physics B88 (1975) 301-317

[16] G.F. Chew, S. C. Frautschi, 'Principle of equivalence for all strongly interacting particles within S-matrix framework', Phys. Rev. Lett. 7 (1961) 394-397

[17] G.F. Chew, S. C. Frautschi, S. Mandelstam, 'Regge poles in $\pi\pi$ scattering', Phys. Rev. 126 (1962) 1202-1208

[18] A. Donnachie, P. V. Landshoff, 'Total cross sections', Phys. Lett. B296 (1992) 227-232

[19] A. Donnachie, P. V. Landshoff, 'Exclusive vector photoproduction: confirmation of Regge theory', Phys.Lett. B478 (2000) 146-150

[20] X. Ji, 'Off-Forward Parton Distributions', J.Phys. G24 (1998) 1181-1205

[21] X. Ji, W. Melnitchouk X. Song, 'A Study of Off-Forward Parton Distributions', Phys.Rev. D56 (1997) 5511-5523

[22] X. Ji, 'Deeply Virtual Compton Scattering', Phys.Rev. D55 (1997) 7114-7125

[23] J. C. Collins, L. Frankfurt, M. Strikman, 'Factorization for hard exclusive electroproduction of mesons in QCD', Phys. Rev. D56 (1997) 2982-3006

[24] M. Diehl, T. Gousset, B. Pire, 'Exclusive electroproduction and off-diagonal parton distributions' hep-ph/9811220, (1998)

[25] A. Donnachie, P. V. Landshoff, 'Exclusive vector-meson production at HERA', hep-ph/9411368 (1994)

[26] L. P. A. Haakman, A. Kaidalov, J.H. Koch, 'Production of vector mesons by real and virtual photons at high energies', Phys. Lett. B 365 (1996) 411

[27] A. Airapetian et. al, HERMES Collaboration, 'Exclusive leptoproduction of ρ^0 mesons from hydrogen at intermediate virtual photon energies', Eur. Phys. J. C 17 (2000) 389-398

[28] M. Vanderhaeghen, P. A. M. Guichon, M. Guidal, 'Hard electroproduction of photons and mesons on the nucleon', Phys. Rev. Lett. 80 (1998) 5064

[29] M. Vanderhaeghen, P. A. M. Guichon, M. Guidal, 'Deeply virtual electroproduction of photons and mesons on the nucleon', Nucl.Phys. A663-664 (2000) 324-327.

[30] K. Schilling, P. Seyboth, G. Wolf, 'On the analysis of vector-meson production by polarized photons', Nucl.Phys. B61(1970) 397-412.

[31] K. Schilling, G. Wolf, 'How to analyze vector-meson production in inelastic lepton scattering', Nucl.Phys. B61(1973) 381-413.

[32] H. Fraas, 'Vector meson production by inelastic scattering of polarized electrons off polarized nucleons', Ann. Phys. 87 (1974) 417

[33] M.Tytgat, Ph. D. thesis (2001), Universiteit Gent, Belgium

[34] G. L. Rakness, Ph. D. thesis (2000), University of Colorado, USA

[35] C. Adloff et. al, H1 Collaboration, DESY-99-010 (1999)

[36] I. Royen, 'Helicity in diffractive vector-meson production', hep-ph/0006044 (2000)

[37] E.V. Kuraev, N. N. Nikolaev, B.G. Zakharov, 'Diffractive vector mesons beyond the s-channel helicity conservation', hep-ph/9809539 (1998)

[38] A. V. Manohar, 'An introduction to spin dependent inelastic scattering', Proceedings of the 7th Lake Louise Winter Institute, World Scientific, 1992

[39] G. Altarelli, G. Parisi, 'Asymptotic freedom in parton language', Nucl. Phys. B126, 298 (1977)

[40] V. N. Gribov, L.N. Lipatov, 'Deep inelastic *ep* scattering in perturbation theory', Sov. J. Nucl. Phys. 15 (1972), 438

[41] D. Adams et al. SMC Collaboration, 'The spin-dependent structure function $g_1(x)$ of the proton from polarised deep-inelastic muon scattering', Phys. Lett. B412 (1997) 414,
D. Adams et al. SMC Collaboration, 'A new measurement of the spin-dependent structure function $g_1(x)$ of the deuteron', Phys. Lett. B357 (1995),
K. Abe et al. E143 Collaboration, 'Measurements of the proton and deuteron spin structure function g_1 and asymmetry A_2', Phys. Rev. Lett. 76 (1996) 587

[42] K. Ackerstaff et al., HERMES Collaboration, 'Measurement of the Neutron Spin Structure Function g_1^n with a Polarised 3He Internal Target', Phys. Lett. B404 (1997) 383-389,
K. Ackerstaff et al., HERMES Collaboration, 'Measurement of the Proton Spin Structure Function g_1^p with a Pure Hydrogen Target', Phys. Lett. B442 (1998) 484-492,
C. Weiskopf 'A HERMES Measurement of the Deuteron Spin Structure Function g_1^d' 9th International Workshop on Deep Inelastic Scattering and QCD (DIS 2001), (2001)

[43] R. L. Jaffe, A. Manohar, 'The g_1 problem: deep inelastic electron scattering and the spin of the proton', Nucl. Phys. B337, 509 (1990)

[44] R. L. Jaffe, 'The spin structure of the Nucleon: Theoretical Overview', hep-ph/0102281, (2001)

[45] K. Ackerstaff et al., HERMES Collaboration, 'Measurement of Angular Distributions and $R = \sigma_L/\sigma_T$ in Diffractive Electroproduction of rho0 Mesons', Eur. Phys. Jour. C 18 (2000) 303-316.

[46] A. Airapetian et al., HERMES Collaboration, Phys. Lett. B 513 (2001) 301-310

[47] H. Fraas, 'Cross-section asymmetries in vector-meson electroproduction and in inelastic *ep* scattering with polarized beam and target', Nuclear Physics B113 (1976) 532-546

[48] V. Eckard et al., DESY 74/5 (1974)

[49] J. Ballam et al., 'Production of vector mesons by muons in a hybrid bubble-chamber experiment', Phys. Rev. D10 (1974) 765

[50] A. Airapetian et al., HERMES Collaboration, 'Measurement of the proton spin structure function $g_1(p)$ with a pure hydrogen target', Phys. Lett. B 442 (1998) 484

[51] N. I. Kochelev, D.-P. Min, V. Vento, A. V. Vinnikov, 'A mechanism for the Double-Spin Asymmetry in Electromagnetic ρ Production at HERMES', hep-ph/0112292 (2001)

[52] N. I. Kochelev, D.-P. Min, Y. Oh, V. Vento, A. V. Vinnikov, 'A new anomalous trajectory in Regge theory', hep-ph/9911480 (1999)

[53] N. I. Kochelev, D.-P. Min, Y. Oh, V. Vento, A. V. Vinnikov, 'Anomalous f_1 exchange in vector meson photoproduction asymmetries', hep-ph/0001209 (2000)

[54] N. Kochelev, A. Vinnikov, private communications

[55] M. G. Ryskin, 'Diffractive ρ meson leptoproduction on polarized nucleon', hep-ph/9706505 (1997)

[56] A. D. Martin, M. G. Ryskin, T. Teubner, 'The QCD description of diffractive ρ meson electroproduction', hep-ph/9609448 (1996)

[57] A. D. Martin, M. G. Ryskin, T. Teubner, 'Q^2 dependence of diffractive vector meson electroproduction', Phys.Rev. D62 (2000) 014022

[58] W. Vogelsang, 'Polarized lepton nucleon scattering', JHEP 9903 (1999), hep-ph/9906289

[59] A. Bravar, D. von Harrach, A. Kotzinian, 'Gluon Polarization from Correlated High p_T Hadron Pairs in Polarized Electroproduction', Phys. Lett. B 421 (1998)

[60] P. Liebing, Diplomarbeit, Humboldt Universität zu Berlin (2001)

[61] V. A. Korotkov, W.-D. Nowak, 'Future Measurements of Deeply Virtual Compton Scattering at HERMES', hep-ph/0108077 (2001)

[62] A. A. Sokolov, I. M. Ternov, 'On polarization and spin effects in the theory of synchrotron radiation', Sov. Phys. Doklady 8 (1964) 1203

[63] J. Buon, K. Steffen, 'HERA variable-energy m̈inišpin rotator and head-on ep collision scheme with choice of electron helicity', Nucl. Instr. and Methods, A245 (1986) 248

[64] D.P. Barber et al., 'The HERA Polarimeter and the First Observation of Electron Spin Polarization at HERA'Nucl., Instr. and Meth. A329 (1993) 79

[65] M. Beckmann et. al., 'The longitudinal Polarimeter at HERA' (2000), physics/0009047

[66] K. Ackerstaff et al., 'Beam-Induced Nuclear Depolarisation in a Gaseous Polarised Hydrogen Target', Phys. Rev. Lett. 82 (1999) 1164-1168.

[67] Chr. Baumgarten, 'Studies of spin relaxation and recombination at the HERMES Hydrogen/Deuterium gas target', Dissertation, Ludwig-Maximilians-Universität München (2000)

[68] Chr. Baumgarten, 'The HERMES Internal Polarized Hydrogen and Deuterium Targets', 13th International Symposium on High Energy Spin Physics (SPIN 98) (1998)

[69] H. Kolster, 'The HERMES gaseous internal polarized target and its use in the HERA positron storage ring', Dissertation, Ludwig-Maximilians-Universität München (1998)

[70] K. Ackerstaff et al., HERMES Collaboration 'The HERMES Spectrometer'(1998), Nucl. Instr. and Meth., A417 (1998) 230-265

[71] A. Schwind et al., 'The HERMES Back Drift Chambers', Nucl. Instr. and Meth., A416 (1998) 45-58

[72] W. Wander, 'Reconstruction of High Energy Scattering Events in the HERMES Experiment', Ph.D. Thesis Universität Erlangen-Nuernberg (1996)

[73] Y. Gärber, 'Messung der Proton-Spinstrukturfunktion g_1 bis zu kleinstmöglichen Bjorken-x mit dem HERMES-Experiment', Dissertation, Humboldt-Universität zu Berlin (2001)

[74] E. C. Aschenauer at al., The HERMES RICH group, 'The HERMES Dual-Radiator Ring-Imaging Cherenkov Detector', DESY report 00-190, submitted to NIM A (2000)

[75] K. Negodaeva, 'Inclusion of the Aerogel Boundary Refraction into the HERMES RICH Reconstruction', HERMES Internal Note 99-022 (1999)

[76] E. Cisbani, R. Kaiser, D. De Schepper 'Particle Identification with the HERMES RICH Detector: Description of the Different Approaches', HERMES Internal Note 98-008 (1998)

[77] A. Maas, 'Particle Identification with RICH detectors: Algorithms and their optimization', Diplomarbeit, Universität Darmstadt (2000)

[78] K. Negodaeva, 'The PID efficiency of the HERMES RICH detector for the IRT method', HERMES Internal Note 00-028 (2000)

[79] R. Kaiser,'Unfolding of Hadrons Distributions and Asymmetries ', HERMES Internal Note 00-027 (2000)

[80] K. Negodaeva, report on the RICH subgroup meeting (1999)

[81] A. Tripet, 'Exclusive ρ^0 Production in Polarized DIS at SMC', Nucl. Phys. B (Proc. Suppl.) 79 (1999) 529-531

[82] F. Meissner,'Measurement of the J/ψ Cross section and Double-Spin Asymmetries in Vector-Meson Production in Polarized Lepton-Nucleon Scattering at HERMES' Dissertation, Humboldt-Universität zu Berlin (2000)

[83] HERMES Collaboration, 'A Large Acceptance Recoil Detector for HERMES ', HERMES Proposal 01-017 (2001)

[84] M. Kolstein, 'Exclusive ρ^0-meson electroproduction at HERMES', Ph. D. Thesis (1998), Vrije Universiteit Amsterdam, Holland

[85] E. Belz, 'Measurement of Decay Angle Distributions in Diffractive Electroproduction of ρ^0 Mesons and an Extraction of R(Q2)', HERMES Internal Note 98-028, (1998) ;
E. Belz, 'Rho Polarization in Exclusive A (e, e', ρ^0)', HERMES Internal Note 96-052, (1996)

[86] T. O'Neill 'Notes on the Letter: Observation of a Coherence Length Effect in Exclusive ρ^0 Electroproduction', (2000) HERMES Internal Note 00-018

[87] H. Holtman, N. N. Nikolaev, A. Szczurek, J. Speth, B. G. Zakharov, 'On the determination of double diffraction dissociation cross section at HERA', Z. Phys. C 69 (1996), 297

[88] M. R. Adams et al., 'Diffractive production of $\rho^0(770)$ mesons in muon-proton interaction at 470 GeV', E665 Collaboration, Z. Phys., C74 (1997), 237

[89] T. Sjostrand et al., 'High-Energy-Physics Event Generation with PYTHIA 6.1', LU TP 00-30, hep-ph/0010017

[90] T. Sjostrand, 'PYTHIA 6.2', Physics and manual, 2000, LU TP 01-21, hep-ph/0108264

[91] P. Liebing, private communications

[92] CERN-CN Division, 'GEANT - Detector Description and Simulation Tool', CERN Program Library Long Writeup W5013, CERN, (1993)

[93] W. D. Schambroom et al., 'Diffractive production of vector mesons in muon-proton scattering at 150 and 100 GeV', Phys. Rev. D 26 (1982) 1

[94] M. Ross, L. Stodolsky, 'Photon Dissociation Model for Vector-Meson Photoproduction', Phys. Rew. 149 (1996) 149

[95] P. Söding, 'On the apparent shift of the rho meson mass in photoproduction', Phys. Lett. 19 (1996) 702

[96] S. D. Drell, 'Production of particle beams at very high energies', Phys. Rev. Lett. 5 (1960) 278

[97] S. D. Drell, 'Peripheral Contributions to High-Energy Interaction Processes', Rev. Mod. Phys. 33 (1961) 458

[98] M. Tytgat, 'Studies of the ρ^0 and ω Invariant Mass Distribution', HERMES Internal Note 00-019 (2000)

[99] A. I. Titov, Y. Oh, S. N. Yang, 'Polarization Observables in ϕ Meson Photoproduction and the Strangeness Content of the Proton', nucl-th/9702015 (1997)

[100] U. Stösslein, 'Measurement of the Spin Structure Functions g_1 of the Proton and the Deuteron', 14th International Spin Physics Symposium (SPIN 2000), 2000, Conference Proceedings 00-53

[101] Christoph Weiskopf, Ph. D. Thesis in preparation

[102] U. Stösslein, I. Akushevich, private communications

[103] J. Blümlein, H. Böttcher, 'QCD Analysis of Polarized Deep Inelastic Scattering Data', hep-ph/0107317 (2001);
K. Abe et. al, the E154 Collaboration, 'Next-to-leading order QCD analysis of polarized deep inelastic scattering data', Phys. Lett. B405 (1997) 180;
B. Adeva et. al, the SMC Collaboration, 'Next-to-leading order QCD analysis of the spin structure function g_1', Phys. Rev. D58 (1998) 112002;
Y. Goto et al., 'Polarized parton distribution functions in the nucleon', Phys. Rev. D62(2000) 34017;
M. Glück et al., 'Models for the polarised parton distributions of the nucleon', Phys. Rev. D63(2001) 94005;
E. Leader et. al, 'A new evaluation of polarized parton densities in the nucleon', hep-ph/0111267

[104] N. I. Kochelev, 'Instanton Contribution to Polarized and Unpolarized Gluon Distribution in Nucleon', hep-ph/9707418 (1997)

[105] I. Akushevich, 'Radiative Correction to Cross Section of Exclusive ρ Electroproduction', HERMES Internal Note 97-059 (1997)

[106] I. Akushevich, P. Kuzhir 'QED radiative correction to spin-density matrix elements in exclusive vector meson production', Phys. Lett. B474(2000)411

Acknowledgments

I would like to thank all those who have supported me, directly and indirectly, on the way towards the completion of my thesis. First of all, I am grateful to my supervisor, Wolf-Dieter Nowak, for encouraging me doing vector-meson physics at HERMES, for discussions, support and lots of wise advises concerning sometimes not only pure scientific subjects. I would like to thank my advisor and friend Elke Aschenauer, who helped me a lot in understanding HERMES physics, data production and analysis. Even overloaded with other tasks, she always found time to answer any crazy question about HERMES, universe and everything. My special thanks goes to Wolf-Dieter and Elke for careful reading of and advises for the thesis. I use this opportunity to express my cordial thanks to Adolf Schwind, from whom I learned a lot about the operation of the drift chambers and the gas system. This gave me the chance to not only enjoy the data collected by the experiment, but also to contribute to a stable detector operation. I enjoyed it working within the RICH group, from which I would like to thank Peter Jung, Elke Aschenauer, Axel Maas and Brecht Hommez for cooperation in solving problems of reconstruction and efficiencies. It would like to thank Falk Meissner for the introduction to the vector-meson asymmetry analysis. It was nice working together with the vector-meson analysis crew, where a lot of very specific questions were thoroughly discussed, thanks to the experience of Alexander Borissov and Michael Tytgat. My gratitude goes to Oleg Teryaev, Nikolai Kochelev and Andrey Vinnikov, for extensive discussions and providing me with results of their theoretical calculations.

My special thanks are addressed to my LPI colleagues Alexei Kozlov and Serguei Potashov, who brought me in contact with the HERMES-Zeuthen group which made my Ph.D. studies within the HERMES Collaboration possible, at all. In addition I would like to mention S. Rusakov, A. Fomenko, A. Lebedev, V. Andreev and other members of the laboratory of electromagnetic interactions in LPI. I thank all the members of the HERMES-Zeuthen group, especially Wolf-Dieter, Elke, Uta, Adolf, Helmut, Patricia, Markus, Avto, Falk, Delia, Yvo and Frank for the wonderful friendly atmosphere and a possibility to have fun doing physics in such a nice team. I would like to thank the members of the HERMES Collaboration, mentioning especially Manuella Vincter, James Ely, Shigenobu Yoneyama, Vitaly Shutov, Maurice Bouwhuis, Christoph Weiskopf and many others whom I may have forgotten, and I therefore apologize in advance.

Finally I want to thank those people who will hardly ever read my thesis, but who supported me and cheered me up when something went wrong. My small family - my parents and husband - I thank you for your love and understanding.

Erklärung

Hiermit erkläre ich, die Dissertation selbständig und ohne unerlaubte Hilfe angefertigt zu haben. Ich habe mich anderwärts nicht um einen Doktorgrad beworben und besitze einen entsprechenden Doktorgrad nicht. Ich erkläre die Kenntnisnahme der dem Verfahren zugrunde liegenden Promotionsordnung der Mathematisch-Naturwissenschaftlichen Fakultät I der Humboldt-Univertität zu Berlin.

K. Lipka den März, 11, 2002.

Lebenslauf

Persönliche Daten:

Name:	Lipka (E)Katerina Mikhailovna
Geburtsname:	Negodaeva
Geburtsdatum:	22 Mai 1977
Geburtsort:	Lubertsy, Moskauer Gebiet, Russland
Staatsangehörigkeit:	Russland

Schulausbildung:	1984–1994	Gymnasium 44, Lubertsy, Moskauer Gebiet, Russland
Berufsausbildung:	1994–1999	Studium der *Experimentellen Methoden der Teilchenphysik* Fakultät der Experimentellen und Theoretischen Physik, Moskauer Physikalisches-Ingenieur Institut (MIPhI) Moskau, Russland Abschluss mit Auszeichnung: Diplom-Kernphysikerin
Beruflicher Werdegang	05/99–05/02	Wissenschaftliche Hilfskraft am Forschungszentrum DESY Zeuthen
	ab 05/98	Wissenschaftliche Mitarbeiterin am Labor der Elektromagnetischen Wechselwirkung des Lebedev Physikalischen Institutes (LPI), Moskau, Russland
	07/98-09/98	Sommerpraktikum am Forschungsinstitut CERN (Schweiz)
	08/98-09/97	Sommerpraktikum am Forschungsinstitut DESY Hamburg
	09/96–01/97	Ingenieur am Lehrstuhl der Biophysik des Moskauer Physikalischen-Ingenieur Institutes